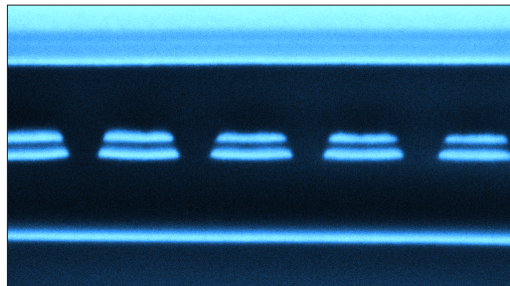


MICROCAVITY PLASMONICS



Von der Fakultät für Mathematik und Physik der Universität Stuttgart
zur Erlangung der Würde eines Doktors der Naturwissenschaften (Dr. rer. nat.)
genehmigte Abhandlung

vorgelegt von

Ralf Ameling

aus Aalen

Hauptberichter:	Prof. Dr. Harald Giessen
Mitberichter:	Prof. Dr. Peter Michler
Tag der Einreichung:	07.06.2011
Tag der mündlichen Prüfung:	29.07.2011

4. Physikalisches Institut der Universität Stuttgart
2011

ZUSAMMENFASSUNG

Das Verständnis der Wechselwirkungen von Licht und Materie im Nanometerbereich bildet die Grundlage für viele zukünftige Technologien, Anwendungen und Materialien. Im Rahmen dieser Arbeit wurden gekoppelte plasmonisch-photonische Systeme untersucht, die aus einer Kombination von photonischen Mikroresonatoren und metallischen Nanostrukturen bestehen. In solchen Systemen ist es möglich, eine besonders starke Kopplung zwischen den elektromagnetischen Lichtmoden eines Resonators und kollektiven Elektronenschwingungen (Plasmonen) im Metall zu beobachten. Über das Nahfeld gekoppelte Nanodrahtpaare wurden dazu zwischen zwei Metallschichten, die einen Mikroresonator bilden, platziert. Abhängig von der Position der Nanodrähte im Mikroresonator können dabei sowohl elektrische als auch magnetische Moden des Lichts an symmetrische und antisymmetrische Plasmonenmoden koppeln, die jeweils elektrische und magnetische Dipole aufweisen. Die gemessenen Kopplungsstärken sind dabei sowohl im elektrischen als auch im magnetischen Fall außergewöhnlich hoch. Platziert man die Nanostrukturen nahe an die Spiegel des Resonators, können neben den lokalisierten Teilchenplasmonen auch propagierende Oberflächenplasmonen an den Grenzschichten des Metalls angeregt und stark an die photonischen Lichtmoden gekoppelt werden. Darüber hinaus wurde eine erste Anwendungsmöglichkeit der Strukturen als Sensoren untersucht. Die Ergebnisse haben gezeigt, dass gekoppelte photonisch-plasmonische Strukturen durch umgebungsabhängige Phasenverschiebungen bei der Plasmonenanregung eine weitaus höhere Sensitivität gegenüber Änderungen in ihrer Umgebung als herkömmliche lokalisierte plasmonische Sensoren aufweisen. Die Arbeit umfasst theoretische Modelle und Simulationen von nah- und fernfeldgekoppelten plasmonischen Systemen um die beobachteten Phänomene zu erklären. Außerdem werden die experimentellen Verfahren zur Herstellung und Vermessung der mehrschichtigen Nanostrukturen vorgestellt. Die Ergebnisse der Arbeit tragen zu einem besseren Verständnis von Licht-Metall-Wechselwirkungen in dreidimensionalen nah- und fernfeldgekoppelten plasmonischen Nanostrukturen bei und zeigen erste Möglichkeiten zu deren praktischer Anwendung auf.

ABSTRACT

The understanding of light-matter interactions at the nanoscale lay the groundwork for many future technologies, applications and materials. The scope of this thesis is the investigation of coupled photonic-plasmonic systems consisting of a combination of photonic microcavities and metallic nanostructures. In such systems, it is possible to observe an exceptionally strong coupling between electromagnetic light modes of a resonator and collective electron oscillations (plasmons) in the metal. Near-field coupled nanowire pairs were placed between two metal layers that form a microcavity. Depending on the position of the nanowires in the microcavity, electric as well as magnetic modes of the light can be coupled to symmetric and antisymmetric plasmon modes exhibiting electric and magnetic dipoles. The measured coupling strengths both in the electric and magnetic case are extremely high. If the nanostructures are placed close to the mirrors of the cavity, both localized particle plasmons as well as propagating surface plasmons at the interfaces of the metal can be excited and strongly coupled to the photonic light modes. Furthermore, a first possible application of the structures as sensors was explored. The results have shown, that coupled photonic-plasmonic structures possess a considerably higher sensitivity to changes in their environment than conventional localized plasmon sensors due to a plasmon excitation phase shift that is depending on the environment. The thesis includes theoretical models and simulations of near- and far-field coupled plasmonic systems to explain the observed phenomena. Furthermore, the experimental techniques for the fabrication and characterization of multilayer nanostructures are presented. The results of the thesis contribute to a better understanding of light-metal interactions in three-dimensional near- and far-field coupled plasmonic nanostructures and disclose possibilities of their initial practical use.

CONTENTS

Zusammenfassung	3
Abstract	5
Contents	7
1 Introduction	11
1.1 The Control of Light and Matter	11
1.2 Plasmonic Nanostructures	12
1.3 Outline	15
2 Electrodynamics of Bulk and Nanostructured Metals	17
2.1 Introduction	17
2.2 Bulk Metals	17
2.2.1 Quasi-Free Electron Model	18
2.2.2 Electrodynamic Properties of Gold	19
2.3 Metal Surfaces	21
2.3.1 Metal Mirrors and Metal Cavities	21
2.3.2 Surface Plasmons	24
2.4 Nanostructured Metals	27
2.4.1 Localized Plasmon Resonances	27
2.4.2 Metal Nanospheres	27
2.4.3 Metal Nanorods	29
2.4.4 Metal Nanowires	31
2.4.5 Damping, Linewidth, and Lifetime	31
2.5 Simulation Methods	32
2.5.1 Finite Difference Time Domain Method	33
2.5.2 Fourier Modal Method	33
3 Experimental Techniques	35
3.1 Introduction	35
3.2 Thin Layer Deposition	35

3.3	Etching	37
3.4	Nanostructuring	38
3.5	Spectroscopy	41
4	Plasmon Coupling	45
4.1	Introduction	45
4.2	Near-Field Coupling	46
4.2.1	Dipole Model	46
4.2.2	Plasmon Hybridization	47
4.2.3	Nanorod Pairs	48
4.2.4	Mirror Hybridization	50
4.3	Far-Field Coupling	52
4.3.1	Transition from Near- to Far-Field Coupling	52
4.3.2	Phase Shift Model	53
4.3.3	Nanostructured Cavities	55
4.3.4	Multilayer Stacks	57
5	Strong Coupling of Photonic and Localized Plasmon Modes	59
5.1	Introduction	59
5.2	Strong Coupling	59
5.2.1	Strong Coupling of Quantum Emitters and Light	59
5.2.2	Transition to Plasmonic Systems	61
5.3	Single Nanorods in a Microcavity	62
5.4	Nanorod Pairs in a Microcavity	63
5.4.1	Electric and Magnetic Coupling	63
5.4.2	Variation of Plasmon Position	64
5.4.3	Nature of the Modes	67
5.4.4	Fabrication Details	68
5.4.5	Experimental Results	69
5.4.6	Splitting Energies	71
5.5	Multilayer Nanorods in a Microcavity	72
6	Strong Coupling of Photonic and Surface Plasmon Modes	75
6.1	Introduction	75
6.2	Structure Geometry and Coupling Scheme	75
6.2.1	Excitation of Surface and Localized Plasmons	75
6.2.2	Enhancing Light-Plasmon Coupling by a Photonic Microcavity	77
6.2.3	Fabrication and Measurement Technique	77
6.2.4	Mode Splitting	80
6.3	Cavity-Assisted Far-Field Interactions	82

7	Cavity-Enhanced Plasmonic Sensing	83
7.1	Introduction	83
7.2	Localized Plasmon Resonance Sensing	83
7.2.1	General Principle	83
7.2.2	Structure Dependence	84
7.2.3	Characterization of Sensing Properties	85
7.3	Cavity-Enhanced Sensing	86
7.3.1	Linewidths and Sensing Principle	86
7.3.2	Phase Shifts	88
7.3.3	Optimal sensing structure parameters	89
7.3.4	Field Localization	91
7.3.5	Unit Cell Size and Incident Angle	91
7.4	Experimental Results	93
7.4.1	Sample Fabrication	93
7.4.2	Experimental Setup	93
7.4.3	Measured Spectra	94
7.4.4	Sensitivity and Figure of Merit	95
8	Conclusions	97
8.1	Summary	97
8.2	Outlook	98
	References	101
	List of Figures	111
	List of Abbreviations	113
	Publication List	115
	Curriculum Vitae	119
	Acknowledgements	121

1 INTRODUCTION

1.1 THE CONTROL OF LIGHT AND MATTER

The control of materials has governed the history of mankind. The earliest ages of human development were named after the materials that man was able to handle and use for his purposes: stone, bronze, iron. The control of new materials triggered not only technological and economic advances but implied often also cultural and social revolutions. Two million years ago, the usage of stone tools provided access to new sources of food and enabled the control over fire. The invention of the sword as well as the developing of trade networks, agriculture and animal husbandry took place at the beginning of the bronze age five thousand years ago. Later, iron facilitated the production of weapons and tools and enlarged their variations which formed the basis for the development of the first cities and ancient empires. Until the late middle ages, progress in material processing was dominated mostly by incidental discoveries, and no deeper understanding of matter existed. A good example for that is Damascus steel; a type of steel with superior properties, that was used for sword making from the twelfth century on. Some chance combinations of techniques and materials were probably the major contributions to its development. The recipe for the production got lost over the centuries but recently, large quantities of carbon nanotubes have been discovered in the steel's composition giving a possible explanation for its properties [99]. Definitely, ancient smiths did not have sufficient knowledge about matter to understand the processes they applied.

The early evolution of physics in the fields of mechanics, thermodynamics and electromagnetism as well as the transition from alchemy to chemistry changed this fundamentally and provided the groundwork for a rational understanding of matter. In the later history, when the large-scale use of refined coal enabled the development of improved iron- and steel-making techniques, this understanding led to new techniques and started the industrial revolution with all its implications on technology and society. Since the last century, the knowledge about matter has advanced in regions that opened up unimagined possibilities. The physics of elementary particles, atoms, molecules, and solid states provides detailed knowledge of the composition of matter on which the engineering of new alloys, silica, polymers, and carbon materials is based. The control of semiconductors had the greatest impact on the modern world's economy and lifestyle due to its usage in the manufacture of discrete electronic devices such as transistors, and in the development

of integrated circuits such as computer chips. The rapid advances are mainly based on the progress in miniaturization. Orders of magnitudes were conquered within only a few decades proceeding from the micro- to the nanoscale.

Today, at the beginning of the nanoage, the control of matter has made amazing progress. Atomic traps, nanotubes, molecular beam epitaxy or atomic layer deposition are just a few examples. The fabrication of nanostructures with photolithography as well as electron or ion beams has become a standard method in science and technology. On these scales, materials behave very differently which can be used as a fruitful approach to design new materials with mechanical, electrical, and optical properties not found in conventional materials. The interaction of light with matter is one major tool in the understanding and processing of materials. The observation of spectral lines was the starting point for our modern understanding of the composition of matter and spectroscopy has become the major method for material analysis. Finally, the evolution of laser physics enabled the ultimate control over the light. Ranging from macroscopic welding and cutting to nanoscopic photolithography, lasers have become an important tool in material treatment on all scales. In data communication, the photon is replacing the electron as the carrier of information; a process that will continue and offer great possibilities in information and computing technology. Rightly, the twenty-first century has often claimed to become the century of the photon.

Many fascinating effects, concepts and techniques in the control of light and matter at the smallest scales have been found, explained and applied and many more are still to be discovered. As always in fundamental research, the exact implications on the future cannot be anticipated. But definitely, the understanding and utilization of light-matter interactions at the nanoscale will be one of the basic building blocks for future materials, technologies and devices.

1.2 PLASMONIC NANOSTRUCTURES

“I have often struggled to perceive [...] to what extent experimental trials might be devised which, with their results and consequences, might contradict, confirm, enlarge or modify the idea we form of [...] that wonderful production of the human mind, the undulatory theory of light [...] Gold seemed especially fitted for experiments of this nature [...] because known phenomena appeared to indicate that a mere variation in the size of its particles gave rise to a variety of resultant colours.”

Michael Faraday, 1857 [28]

Since ancient times it has been known that metal dust can be used to color glasses. The technique has been applied by the Romans for the ornamentation of luxury goods, such as cups or in medieval times to color church windows [Fig. 1]. Michael Faraday



Figure 1: Small metal particles can be used to color glasses. The technique has been applied at the Lycurgus Cup, a Roman glass cage cup, or in church windows.

(1791-1867) was the first modern scientist to systematically investigate the optical properties of small metal particles and communicated his observations in his famous Bakerian lecture from 1857 [28]. Faraday was fascinated by the different colors of colloidal gold for his investigations on the relations between matter and electric, magnetic, and optical phenomena. His lecture, however, contained rather a mere description of the observed phenomena than a scientific explanation in a contemporary sense.

The first mathematical description of light interacting with small particles was given by Gustav Mie (1868-1957) [77] at the beginning of the twentieth century shortly after the first direct observation of microscopic particles by Richard Zsigmondy (1865-1929) [132] using his newly invented slit ultramicroscope. Mie explained consistent with Maxwell's equations how small particles sustain resonant modes that can be excited by electromagnetic waves. Apart from metallic particles, these collective oscillations of electrons can also be supported by metallic surfaces. In fact, these propagating surface plasmon polaritons have been first described by Sommerfeld in 1899 [109] in the context of radio waves propagating along the surface of a metal cylinder. A comprehensive theoretical treatment of surface plasmons in the context of loss spectra of diffracted electron beams at thin metallic films has been given by Ritchie in 1957 [101] before the first observation by Powell in 1960 [96]. Extensive experimental investigations concerning the optical excitation of surface plasmons followed in the next decades [86, 50, 102]. Complete treatments of localized particle plasmons and propagating surface plasmons and their interactions can be found in the books of Bohren and Huffman [10] or Kreibig and Vollmer [49].

The relevance of the field of plasmonics as an integral part of nanophotonics has emerged in the last two decades. The advances in particle synthesis and nanofabrication offer unique possibilities to produce structures with subwavelength dimensions [Fig. 2] with tailored optical properties (metamaterials). Such properties include refractive indices

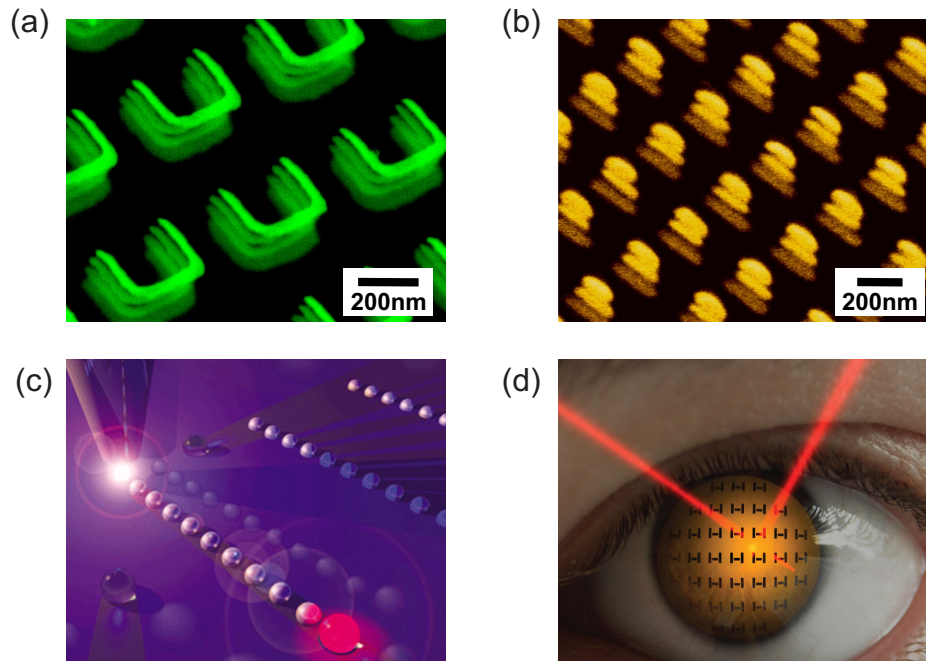


Figure 2: Examples for plasmonic applications: (a) Novel materials [61], (b) nanoantennas [23], (c) waveguides [72], and (d) sensors [66].

not observed in conventional materials which have led to many fascinating ideas such as the design of perfect lenses [89] or cloaking devices [90, 27]. Further applications include optical nanoantennas [80, 106, 23] or, more generally, active and passive components for (integrated) optical devices [131], like high-speed optical switches, tailored optical filters and gratings, nanoscale waveguides as well as coherent optical light sources [7, 87]. Furthermore, the technique of surface-enhanced Raman spectroscopy (SERS) has become a widely used method to study molecule spectra that is based on large field enhancements due to the excitation of localized plasmons. The enhanced near-fields of metallic nanoparticles can also be used to detect marginal changes in the environment which is crucial for sensing applications such as the detection of biomolecules [124, 51, 3].

In all mentioned fields, plasmonic devices consist of many metallic nanoparticles that interact with each other and the external light field all the time. The different components cannot be regarded as isolated elements, therefore the coupling between plasmons and the coupling of light to plasmons decisively determines the properties and functionality of the applications. So, the questions that we have to ask ourselves are: What are the exact coupling mechanisms for different particle distances, especially with respect to three-dimensional geometries? How can we manipulate both coupling strength and range as well as the resonance linewidths and how can we utilize these modifications to improve plasmonic devices?

1.3 OUTLINE

The thesis begins with a general introduction into the basics of the description of conductive solid states and their interactions with light [Ch. 2]. After the derivation of the optical properties of metals using the quasi-free electron model, the effects of the transition from bulk metal to thin metal layers and finally to metallic nanostructures are explained. The focus will be on the optical properties of gold and on the reflection of electromagnetic waves at thin gold layers. Also, a consideration of microresonators consisting of thin gold layers is included. Finally, the basics of propagating surface plasmons and of localized particle plasmons in different structures are reviewed. After that, the methods to simulate the behavior of multilayer nanostructures and the experimental techniques used to fabricate and characterize them are introduced [Ch. 3]. The presented experimental methods include the deposition of thin dielectric and metal layers as well as etching methods and nanostructuring processes using electron beam lithography. The method of Fourier transform infrared spectroscopy used for the characterization of the fabricated samples is briefly explained.

Essential for the later understanding is a detailed description of plasmon-plasmon and light-plasmon coupling [Ch. 4]. Models to describe and intuitively understand the behavior of plasmonic elements that are coupled both via the near- and the far-field are developed. The model of plasmon hybridization and a consideration of phase shifts provide the basis for the understanding of near-field coupled nanorod and nanowire pairs as well as far-field coupled nanostructured layers that form cavities with resonant mirrors. The optical properties of nanostructured layers are modeled using a resonant dielectric function which helps to understand the behavior of the resonant modes of coupled photonic-plasmonic systems. Furthermore, an extension to multilayer structures is included to give an impression of the characteristics of three-dimensional plasmonic structures.

The first experimentally observed effect involves strong coupling of localized plasmonic modes to photonic modes that could be achieved by placing plasmonic nanorods into a photonic microcavity [Ch. 5]. The investigation of the effects of changing the nanorod positions in the microcavity as well as changing the cavity length reveal the coupling mechanisms of the electric and magnetic fields of the confined light modes to the symmetric and antisymmetric plasmon modes. In the next chapter [Ch. 6], the concept is extended to strong coupling of surface plasmons to light modes by placing nanowires close to the mirrors that form the microcavity. This way, the photonic light modes excite localized plasmons that can induce surface plasmons on the cavity mirrors. By applying external pressure to the microcavity, the behavior of the system is investigated for different resonator lengths. Furthermore, a model of cavity-induced far-field interactions of plasmons is illustrated.

Finally, a first application of the investigated structures is presented [Ch. 7]. It implies the use of a coupled photonic-plasmonic structure as a refractive index sensor featuring

enhanced sensing properties compared to conventional plasmon sensors. Nanorods that are placed at Bragg-distance above a mirror exhibit a resonance with a decreased linewidth and a strong phase dependence of the plasmon excitation. This way, the sensing properties are very much improved. The experimental setup to measure the sensitivity of the fabricated samples using different liquids is demonstrated. The experimentally obtained results are presented and compared with the theoretical predictions.

2 ELECTRODYNAMICS OF BULK AND NANOSTRUCTURED METALS

2.1 INTRODUCTION

In the following sections, the basic models and concepts for the description of the electromagnetic properties of bulk metals, thin metal layers, and metal nanostructures are reviewed. The first successful attempts in deriving the optical properties of solid states have been carried out by Sommerfeld and Drude [25] using the quasi-free electron model. The basics of this model are described in the first section. Since this simple model has strong limitations, a section covering the properties of real metals, particularly gold, is included in this chapter. After examining the effects of light impinging on metal-dielectric interfaces in the context of microresonators and surface plasmon excitation, the focus will be on localized plasmon resonances in metal nanostructures. As already pointed out in Ch. 1, it has been known a long time that the optical properties of small metallic particles differ substantially from those of bulk metal. Starting from a quasi-static approach to derive the resonance conditions for subwavelength metal spheres as well as their scattering and absorption characteristics, we continue with comparing different simple nanoparticle geometries and illustrate the effects of varying the geometric and environmental parameters. A short section covering the time-dependent characteristics lifetime and damping is next. The chapter is closed with the different simulation methods used for the calculations of the optical properties of the investigated structures in this thesis. The subsequent considerations are following partly the approaches found in the books of Bohren and Huffmann [10], Kreibig and Vollmer [49], Maier [69], as well as Sarid and Challener [103].

2.2 BULK METALS

For the purposes of this thesis, it is sufficient to describe the interactions of electromagnetic waves with solid states in the framework of classical electrodynamics. Although dealing with extremely small structures later on, quantum effects can still be safely neglected. Furthermore, the very dispersive properties of metals will be described using a macroscopic, phenomenological approach by introducing the complex dielectric function $\epsilon(\omega)$ that includes the average effects of the microscopic electromagnetic interactions in

a solid state. The considerations are limited to linear, isotropic, and non-magnetic materials.

2.2.1 QUASI-FREE ELECTRON MODEL

The quasi-free electron model (also called plasma model or Drude-Sommerfeld model [25]) is a very simple approach to describe the motions of electrons in a metal and to derive the optical properties of the metal. It is based on the kinetic gas theory and regards the electrons as moving independently and freely against a fixed background of positive ions. The electron-electron interactions as well as the electron-lattice interactions are accounted for in a damping parameter γ_e in the equation of motion for the electrons in the plasma. An effective mass m_e for the electrons includes corrections originating from the band structure of the metals, whereas interband transitions are completely neglected limiting the validity of the model. The motion of the electrons is thus given by

$$m_e \ddot{\vec{r}} + m_e \gamma_e \dot{\vec{r}} = -e \vec{E}. \quad (2.1)$$

The solution of this damped harmonic oscillator differential equation for a harmonic driving electric field $\vec{E}(t) = \vec{E}_0 e^{-i\omega t}$ as from an electromagnetic wave is

$$\vec{r}(t) = \frac{e}{m_e (\omega^2 + i\gamma_e \omega)} \vec{E}(t) \quad (2.2)$$

where $r(t) = \vec{r}_0 e^{-i\omega t}$ with the complex amplitude \vec{r}_0 including phase shifts between driving force and response. The macroscopic polarization $\vec{P} = -n_e e \vec{r}$ of a metal with the electron density n_e is given by

$$\vec{P} = -\frac{n_e e^2}{m_e (\omega^2 + i\gamma_e \omega)} \vec{E}. \quad (2.3)$$

The combined effect of an external electric field \vec{E} and a macroscopic internal polarization \vec{P} is given by the dielectric displacement

$$\vec{D} = \epsilon_0 \vec{E} + \vec{P} \quad (2.4)$$

with ϵ_0 being the electric permittivity of vacuum. For low field strengths, the relation between the polarization and the electric field is linear (as assumed in the quasi-free electron model in Eq. 2.3). Hence, the macroscopic polarization can be written as $\vec{P} = \epsilon_0 \chi \vec{E}$ with the dielectric susceptibility χ . Introducing the material specific (and frequency dependent) electric permittivity $\epsilon = 1 + \chi$, Eq. 2.4 takes the form

$$\vec{D} = \epsilon_0 \epsilon \vec{E}. \quad (2.5)$$

With Eq. 2.3 one then obtains

$$\vec{D} = \epsilon_0 \left(1 - \frac{n_e e^2}{\epsilon_0 m_e (\omega^2 + i\gamma_e \omega)} \right) \vec{E}. \quad (2.6)$$

With the plasma frequency $\omega_p = \sqrt{\frac{n_e e^2}{\epsilon_0 m_e}}$, the complex dielectric function becomes

$$\epsilon(\omega) = 1 - \frac{\omega_p^2}{\omega^2 + i\gamma_e \omega} \quad (2.7)$$

with the real and imaginary parts

$$\epsilon(\omega) = \text{Re}[\epsilon(\omega)] + i \cdot \text{Im}[\epsilon(\omega)] = \left(1 - \frac{\omega_p^2}{\gamma_e^2 + \omega^2}\right) + i \left(\frac{\omega_p^2 \gamma_e}{\omega(\omega^2 + \gamma_e^2)}\right). \quad (2.8)$$

It is interesting to look at the high and low frequency limits. If $\omega \gg \gamma_e$ (but still $\omega < \omega_p$), the damping can be neglected and the metal behaves like a free electron plasma. However, in real metals [Sec. 2.2.2] interband transitions rule the metal behavior leading to a high imaginary part of the dielectric function. For the low frequency limit $\omega \ll \gamma_e$, the imaginary part $\text{Im}[\epsilon(\omega)]$ increases dramatically, and the metals become absorbing and are characterized by their skin depth.

The dielectric function $\epsilon(\omega)$ is linked to the conductivity $\sigma(\omega)$ of a material by

$$\epsilon(\omega) = 1 + \frac{i\sigma(\omega)}{\epsilon_0 \omega} \quad (2.9)$$

and to the (complex) refractive index by

$$\epsilon(\omega) = n(\omega)^2. \quad (2.10)$$

2.2.2 ELECTRODYNAMIC PROPERTIES OF GOLD

As already mentioned in the introduction of this chapter, simple models as the quasi-free electron model have limitations in their validity. Since gold is the metal used for the fabrication of all metal nanostructures and thin metal layers in this thesis, this section covering the properties of “real” gold and comparing them to the model is included.

In Figs. 3 and 4, measured optical properties of gold layers from Johnson and Christy [46] and from Thèye [115] are compared with theoretical values from the quasi-free electron model in the near-infrared and visible spectrum. The thickness of the measured gold films was in the range of a few tens of nanometers. According to Johnson and Christy [46], the properties of films thicker than 25 nm correspond to those of bulk metal. As soon as interband transitions occur below wavelengths of around 650 nm, the quasi-free electron model totally loses its validity. Since the increase in absorption in this range also inhibits the excitation of localized plasmon excitations, the quasi-free electron model was used for simulations of gold throughout the thesis. The material constants ω_p and γ_e determining the dielectric function $\epsilon(\omega)$ can be obtained by fitting theoretical curves to the measured data. A lot of measured data has been published and, unfortunately, the derived

material parameters vary a lot. The main reason for this variation lies in the consideration of a limited spectral area [85].

The interesting spectral range for the experiments of this thesis [Fig. 4] is the near-infrared range from wavelengths of 700 nm up to 2000 nm corresponding to a frequency range from 150 THz to 400 THz. Regarding only this range, a fit of the measured data results in the following values for the plasma frequency ω_p and the damping frequency γ_e that are used for all simulations throughout this thesis:

$$\omega_p = 1.31 \cdot 10^{16} \text{ Hz}, \quad (2.11)$$

$$\gamma_e = 1.26 \cdot 10^{14} \text{ Hz}, \quad (2.12)$$

$$\epsilon_\infty = 8. \quad (2.13)$$

The parameter ϵ_∞ accounts for a highly polarized environment of the free s electrons in the high frequency limit caused by the filled d band close to the Fermi surface. This additional polarization $\vec{P}_\infty = \epsilon_0 (\epsilon_\infty - 1) \vec{E}$ changes Eq. 2.7 to

$$\epsilon(\omega) = \epsilon_\infty - \frac{\omega_p^2}{\omega^2 + i\gamma\omega}. \quad (2.14)$$

Nevertheless, the fabrication method and final condition of the metal layer or nanostructure in terms of surface roughness, homogeneity and purity has an influence on the optical parameters that cannot be predicted. This is one important reason for the deviations between experimental and simulated spectra.

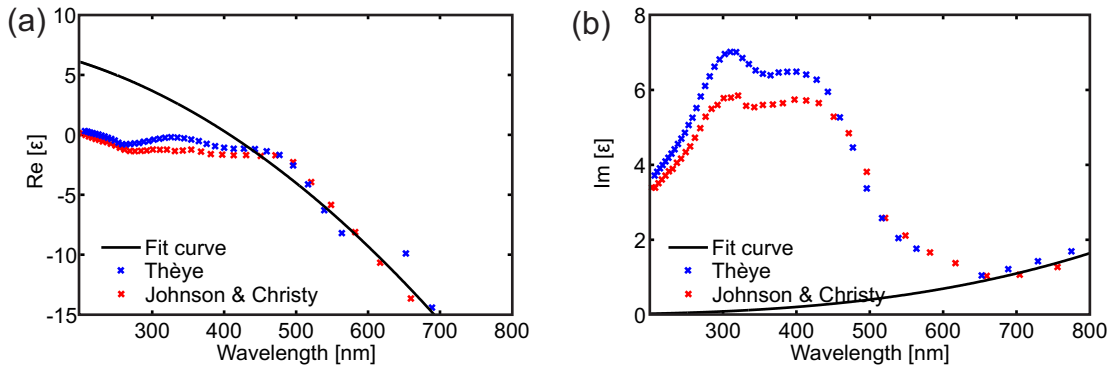


Figure 3: (a) Real part $\text{Re}[\epsilon(\omega)]$ and (b) imaginary part $\text{Im}[\epsilon(\omega)]$ of the dielectric function of gold. The fit of the quasi-free electron model corresponds to the measured data only for wavelength higher than 650 nm where no interband transitions occur.

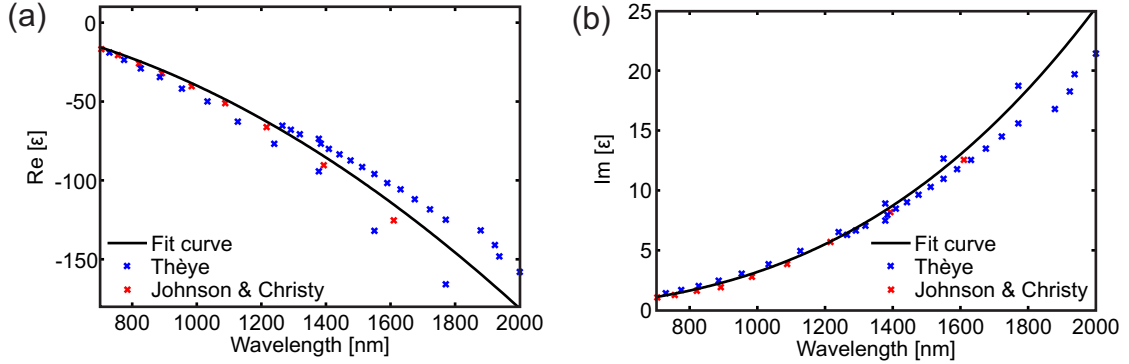


Figure 4: For the relevant spectral range of this thesis (700 nm to 2000 nm) the agreement between measured and fitted curves of (a) the real part $\text{Re}[\epsilon]$ and (b) the imaginary part $\text{Im}[\epsilon]$ of the dielectric function of gold is very good.

2.3 METAL SURFACES

2.3.1 METAL MIRRORS AND METAL CAVITIES

The dispersive response of metal to an electromagnetic wave determines the different effects that occur at the surfaces of metals or metal-dielectric interfaces. For low frequencies, metals can be regarded as perfect conductors. When the frequency increases towards the near-infrared and visible region, the penetration depth of the electromagnetic wave into the metal can no longer be omitted and plays an important role for the reflectivity and the phase shifts occurring upon reflection. For higher ultraviolet frequencies, some metals even become transparent as long as interband transitions do not absorb the light.

The effects on light that is reflected from metal surfaces play an important role when using microresonators that consist of reflecting metal layers. In general, microcavities can be used to confine electromagnetic waves to very small regions and to enhance the interactions of light with emitters [see also Sec. 5]. A microcavity consists of two reflectors at a distance in the order of the wavelength. The simplest way is using two thin metal layers as mirrors. For cavities where higher Q-factors are of importance, multi-layer Bragg mirrors can be used.

The resonance frequency of a microcavity depends on the distance of the mirrors d as well as on the optical properties of the materials in and around the cavity. In particular, the phase shifts that occur upon reflection of the confined electromagnetic wave at a mirror play an important role. If we assume a cavity consisting of two perfectly conducting metal mirrors at a distance d [Fig. 5(b)], the electric field at the metal-dielectric interfaces is 0 (electric field nodes) and the resonance wavelengths λ_N can be calculated as

$$\lambda_N = \frac{2n_{\text{cav}}d}{N} \quad (2.15)$$

where n_{cav} is the refractive index of the material inside the cavity and N is a positive

integer. The phase shift upon reflection at a perfect conductor is $\Delta\varphi_{\text{refl}} = \pi$. For real metals, however, the reflection phase shift can be substantially different from π . It can be calculated using the Fresnel formulas. Assuming that the imaginary part of the refractive index of the dielectric medium $\text{Im}[n_{\text{cav}}]$ is 0 and the metal has a complex refractive index of n_{met} , the complex reflection coefficient R can be calculated as [44]

$$R = \frac{E_{\text{refl}}}{E_{\text{inc}}} = |R|e^{i\Delta\varphi_{\text{refl}}} = \frac{n_{\text{cav}} - n_{\text{met}}}{n_{\text{cav}} + n_{\text{met}}} \quad (2.16)$$

with the complex electric field amplitudes of the incident wave E_{inc} and the reflected wave E_{refl} . The phase shift $\Delta\varphi_{\text{refl}}$ can then be calculated as

$$\Delta\varphi_{\text{refl}} = \arctan \frac{\text{Im}[R]}{\text{Re}[R]} = \arctan \frac{2n_{\text{cav}} \text{Im}[n_{\text{met}}]}{\text{Re}[n_{\text{met}}]^2 + \text{Im}[n_{\text{met}}]^2 - n_{\text{cav}}^2}. \quad (2.17)$$

To calculate the resonance wavelengths λ_N of a cavity, two points of view can be taken. The first way implies the assumption that the cavity has a larger resonator length due to the penetration depth of the wave into the metal [Fig. 5(c)]. The resonance wavelengths can then be calculated using

$$2(n_{\text{cav}}d + \delta) = N \cdot \lambda_N \quad (2.18)$$

with δ being the apparent length increase of the cavity ¹. The second possibility is regarding the phase shifts that occur during propagation and reflection of the wave in the cavity [Fig. 5(d)]. The total phase shift $\Delta\varphi_{\text{tot}}$ that a wave accumulates during one round trip in the resonator system is the sum of the phase shifts due to propagation $\Delta\varphi_{\text{prop}}$ and on reflection $\Delta\varphi_{\text{refl}}$. The sum has to be a multiple of 2π for the wave to be resonantly enhanced. Thus, the resonance condition reads

$$\Delta\varphi_{\text{tot}} = 2 \cdot \Delta\varphi_{\text{prop}} + 2 \cdot \Delta\varphi_{\text{refl}} \quad (2.19)$$

$$= 2 \cdot \frac{2\pi \cdot n_{\text{cav}}d}{\lambda_N} + 2 \cdot \Delta\varphi_{\text{refl}} = (N + 1) \cdot 2\pi, \quad (2.20)$$

and the resonance wavelength is

$$\lambda_N = \frac{2n_{\text{cav}}d}{(N + 1) - \frac{\Delta\varphi_{\text{refl}}}{\pi}} \quad (2.21)$$

which reduces to Eq. 2.15 for $\Delta\varphi_{\text{refl}} = \pi$. Combining Eqs. 2.18 and 2.21, one obtains the relation between apparent length increase and reflection phase shift

$$\delta = \frac{\lambda_N}{2} \left(\frac{\Delta\varphi_{\text{refl}}}{\pi} - 1 \right). \quad (2.22)$$

More detailed treatments of microcavities can be found for example in [58], [31] or [68].

¹Please note that the apparent length increase δ is not equal to the actual penetration depth of the wave into the metal. The penetration depth depends on $\text{Im}[n_{\text{met}}]$ and is defined as the distance from the metal surface where the amplitude of the incident wave has exponentially decreased to $1/e$ of its original value at the surface.

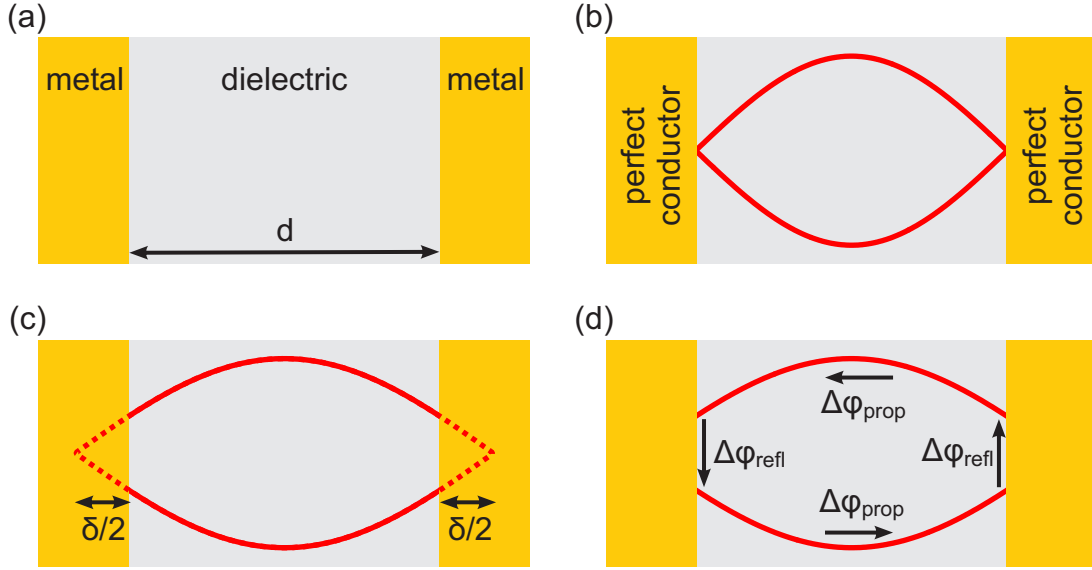


Figure 5: (a) Microcavity consisting of a dielectric and two metal mirrors. (b) No field penetration for perfect conductor metals. (c) Apparent length increase and (d) phase shifts for real metals.

Assuming a microcavity with thin metal layers acting as mirrors, we also have to take the thickness of the metal layers into account. Reflections on the outer metal-dielectric interface have an influence on the cavity resonance due to the effects of multibeam interferences. Therefore, also the materials surrounding the cavity, for example glass and air, play an important role, and the Fresnel amplitude reflection coefficient takes a more complicated form. In Fig. 6, the dependence of the resonance wavelength of a microcavity on the resonator length d and the mirror thickness t is plotted. The regarded resonator consists of a dielectric material with a refractive index of $n_{\text{cav}} = 1.40$, two gold layers with varying thickness t as mirrors surrounded by glass ($n_{\text{sub}} = 1.45$) on the one side and air ($n = 1$) on the other. For the simulated gold, the quasi-free electron model with the parameters from Sec. 2.2.2 was assumed. The calculations were performed using a transfer matrix method to account for the reflections on each layer. For comparison, the results for perfect conducting mirrors are included. The general shift to higher wavelengths for real cavities compared to ideal ones is the aforementioned “apparent length increase” δ . For the regarded system, this increase is around 50 nm in the near-infrared which corresponds to phase shifts on reflection of $\Delta\phi_{\text{refl}} = 220^\circ$ for $\lambda = 700$ nm and to $\Delta\phi_{\text{refl}} = 192^\circ$ for $\lambda = 2000$ nm. Thin metal layers ($t < 50$ nm) shift the resonances further to higher wavelengths. In conclusion, when calculating resonance wavelengths from resonator lengths or vice versa, one always has to keep in mind the effects of reflections on real metals which can differ substantially from those of perfect conductors.

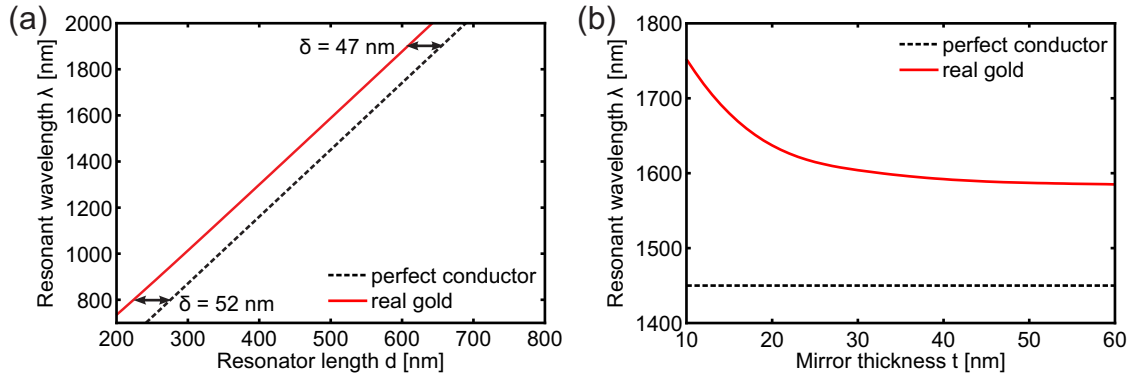


Figure 6: Comparison of a metal-dielectric-metal cavity with perfect conducting mirrors and “real” gold mirrors leading to an apparent length increase δ . Resonance wavelengths for (a) different mirror distances d (infinite mirror thickness t) and (b) different mirror thicknesses t (mirror distance $d = 500$ nm).

2.3.2 SURFACE PLASMONS

This section provides a brief review on the theory and the excitation of surface plasmons. More extensive treatments can be found for example in [93], [69], or [98].

Surface plasmons are electromagnetic modes trapped on a metal-dielectric interface. They can only be excited by p-polarized waves. Let us assume a coordinate system as in Fig. 7 with a metal-dielectric interface located in the x - y -plane at $z = 0$. The upper half space ($z > 0$) is filled with a dielectric material characterized by the permittivity ϵ_d and the lower half space ($z < 0$) consists of a metal (ϵ_m). A p-polarized wave is incident from the dielectric side with a \vec{k} -vector in the x - z -plane with the components k_x and k_z . Hence, the wave consists only of the electric field components E_x and E_z and the magnetic field component H_y . The electric and magnetic fields of a possibly excited wave propagating

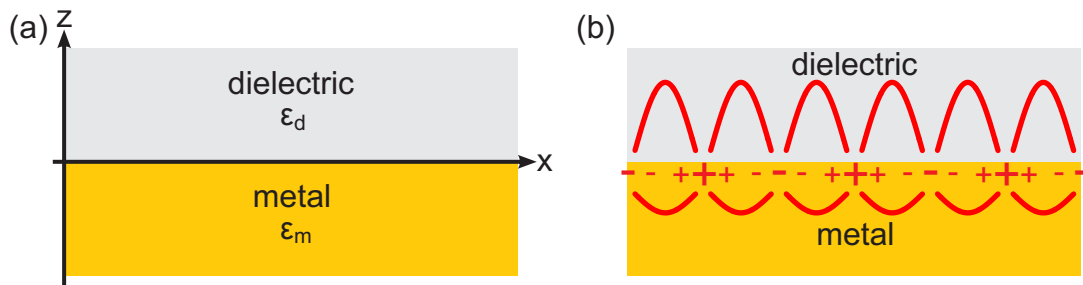


Figure 7: (a) Metal-dielectric interface in the x - y -plane at $z = 0$. (b) Surface plasmons (collective charge oscillations) at the metal-dielectric interface propagating in x -direction.

on the metal-dielectric interface then take the general form [102]

$$\vec{E}_m = (E_{x,m}, 0, E_{z,m}) e^{i(k_x x + k_{z,m} z - \omega t)} \quad (2.23)$$

$$\vec{H}_m = (0, H_{y,m}, 0) e^{i(k_x x + k_{z,m} z - \omega t)} \quad (2.24)$$

$$\vec{E}_d = (E_{x,d}, 0, E_{z,d}) e^{i(k_x x + k_{z,d} z - \omega t)} \quad (2.25)$$

$$\vec{H}_d = (0, H_{y,d}, 0) e^{i(k_x x + k_{z,m} z - \omega t)} \quad (2.26)$$

where the indices m and d represent the metallic and the dielectric half space. Applying Maxwell's equations $\vec{\nabla} \cdot \vec{E} = 0$ and $\vec{\nabla} \times \vec{E} = -\mu \frac{\partial \vec{H}}{\partial t}$ as well as the boundary conditions at $z = 0$ where the tangential components of the field must be continuous ($E_{x,m} = E_{x,d}$ and $H_{y,m} = H_{y,d}$), one obtains the relations

$$\frac{\epsilon_m}{k_{z,m}} = \frac{\epsilon_d}{k_{z,d}} \quad (2.27)$$

and

$$k_{z,d} = -i \sqrt{k_x^2 - \epsilon_d k^2} \quad (2.28)$$

$$k_{z,m} = +i \sqrt{k_x^2 - \epsilon_m k^2} \quad (2.29)$$

with $k = \frac{\omega}{c}$. In order to have exponential decay in z -direction, $k_{z,m}$ and $k_{z,d}$ have to be imaginary and with opposite sign, more precisely the conditions $ik_{z,d} > 0$ and $ik_{z,m} < 0$ have to be fulfilled. Therefore, also ϵ_m and ϵ_d have to be of opposite sign as it is the case for a dielectric and a metal. Combining Eqs. 2.27, 2.28, and 2.29 gives the dispersion relation of surface plasmons propagating at a metal-dielectric interface

$$k_x = k \sqrt{\frac{\epsilon_m \epsilon_d}{\epsilon_m + \epsilon_d}}. \quad (2.30)$$

For a propagating wave, k_x would have to be real which would be the case for $|\epsilon_m| > \epsilon_d$ if ϵ_m and ϵ_d were both real. However, for a metal we usually have $\text{Im}[\epsilon_m] > 0$ which causes surface plasmons to be damped also in their propagation direction.

Comparing the dispersion diagrams of surface plasmons and photons [Fig. 8(a)], one can see that the two curves do not cross, meaning there is no direct excitation of surface plasmons by incident electromagnetic waves and no direct decay of surface plasmons into free electromagnetic waves. For large wave vectors k_x , the frequency of the surface plasmons approaches the characteristic surface plasmon frequency ω_{SP} that can be derived by inserting the quasi-free electron model dielectric function Eq. 2.7 in the surface plasmon dispersion relation Eq. 2.30

$$\omega_{\text{SP}} = \frac{\omega_p}{\sqrt{1 + \epsilon_d}}. \quad (2.31)$$

Radiative excitation of surface plasmons requires certain tricks. One way is using total internal reflection of electromagnetic waves in a dielectric with a high permittivity

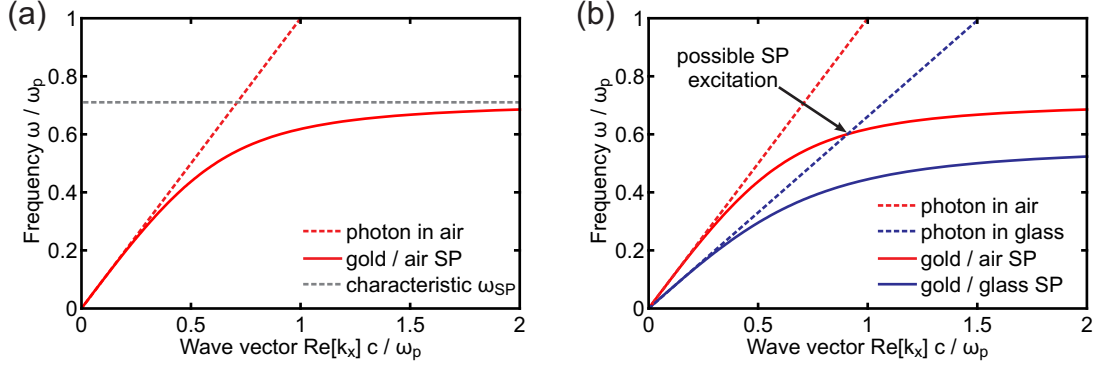


Figure 8: (a) Dispersion relation of a surface plasmon (SP) at a gold-air interface compared to that of a photon in air and the characteristic surface plasmon frequency ω_{SP} . (b) Comparison of the dispersion relations of surface plasmons at a gold-air and a gold-glass ($n_{\text{sub}} = 1.5$) interface. Optical surface plasmon excitation is possible when photon and surface plasmon dispersion relations intersect [see configurations in Fig. 9].

ϵ_{high} . Surface plasmons can then be excited on the interface of a thin metal layer and a dielectric with a low permittivity (for example air) when this interface is located very close to the high-permittivity material surface, usually a prism. In such a configuration, photons reflected internally in the prism under the angle θ have the in-plane momentum $k_x = \sqrt{\epsilon_{\text{high}}}\sin\theta$ which is sufficient to excite surface plasmons at, for example, a metal-air interface [Fig. 8(b)], when photons can tunnel the distance to this interface. Two different configurations exist. The Otto-configuration [86] [Fig. 9(a)] consisting of a prism and a metal layer with a thin air or dielectric gap in between and the Kretschmann-configuration [50] [Fig. 9(b)] with a thin metal layer located directly on the prism bordered by air or another dielectric on the other side.

A second possibility of surface plasmon excitation implies the use of gratings [Fig. 9(c)]. The momentum of the surface plasmons k_x can be matched with the photon in-plane momentum $k_{\parallel} = k_{\gamma}\sin\theta$ by “back-folding” of the dispersion curves. A surface plasmon can

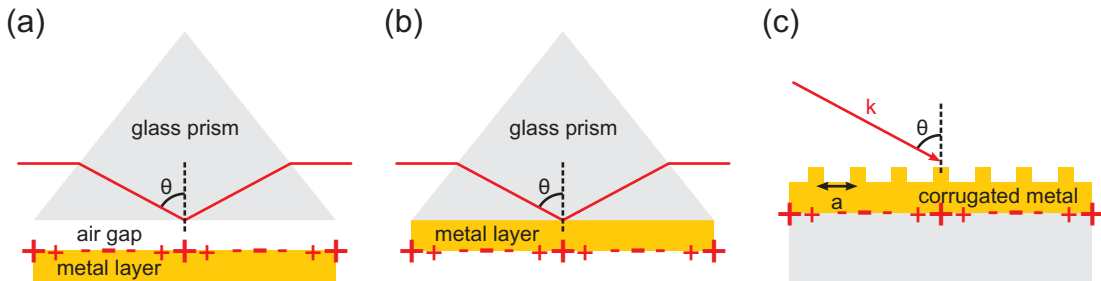


Figure 9: Surface plasmon excitation in the (a) Otto-configuration, (b) Kretschmann-Raether-configuration, and (c) using a grating.

be excited whenever the condition

$$k_x = k_y \sin \theta \pm N \frac{2\pi}{a} \quad (2.32)$$

is fulfilled, where N is an integer and a is the periodicity of the grating.

2.4 NANOSTRUCTURED METALS

2.4.1 LOCALIZED PLASMON RESONANCES

Non-propagating surface plasmons, usually referred to as localized plasmons or sometimes particle plasmons, can be excited in subwavelength metal nanoparticles. In contrast to propagating surface plasmons, localized plasmons can be excited directly by an electromagnetic wave incident on the particle [Fig. 10]. The oscillating external electric field drives the conduction electrons in the nanoparticle whereas the surface represents the restoring force. Gold nanoparticles at sizes of around 100 nm to 1 μ m exhibit resonances in the near-infrared and optical spectrum producing the well-known colorful effects described in Sec. 1.2.

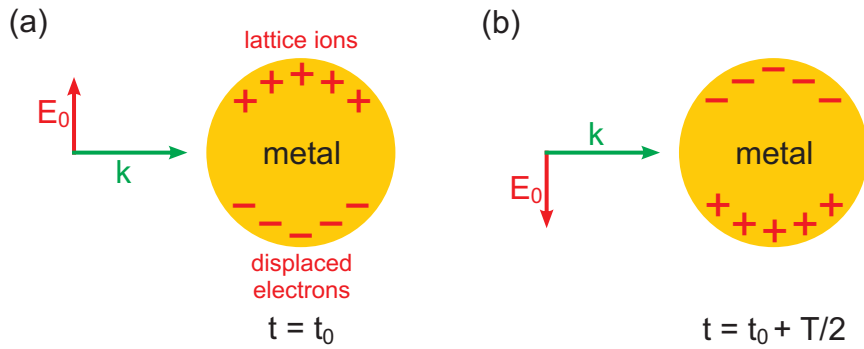


Figure 10: An incident electromagnetic wave excites a localized plasmon in a metal nanosphere. The charge distributions at (a) $t = t_0$ and (b) half a period later at $t = t_0 + \frac{T}{2}$ with $T = \frac{2\pi}{\omega}$ are displayed.

Localized plasmons in sufficiently small particles ($\ll \lambda$) can be described using a quasi-static approximation. The phase of the incident electromagnetic wave is assumed to be spatially constant over the whole particle volume. The harmonic time dependence can be added in the end to the solution of the electrostatic problem.

2.4.2 METAL NANOSPHERES

For the simplest possible structure, a nanosphere, analytical solutions for the localized plasmon resonance wavelength exist. Let us assume a sphere with radius R located at

the origin of a coordinate system in the presence of an external homogeneous electric field $\vec{E}_0 = (0, 0, E_0)$ [Fig. 11]. The sphere consists of a metal with the dielectric function $\epsilon_m(\omega)$ and is surrounded by a dielectric material ϵ_d . Due to the electrostatic field, charges are induced on the surface of the sphere. This electrostatic problem can be solved using a Legendre-polynomial approach and applying the boundary conditions at $r = R$. The potentials inside and outside the sphere take the form [10]

$$\Phi_m = -\frac{3\epsilon_d}{\epsilon_m + 2\epsilon_d} E_0 r \cos \theta \quad (r \leq R) \quad (2.33)$$

$$\Phi_d = -E_0 r \cos \theta + R^3 E_0 \frac{\epsilon_m - \epsilon_d}{\epsilon_m + 2\epsilon_d} \frac{\cos \theta}{r^2} \quad (r > R). \quad (2.34)$$

Comparing this with the potential of an ideal dipole (embedded in a medium with permittivity ϵ_d)

$$\Phi_p = \frac{\vec{p} \cdot \vec{r}}{4\pi\epsilon_0\epsilon_d r^3} = \frac{p \cos \theta}{4\pi\epsilon_0\epsilon_d r^2}, \quad (2.35)$$

one recognizes that the potential outside the sphere Φ_d is a superposition of the potential of the external electric field \vec{E}_0 and the potential of an ideal dipole with the dipole moment

$$\vec{p} = 4\pi\epsilon_0\epsilon_d R^3 \frac{\epsilon_m - \epsilon_d}{\epsilon_m + 2\epsilon_d} \vec{E}_0 \quad (2.36)$$

located at the sphere center. Using $\vec{E} = -\vec{\nabla}\Phi$, the electric fields inside and outside the sphere are given by

$$\vec{E}_m = \frac{3\epsilon_d}{\epsilon_m + 2\epsilon_d} \vec{E}_0 \quad \text{and} \quad (2.37)$$

$$\vec{E}_d = \vec{E}_0 + \frac{1}{4\pi\epsilon_0\epsilon_d} \frac{1}{r^3} (3\vec{r}p \cos \theta - \vec{p}). \quad (2.38)$$

With $\vec{p} = \epsilon_0\epsilon_d\alpha\vec{E}_0$ the polarizability α is

$$\alpha = 4\pi R^3 \frac{\epsilon_m - \epsilon_d}{\epsilon_m + 2\epsilon_d}. \quad (2.39)$$

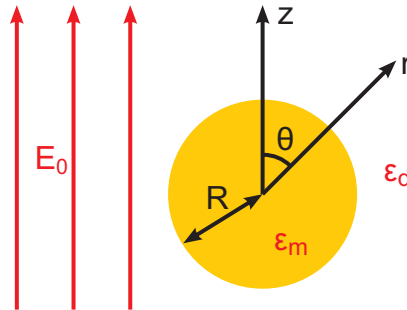


Figure 11: Metal nanosphere located at the origin in a homogeneous static electric field.

The polarizability is resonantly enhanced at the minimum of $|\epsilon_m + 2\epsilon_d|$ which leads for small $\text{Im}[\epsilon_m]$ to the Fröhlich condition

$$\text{Re}[\epsilon_m] = -2\epsilon_d. \quad (2.40)$$

For a metal described by a Drude model the localized plasmon resonance frequency of a nanosphere in vacuum is then given by

$$\omega_{\text{LP}} = \frac{\omega_p}{\sqrt{3}}. \quad (2.41)$$

The internal field E_m as well as the external dipolar field are resonantly enhanced when the condition of Eq. 2.40 is fulfilled. The harmonic time dependence can finally be multiplied to the fields leading to a scattering of the electromagnetic wave by the sphere that is represented by an electric point dipole

$$\vec{p} = \epsilon_0 \epsilon_d \alpha \vec{E}_0 e^{-i\omega t}. \quad (2.42)$$

The expressions for the scattering, absorption and extinction cross-sections derived by Bohren and Huffmann [10] take the form

$$C_{\text{abs}} = k \text{Im}[\alpha] = 4\pi k R^3 \text{Im} \left[\frac{\epsilon_m - \epsilon_d}{\epsilon_m + 2\epsilon_d} \right] \quad (2.43)$$

$$C_{\text{scat}} = \frac{k^4}{6\pi} |\alpha|^2 = \frac{8\pi}{3} k^4 R^6 \left| \frac{\epsilon_m - \epsilon_d}{\epsilon_m + 2\epsilon_d} \right|^2 \quad (2.44)$$

$$C_{\text{ext}} = C_{\text{abs}} + C_{\text{scat}} = 12\pi \frac{\omega}{c} R^3 \frac{\epsilon_d^{3/2} \text{Im}[\epsilon_m]}{(\text{Re}[\epsilon_m] + 2\epsilon_d)^2 + (\text{Im}[\epsilon_m])^2} \quad (2.45)$$

with $k = \frac{2\pi}{\lambda}$. The cross-sections exhibit resonance maxima at the same frequencies as the polarizability. By spectral transmittance or reflectance measurements, the resonant frequencies of the nanoparticles can easily be determined experimentally. For a good signal, the measurements are usually performed at arrays of particles rather than at single particles.

2.4.3 METAL NANORODS

An analytical treatment of geometries other than spherical leads to complicated expressions very soon. Bohren and Huffmann [10] provide formulas for ellipsoidal particles, and detailed calculations of nanorods in the context of nanoantennas can be found in the paper of Novotny et al. [84]. The best tool of investigating nanorods are simulations [Sec. 2.5], and this section is limited to the investigation of the influence of structural parameters on the localized plasmon resonances of nanorods using simulations.

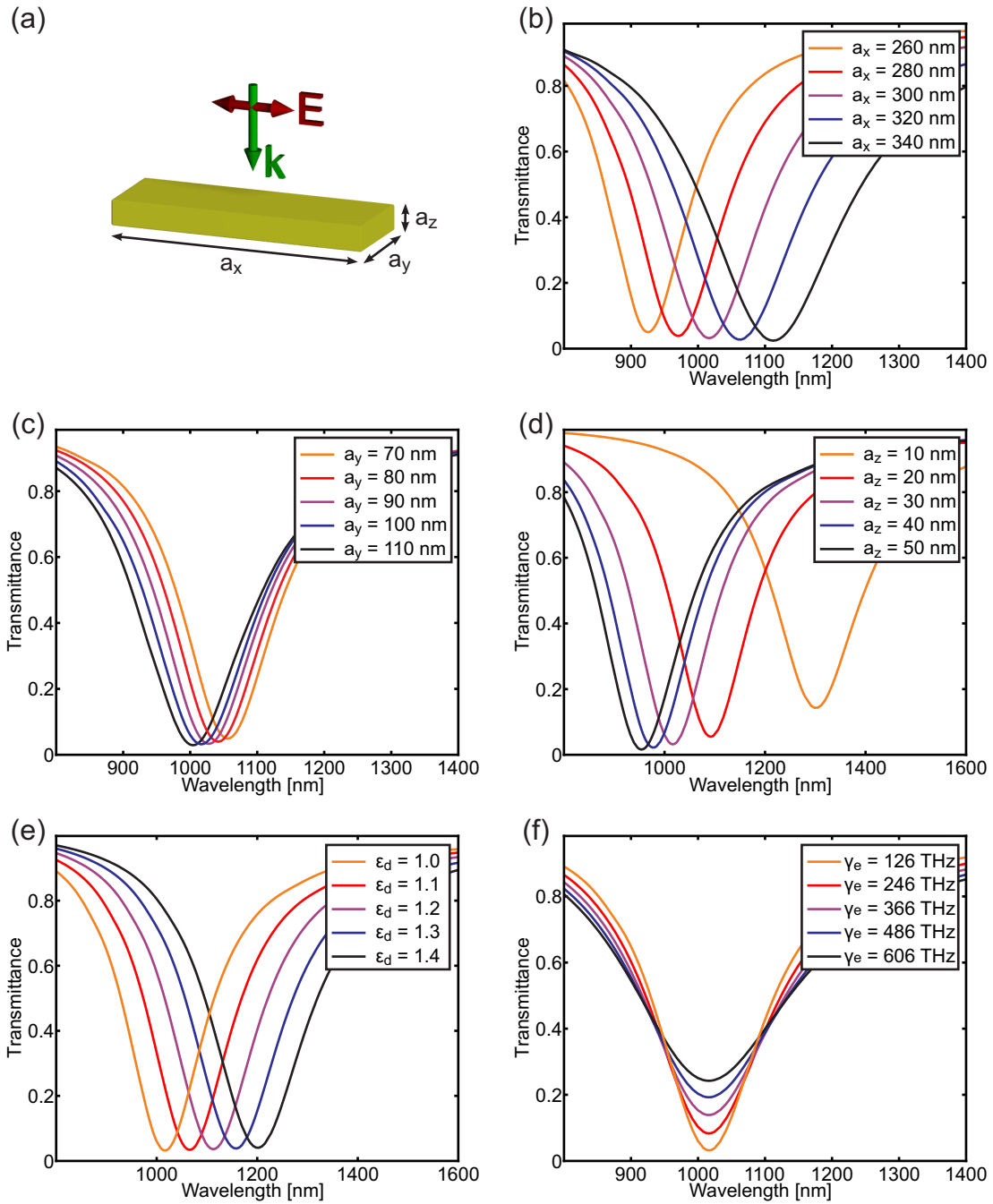


Figure 12: (a) A metal nanorod and its transmittance spectra showing the localized plasmon resonances for (b) different lengths a_x , (c) widths a_y , (d) thicknesses a_z , (e) permittivities of the environment ϵ_d as well as (f) different metal damping frequencies γ_e .

The basic structure for the following consideration is a gold nanorod [Fig. 12(a)] with a length of $a_x = 300$ nm, a width of $a_y = 100$ nm, and a thickness of $a_z = 30$ nm embedded in air ($\epsilon_d = 1$). The dielectric function of gold $\epsilon_m(\omega)$ is described using a Drude

model with the parameters defined in Sec. 2.2.2. The incident electromagnetic waves are polarized in x -direction (= along the nanorod). The localized plasmon resonance wavelength of such a nanorod is $\lambda_{\text{LP}} = 1015$ nm. The graphs in Fig. 12 show the effects on the resonance wavelength when changing the geometrical parameters a_x , a_y , a_z , the dielectric constant of the environment ϵ_d , and the Drude model damping frequency of the metal γ_e . An increase in the length a_x of the nanorod shifts the resonance to higher wavelengths [Fig. 12(b)]. For small variations we have a linear dependence of the plasmon resonance wavelength on the nanorod length with an offset due to the phase shift upon reflection of the plasmon at the nanorod end [22]. A larger width [Fig. 12(c)] as well as a larger thickness [Fig. 12(d)] shift the plasmon resonance to lower wavelengths. For thicknesses of $a_z = 30$ nm and below, the shifts are very pronounced. For higher thicknesses the resonance shifts become smaller, and the plasmon resonance approaches a limiting value. Since the electric fields outreach the nanostructure, the plasmon resonance is very dependent on the surrounding medium which is the basis for localized plasmon resonance sensing [Ch. 7]. The shifts of the plasmon resonance on changes of the permittivity ϵ_d of the environment are displayed in [Fig. 12(e)]. A higher refractive index of the environment $n_d = \sqrt{\epsilon_d}$ shifts the plasmon resonance to higher wavelengths. The resonance shift $\Delta\lambda$ depends linearly on the refractive index change Δn . Finally, the damping of the metal γ_e determines the linewidth of the resonances [Fig. 12(f)]. A higher damping causes transmittance curves with larger linewidths and lower modulation depth.

2.4.4 METAL NANOWIRES

In analogy to the previous section, localized plasmons can also be excited in continuous metal nanowires, when the incident light is polarized perpendicular to the wires [Fig. 13(a)]. The dependence of the plasmon resonance on the width a_x of gold nanowires with a thickness of $a_z = 20$ nm and a period of $p_x = 300$ nm is displayed in the graphs of Fig. 13(b). The resonance is located at lower wavelengths compared to the nanorods due to the infinite length a_y [compare with Fig. 12(c)].

2.4.5 DAMPING, LINEWIDTH, AND LIFETIME

Localized plasmons are damped by two mechanisms. Radiative decay into photons and non-radiative absorption due to electron-electron and electron-phonon scattering. The radiative damping is for the regarded particles about one order of magnitude higher than the non-radiative damping. Therefore, the linewidth of the plasmon resonances Γ is mainly determined by the radiative damping. It is directly coupled to the dephasing time T_d . The Fourier transformation of a damped oscillation like the dephasing of a plasmon

$$x(t) = x_0 e^{-i\omega_{\text{LP}} t} e^{-t/T_d} \quad (2.46)$$

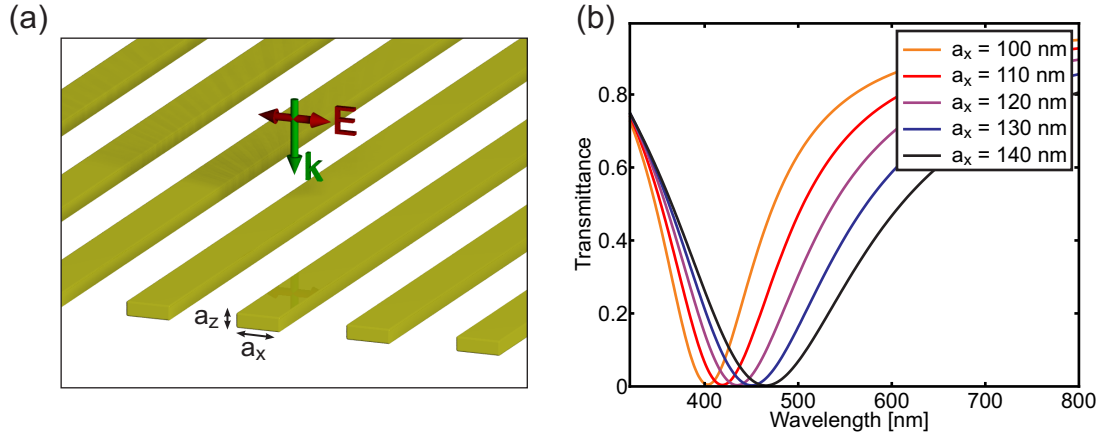


Figure 13: (a) A metal nanowire array and (b) its transmittance spectra showing the localized plasmon resonances for different widths a_x .

is a function with a Lorentzian lineshape. The maximum is at $\omega = \omega_{LP}$, half the maximum is reached at $\omega = \omega_{LP} \pm \frac{1}{T_d}$. With the full width at half maximum in energy units $\Gamma = \hbar\Delta\omega$, one obtains

$$\Gamma = \frac{2\hbar}{T_d}. \quad (2.47)$$

The dephasing time is usually in the order of a few femtoseconds. For a typical structure investigated in this thesis like the nanorods in Sec. 2.4.3, one observes in simulations a linewidth of around 200 nm for a resonance wavelength of 1000 nm. Converting this into energy units and applying Eq. 2.47 yields a plasmon lifetime of 5 fs. One has to keep in mind that in experiments on arrays of nanoparticles the contribution of inhomogeneous broadening impedes the deduction of plasmon lifetimes from resonance linewidths.

2.5 SIMULATION METHODS

To understand the mechanisms in plasmonic nanoparticles, simulations are a very helpful tool. Before the fabrication of a nanostructure, it is also crucial to know the approximate geometrical parameters for the desired effects that can be estimated with simulations. Two different simulation methods were used in this thesis: The finite difference time domain method implemented in a commercially available software package and a Fourier modal method implemented in Matlab. Both programs offer besides the calculation of transmittance, reflectance, absorbance and extinction spectra, the calculation of electric and magnetic field distributions.

2.5.1 FINITE DIFFERENCE TIME DOMAIN METHOD

The finite difference time domain (FDTD) algorithm is a method proposed in 1966 [126] to solve time-dependent differential equations and is today mostly used to solve Maxwell's equations. It relies on the discretization of space and time. The computational domain is divided into rectangular cells. A light source and, for every point in space, the permittivity and permeability have to be defined. In every cell of the size $\Delta x \cdot \Delta y \cdot \Delta z$ the electric and magnetic fields are calculated after time steps Δt . The components of the electric (magnetic) field in every cell are dependent on the electric (magnetic) fields of the previous time step as well as on the (numerical) curl of the local magnetic (electric) spatial field distributions according to the discretized Maxwell equations.

The software CST Microwave Studio² was used for the FDTD simulations. It provides a very intuitive user interface and easy structure modeling. When using periodic boundary conditions and a Gaussian pulse waveguide mode, a whole array of particles can be simulated for a wide spectral range in one quick simulation run. The program also provides animations of the propagation of the electromagnetic wave through the structure. Problems occurred for wavelengths smaller than the unit cell size (mainly convergence problems in the case of Rayleigh anomalies) as well as for spherical geometries.

Due to this advantages and disadvantages, CST was mainly used to generally understand the processes and interactions in a structure and to estimate structure parameters for fabrication.

2.5.2 FOURIER MODAL METHOD

The Fourier modal method (FMM) also known as rigorous coupled wave analysis (RCWA) is based on the general optical scattering matrix (S-matrix) theory [123, 117]. First, the structure is divided in several layers, then Maxwell's equations are solved in each layer independently. Finally, the layers are combined again using the S-matrix formalism which includes matching the electric and magnetic continuity conditions at the layer interfaces. Besides a calculation of spectra, the S-matrix also allows the calculation of the eigenmodes of a structure. This method has been proven to be very efficient on three-dimensional periodic plasmonic structures [121] because of intrinsically included periodicity due to the expansion in Fourier series. The used code includes several methods to improve the convergence such as Fourier factorization rules [55, 56] or the increase of the spatial resolution at metal-dielectric interfaces (adaptive spatial resolution [32, 18, 122]).

Calculations using FMM with a reasonable number of harmonics are quite time-consuming for three-dimensional metal-dielectric structures because it involves the expansion of discontinuous functions in a Fourier basis. However, the results are excellent and do not show instabilities for high frequencies or non-normal light incidence.

²CST (Computer Simulation Technology) AG, 64289 Darmstadt, Germany, www.cst.com

The FMM code was mainly used to calculate accurate resonances or spectra of well-understood structures.

3 EXPERIMENTAL TECHNIQUES

3.1 INTRODUCTION

This chapter provides a short overview of the experimental techniques that were used to produce the metallo-dielectric nanostructures of this thesis and to observe their optical properties. The deposition of thin metallic and dielectric layers [Sec. 3.2] is usually the first step followed by lithographic nanostructuring [Sec. 3.4] and etching processes [Sec. 3.3]. Three-dimensional samples can be produced this way in a layer-by-layer fashion. Scanning electron microscopy (Hitachi³ S-4800) and atomic force microscopy (Veeco⁴ CP-II) are used to determine the geometrical parameters of the nanostructures. The optical characterization of the samples is carried out using Fourier transform infrared spectroscopy [Sec. 3.5]. For all fabricated samples, glass substrates with an enhanced near-infrared transmission were used (Infrasil302 by Heraeus⁵).

3.2 THIN LAYER DEPOSITION

A number of different methods exist to produce thin films such as spin coating, sputtering, thermal evaporation, electron beam evaporation, galvanic deposition methods, or chemical vapor deposition including atomic layer deposition. The desired materials as well as the requirements in homogeneity, planarity, size, and thickness determine the choice of the method.

Dielectric layers with variable thicknesses ranging from 30 nm to several hundred nanometers were produced using spin coating. The rotation speed and rotation time of the substrate as well as the mixing ratio of the dielectric in a solvent and the parameters of the final baking process determine the thickness and the optical properties of the layer. Mainly, a polysiloxane-based spin-on glass (Intermediate Coating IC1-200 from Futurrex⁶) was used as a spacer for the microcavity samples of Chs. 5 and 6. A rotation speed of 3000 rotations per minute and a rotation time of 40 s results in a layer with a thickness of 350 nm. One has to keep in mind that this thickness is not constant over the

³Hitachi High-Technologies Europe GmbH, 47807 Krefeld, Germany, www.hht-eu.com

⁴Veeco Instruments Inc., Plainview, NY 11803, USA, www.veeco.com

⁵Heraeus Quarzglas GmbH, 63450 Hanau, Germany, www.heraeus-quarzglas.com

⁶Futurrex Inc., Franklin, NJ 07416, USA, www.futurrex.com

whole sample surface but increases slightly when moving away from the sample center. The measured deviations were in the range of a few tens of nanometers. By diluting the spin-on glass in n-butanol, the thickness of the layer can be further decreased down to 30 nm. The temperature of the final baking influences the refractive index of the layer. A baking time of 60 s at 200 °C on a hotplate results in a refractive index of $n_{\text{IC1}} = 1.40$. Spin coating is also used to deposit electron beam resists on the sample.

Metallic layers were deposited using electron beam evaporation (Pfeiffer⁷ Vacuum Electron Gun Evaporation System PLS 500). In a vacuum chamber with a pressure in the order of 10^{-6} mbar, the metals are heated and vaporized by an electron beam and deposit homogeneously on the walls of the reaction chamber as well as on the substrate placed inside [Fig. 14]. The evaporation rate and final thickness of the layer can be controlled very accurately by tuning the electron beam current. The best results for gold and chromium were obtained with an evaporation rate of 1 Å to 2 Å per second obtained with an electron beam current of 10 mA (Cr) and 250 mA (Au) at a voltage of 11.25 kV. Also, certain dielectric layers (MgF_2 , SiO_2) can be produced this way. The thickness, however,

⁷Pfeiffer Vacuum GmbH, 35614 Asslar, Germany, www.pfeiffer-vacuum.com

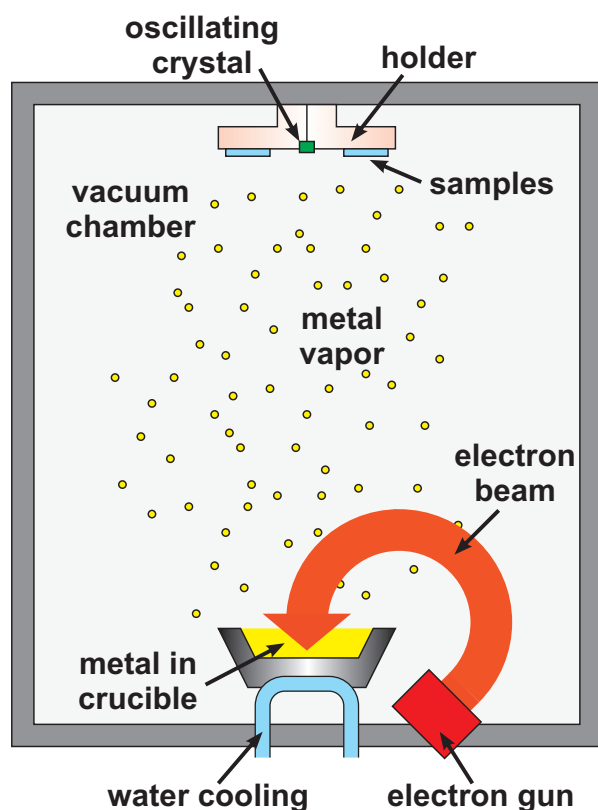


Figure 14: Evaporation of metals in a vacuum chamber using an electron beam. The electron beam is deflected by a magnetic field. The evaporation rate is measured with an oscillating crystal.

for MgF_2 layers is limited to about 40 nm before thermal stress causes cracks and other inhomogeneities in the layer. A constant evaporation rate is also crucial for the quality of the sample which could not be satisfactorily achieved with SiO_2 .

The measurement of the layer thickness with the oscillating crystal during the evaporation is very accurate for metals. However, for dielectric materials, the mass density of the evaporated layers is very dependent on the evaporation rate as well as on impurities and grain which can lead to imprecise values for the final layer thickness.

3.3 ETCHING

As essential as the deposition of materials for nanostructuring processes is their removal. Etching is used for subtractive structure generation processes as well as for the removal of resists. Depending on whether the material removed enters the liquid or gas phase, one distinguishes between wet and dry etching. The relevant techniques used for the structure generation in this thesis are ion beam etching and plasma etching.

An ion beam system (R.I.B.-Etch 160 by Technics Plasma GmbH) was used for the removal of metal layers located under a patterned negative resist layer [see Sec. 3.4]. By a voltage of 75 V, electrons are accelerated from a cathode filament and ionize argon atoms [Fig. 15]. The argon gas pressure is in the order of 10^{-4} mbar. The ions of the argon plasma are accelerated by an accelerating grid and hit the sample surface with a kinetic energy that is much higher than the binding energy of the metal layer atoms. The local transfer of impulse knocks out atoms or clusters of atoms of the sample surface and

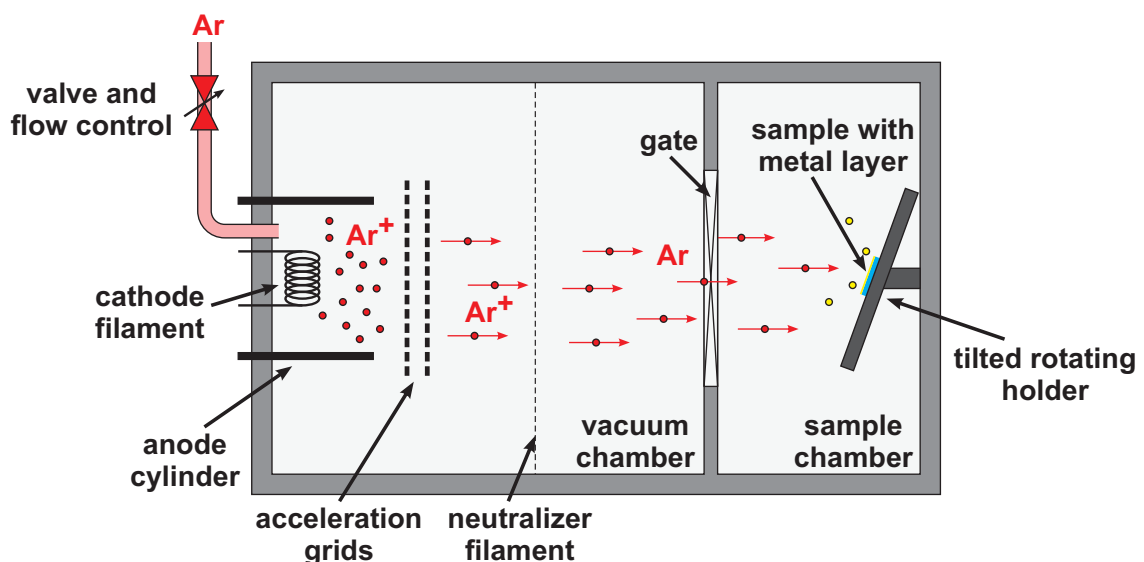


Figure 15: Principle of ion beam etching. Accelerated electrons produce an argon plasma. The positive argon ions are accelerated toward the sample and remove atoms from the sample surface.

transfers them into the gas phase before they are transported by convection. To reduce the space charge density and to prevent the target and surrounding surfaces from becoming charged, the argon ions are neutralized on their way to the sample by a neutralizer filament. To avoid redeposition of metal atoms and to achieve a spatially homogeneous etching rate, the sample stage constantly rotates and is tilted by an angle of 20° with respect to the argon beam. The etching rate for gold layers is in the order of 50 nm per minute for the used beam voltage (500 V) and beam current (100 mA).

To remove remaining particles of resist or other contaminants on a developed sample or substrate, oxygen plasma etching was applied. In a plasma chamber (Plasma Processor 100-E by Technics Plasma GmbH) oxygen at a pressure of around 1 mbar is ionized by microwaves generated by high frequency voltages (2450 MHz, 250 W). The oxygen plasma consists of highly reactive oxygen radicals and emits ultraviolet photons. This mixture removes small particles and cleans the sample surface very effectively by reactions with organic contaminants and by breaking organic bonds.

3.4 NANOSTRUCTURING

The advances of optical and electron beam lithography have pushed the limits of producible structure sizes to the order of a few tens of nanometers. Because of the diffraction limit in optical lithography, electron beam lithography is superior in terms of the minimum structure size. The disadvantage is the relatively long writing time which is for scientific applications, however, not a crucial factor. Electron beam lithography is the method used for the nanostructuring of the samples in this thesis. An electron beam (acceleration voltage 20 kV to 50 kV, beam current typically around 100 pA) is focussed by electrostatic

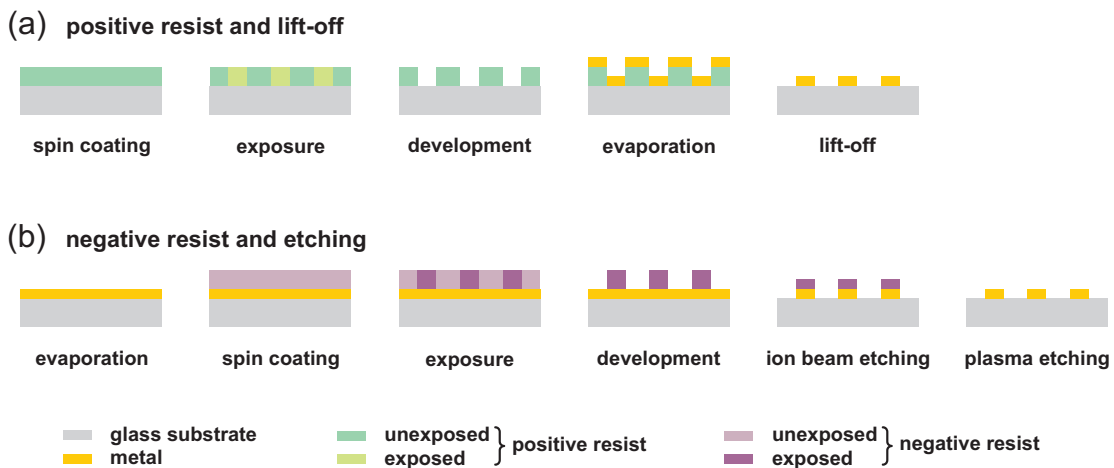


Figure 16: Layer scheme of electron beam lithography using positive and negative resist.

and electromagnetic lenses on the resist on the sample and scans the surface in a patterned fashion using electrostatic deflection lenses. The maximum field size is in the range of $100\ \mu\text{m} \times 100\ \mu\text{m}$. To obtain larger fields, many basic fields have to be attached which possibly implicates stitching problems. The kinetic energy of the electrons exceeds the atomic binding energies many times leading to a cascade of reactions when hitting the target material. This way, the properties of a resist change where it is exposed to the electron beam. A low beam current leads to low interelectron repulsions and, therefore, to a better focussing but also to longer writing times. The resolution of electron beam lithography is usually not limited by the electron beam diameter but rather by proximity effects. The energetic electrons are scattered many times and produce secondary electrons as well as X-ray radiation in the resist. Thus, neighboring parts of the resist are also partly exposed leading to a gradient of resist solubility. The electron beam lithography systems used for structures in this thesis (JEOL⁸ JBX-5DII and Raith⁹ e-LiNE) provide proximity correction routines to reduce these errors.

One can distinguish between additive and subtractive fabrication procedures using either negative or positive resist [Fig. 16]. The negative resist is spun on an evaporated metal layer. Those parts of a negative resist that were exposed to the electron beam become insoluble for the developer and remain on the metal layer after the development. Using reactive ion-beam etching [Sec. 3.3], the uncovered metal regions can be removed, and only those parts of the metal that were covered by the resist remain and form the nanostructures. The remaining resist can be removed using oxygen plasma etching [Sec. 3.3].

For most of the structures in this thesis, an additive procedure was applied. The positive resist polymethyl-methacrylate (PMMA) in a chlorobenzene solution is spun on a bare substrate. Exposure to an electron beam creates chain scission (or de-cross-linking) within the PMMA allowing for the selective removal of exposed areas by the chemical developer methyl-isobutyl-ketone (MIBK). After development, the resist is removed at those places where the later metal nanostructure was intended to reside. A short application of oxygen plasma removes small detached resist particles. Subsequently, a metal layer is evaporated on the structured resist. Next is the lift-off process where the sample is placed into N-Methyl-2-pyrrolidone (NMP) and acetone for about 2 hours. NMP makes the resist swell, and acetone finally removes it from the sample including the metal layer on the resist [Fig. 17]. Ideally, after this last step, only the metal that was deposited in the holes of the resist remains on the substrate surface.

The best results were obtained using two layers of different resists. The upper resist layer has a concentration of 1.5% in chlorobenzene and a molecular weight of 950 kg/mol whereas the lower layer consists of a resist with a concentration of 3.5% and a molecular weight of only 200 kg/mol making it more sensitive to the electron beam. The development of this two-layer combination creates a pattern in the resist with a larger excavation

⁸JEOL Ltd., Tokyo 196-8558, Japan, www.jeol.com

⁹Raith GmbH, 44263 Dortmund, Germany, www.raith.com

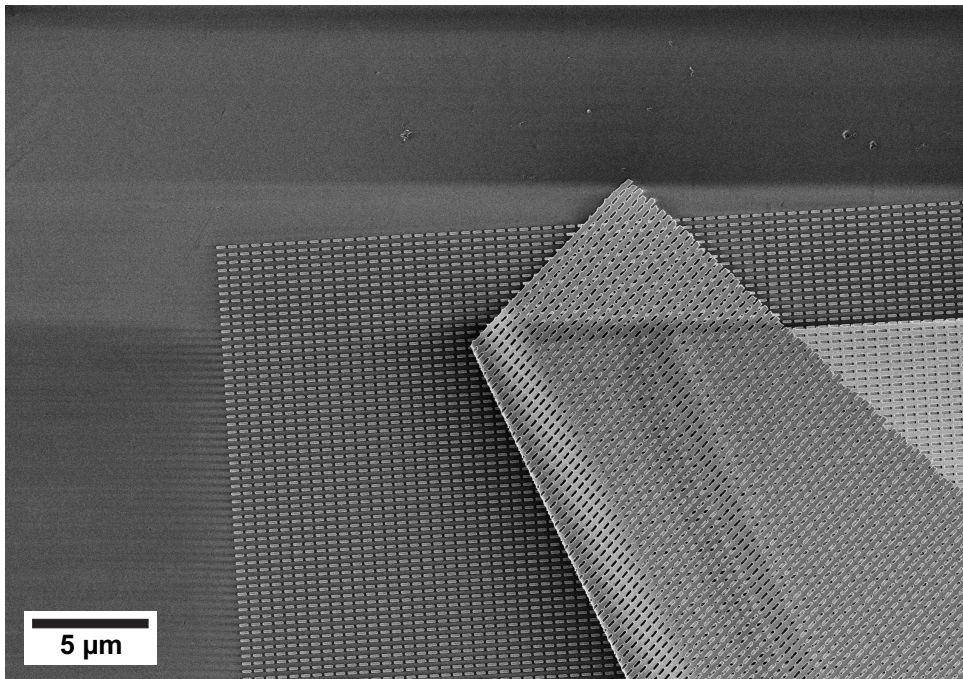


Figure 17: SEM image of an incomplete lift-off. The gold layer on top of the positive resist (nanohole array) was not totally removed from the structure (array of nanorods).

in the lower resist layer facilitating the lift-off and leading to a better quality than the downward tapered gaps in a developed single-layer resist. Additionally, the evaporation of a thin chromium layer (3 nm) or alternatively the spin-coating of a conducting spacer (Espacer 300 Z from Showa Denko¹⁰) on the resist avoids charging of the sample during exposure.

Three-dimensional multilayer structures can be fabricated using thick (200 nm) cross-shaped alignment marks on the sample. These marks can be detected by the electron beam, and each new layer is aligned to the same positions on the sample. This way, up to five layers can be accurately stacked [61, 59, 64].

To evaluate and measure the geometrical parameters of multilayer structures, it is necessary to look at them from the side with a scanning electron microscope. To provide such a view, a hole with defined edges has to be cut in the sample which has been accomplished using a focussed ion beam (FIB). In general, a FIB can be used to produce nanostructures with even better resolutions and higher aspect ratios than those obtained by electron beam lithography. The disadvantage is the very long writing time.

¹⁰Showa Denko Europe GmbH, 81829 München, Germany, www.showa-denko.com

3.5 SPECTROSCOPY

The observation of plasmonic and photonic resonances in the fabricated nanostructures was carried out using Fourier transform infrared (FTIR) spectroscopy. In contrast to dispersive spectrometers, the spectrum is not recorded by changing the wavelengths. Instead, the fundamental component of an FTIR spectrometer is a Michelson interferometer consisting of a beam splitter and two mirrors (one fixed, one movable). The light entering the interferometer is split into two parts by the beam splitter, one part being reflected by the fixed mirror, the other part by the movable mirror. The measured quantity is an interferogram $I(x)$, i.e. the intensity I of the recombined beams as a function of the moving mirror displacement x . For a single frequency ν , the interferogram is given by

$$I(x) = \cos(2\pi\nu x). \quad (3.1)$$

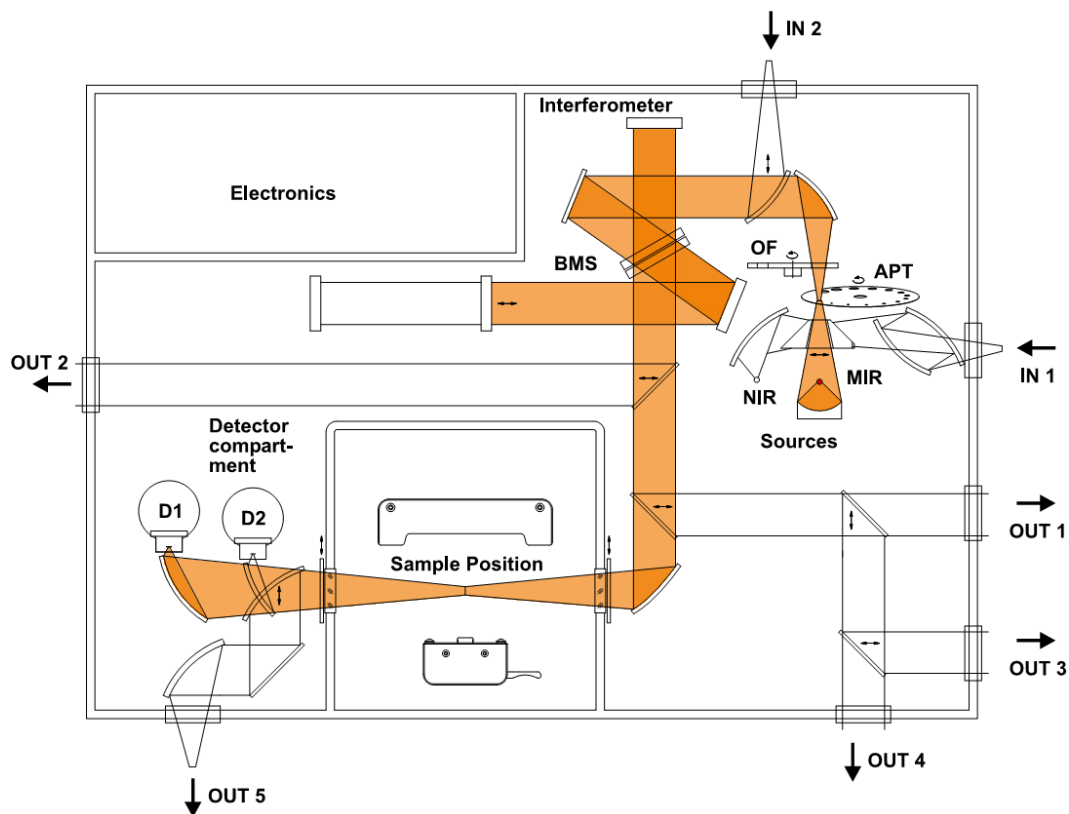


Figure 18: Beam paths in the FTIR spectrometer. The light leaving the near-infrared (NIR) or mid-infrared (MIR) light source passes an aperture wheel (APT) and an optional optical filter (OF) before it arrives at the beam splitter (BMS) in the interferometer. The infrared microscope used for the measurements of nanostructures is attached to output 1 (OUT1). (Image source: Bruker Optik GmbH)

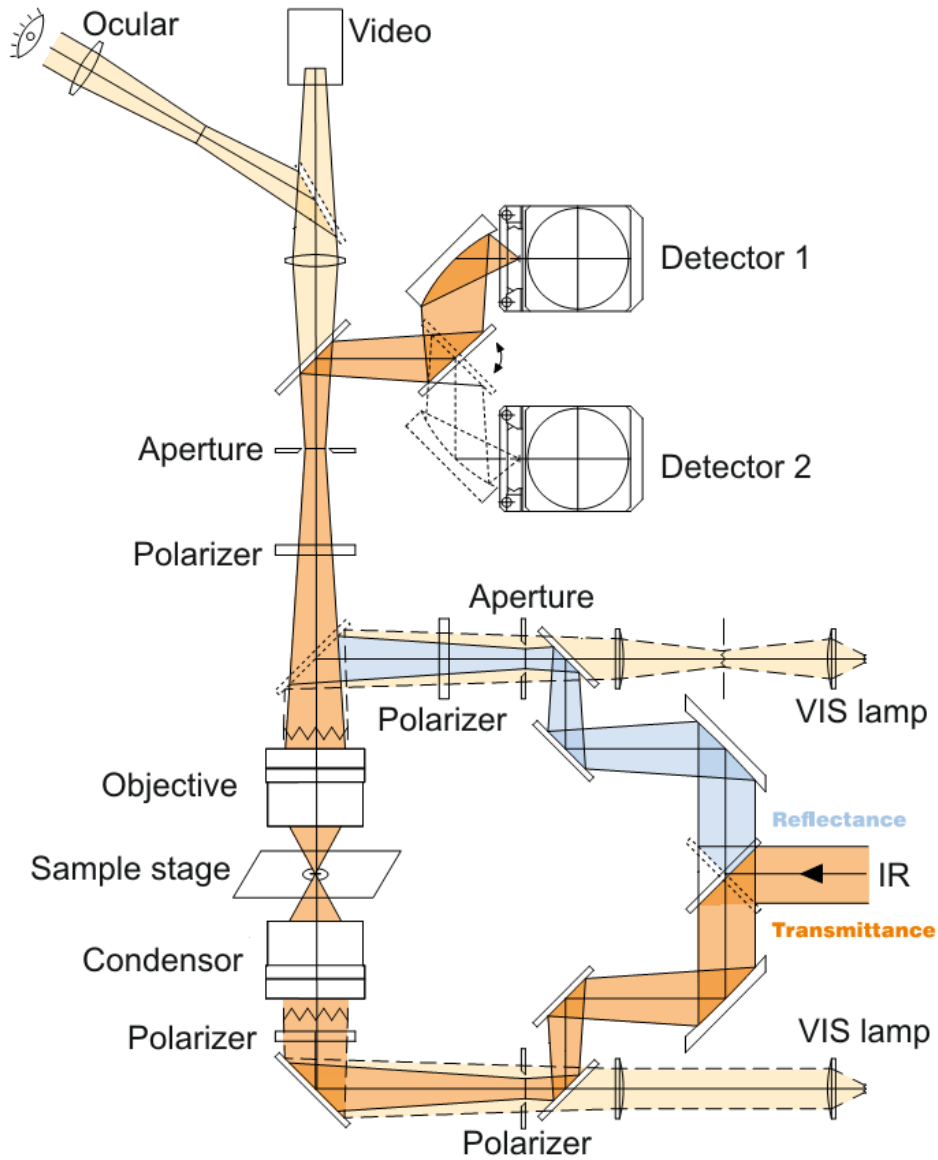


Figure 19: Beam paths in the attached infrared microscope. The sample can be measured either in reflection or transmission. (Image source: Bruker Optik GmbH)

For a spectral distribution $S(\nu)$, the interferogram becomes

$$I(x) = \int_{-\infty}^{+\infty} S(\nu) \cos(2\pi\nu x) d\nu. \quad (3.2)$$

The interferogram $I(x)$ and the spectrum $S(\nu)$ are pairs of a Fourier transformation, hence, the spectrum is given by the Fourier transform of the interferogram

$$S(\nu) = \int_{-\infty}^{+\infty} I(x) \cos(2\pi\nu x) dx. \quad (3.3)$$

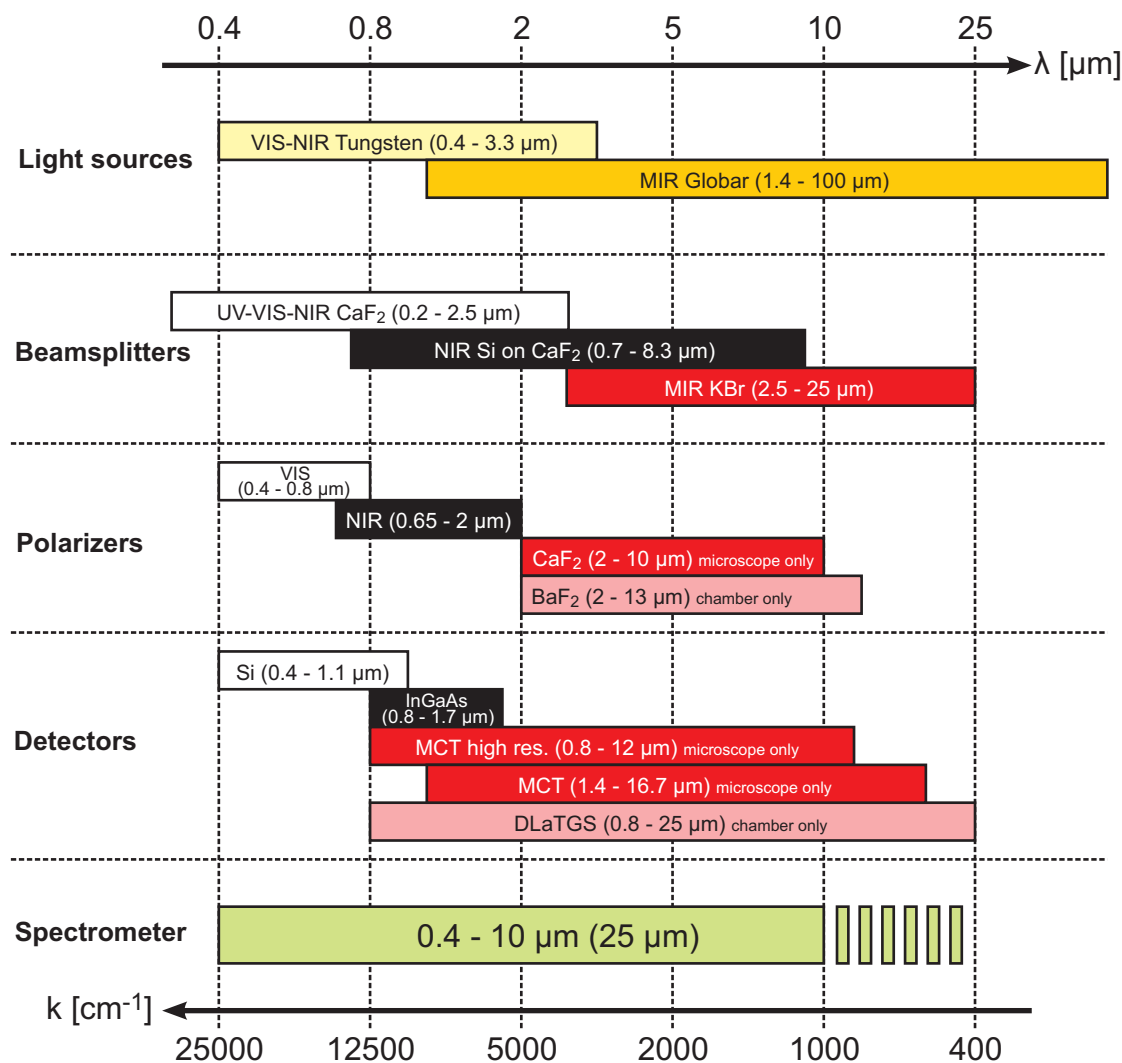


Figure 20: Spectral coverage of the light sources, beam splitters, polarizers and detectors used in the FTIR spectrometer. The total operational range starts at 400 nm and ends at 10 μm for polarization dependent measurements using the attached infrared microscope.

For our measurements, we used an FTIR spectrometer from Bruker¹¹ (Vertex 80) [Fig. 18] with an attached infrared microscope (Hyperion 2000) [Fig. 19]. Two light sources, a globar (an electrically heated silicon carbide rod) and a tungsten halogen lamp, are available covering the visible, near- and mid-infrared spectrum [Fig. 20]. For a first adjustment of intensity, an aperture wheel is installed directly in front of the light sources.

The light enters the Michelson interferometer and is split in two parts by the beam splitter. Three different beam splitters (KBr, Si on CaF₂, and CaF₂) are in use to cover the full spectrum [Fig. 20]. The resolution of the spectrum is determined by the total distance the mirror can be moved and by the accuracy of the mirror position determination.

¹¹Bruker Optik GmbH, 76275 Ettlingen, Germany, www.brukeroptics.com

The spectral resolution of the used system is 0.07 cm^{-1} . The two phase-shifted recombined beams leave the interferometer and are sent to the sample compartment where they are focussed on the sample and finally on the detector, a DLaTGS (deuterated L-alanine doped triglycene sulphate) pyroelectric detector covering the near- and mid-infrared spectrum. Measurements in the sample compartment, however, do not allow for a controlled illumination of areas of only a few tens or hundreds of micrometers which is the typical field-size of our nanostructure samples. Therefore, the light can be alternatively directed to an attached infrared microscope. It uses Cassegrain objectives with a $15\times$ magnification and a numerical aperture of 0.4 to focus the light on the sample which is located on an x-y-micrometer stage. The incident angle on the sample ranges from 9.8° to 23.6° . By placing the sample on a wedge with an opening angle of 16.7° , the incident angle range can be reduced to $\pm 6.9^\circ$ from normal incidence associated with a loss of half the intensity.

The microscope can operate either in transmission or in reflection mode. With a flexible knife-edge aperture the illuminated area on the sample can be decreased to only a few hundred square micrometers. Different linear polarizers as well as quarter-wave plates can be installed before and after the sample to allow for linear and circular polarization dependent measurements. Finally, four semiconductor detectors can be used in combination with the microscope: a silicon diode for the visible spectrum, an indium gallium arsenide (InGaAs) diode for the near-infrared, and two liquid nitrogen cooled mercury cadmium telluride (MCT) detectors with different sensitivities covering the near- and mid-infrared frequencies [Fig. 20].

Measuring small fields often caused problems concerning the intensity of the light reaching the detector. By polarizers and apertures, the intensity is decreased a lot. A series of more than 100 spectra was often recorded to obtain an acceptable signal-to-noise ratio.

4 PLASMON COUPLING

4.1 INTRODUCTION

After having reviewed the optical properties of isolated metallic nanoparticles in Sec. 2.4, the focus will now be on the interactions among two or more coupled particles. The coupling of nanoparticles opens up new ways in guiding plasmons, exciting plasmons and changing the properties of nanostructured materials. Two fundamentally different coupling mechanisms have to be distinguished: coupling via the near-field and coupling via the far-field.

Plasmonic nanoparticles can be coupled via their near-fields when the particle distance is substantially lower than the plasmon resonance wavelength of the nanostructure. Many near-field coupled structures have been investigated in the past years [Fig. 21] including nanorod pairs (also referred to as cut-wire pairs) [95, 21], nanowire pairs [14, 15], double-fishnet structures [20, 59], coupled split-ring resonators [61, 62], particle chains [71], or

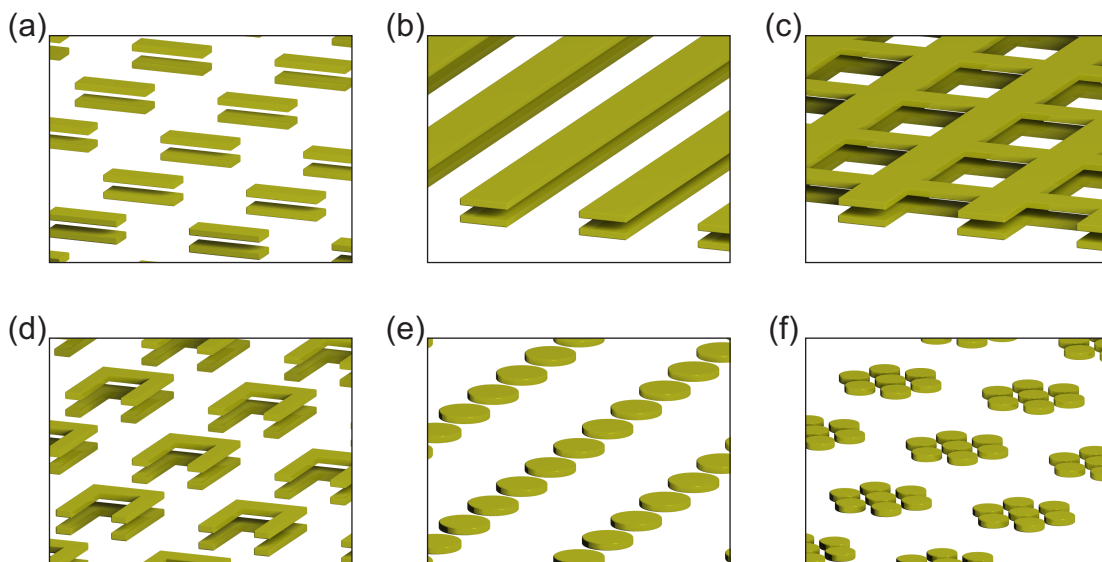


Figure 21: Examples of near-field coupled plasmonic nanostructures: (a) nanorod pairs, (b) nanowire pairs, (c) double-fishnet structures, (d) coupled split-ring resonators, (e) particle chains, and (f) oligomers

oligomers [37]. All near-field coupled plasmonic structures have in common that the fundamental localized plasmon resonance is shifted or split (hybridized) due to the particle interactions. Often, circular currents or currents with opposite directions exhibit magnetic moments providing a whole new way of interaction and excitation possibilities. In general, the coupling strength decreases when the particle-particle distance increases. When the particle distance, however, approaches or exceeds the wavelength of the plasmon resonances, plasmonic far-field interactions mediated by photonic Fabry-Pérot modes can be observed. This effect can be investigated by analyzing multilayer Bragg stacks of plasmonic structures or plasmonic particles in microcavities. In the context of optical plasmonic nanoantennas [1], far-field coupling has been investigated as well.

This chapter includes an analysis of near-field coupled nanorod pairs and nanowire pairs (simulation and experiment) for their later use in coupled photonic-plasmonic systems. The transition from the near-field to the far-field coupling regime is examined and models to describe the far-field interactions are derived in order to understand the combined photonic-plasmonic systems that will be investigated in the context of strong coupling [Chs. 5 and 6] and sensing applications [Ch. 7].

4.2 NEAR-FIELD COUPLING

4.2.1 DIPOLE MODEL

If the particle size is sufficiently smaller than the particle distance d , the particles can be treated as point dipoles and the plasmonic near-field coupling can be approximated as dipole-dipole coupling [129]. Hence, the distance dependence of the coupling strength is on the order of d^{-3} which has been experimentally demonstrated for example for the case of particle chains [71, 70]. If the resonance wavelengths are large enough, the same quasi-electrostatic model as for the excitation of localized plasmons in single particles

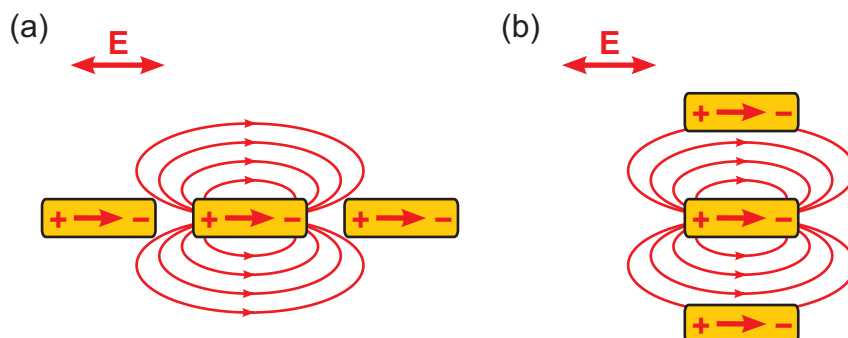


Figure 22: Dipolar electric fields of near-field coupled nanoparticles arranged (a) along and (b) perpendicular to the electric field direction of the incident wave.

can be applied [see Sec. 2.4.1] and retardation effects can be neglected. Two different arrangements of particles can be distinguished [Fig. 22]: the particles can be arranged along the direction of the electric field of the incident wave or perpendicular to it. In the first case [Fig. 22(a)], the restoring force acting on the electrons in the particles is decreased by the dipolar electric field of neighboring particles resulting in a shift of the localized plasmon resonance to lower frequencies. In the second case [Fig. 22(b)], the restoring force is increased leading to a plasmon resonance shift towards higher frequencies. The emitted radiation of the dipoles is mostly directed perpendicular to the oscillation direction. Therefore, in structures aligned perpendicular to the incident electric field, like stacked nanowires, the coupling is much larger than in a planar arrangement along the electric field.

For structure sizes approaching the particle distance, like in the case of near-field coupled nanorods, the point dipole model does not produce accurate results anymore. The model can be expanded to a series of dipoles representing the currents in a nanostructure of a certain shape. With an appropriate oscillator strength distribution function of the dipoles, a good agreement with experimental measurements can be achieved [52]. Despite its deficiencies, the dipole model provides a simple picture to intuitively understand the coupling mechanisms of nanostructures.

4.2.2 PLASMON HYBRIDIZATION

The second phenomena that can be observed at coupled nanoparticles besides a mere shift of the plasmon resonances is the resonance splitting. In analogy to the hybridization of atomic energy levels which occurs when the atoms couple and form molecules, localized plasmon resonances can be hybridized [97, 83]. A system of two coupled nanorods, for example, exhibits two different resonances: a symmetric mode where both plasmons oscillate in phase and an antisymmetric mode where the two plasmons oscillate with a

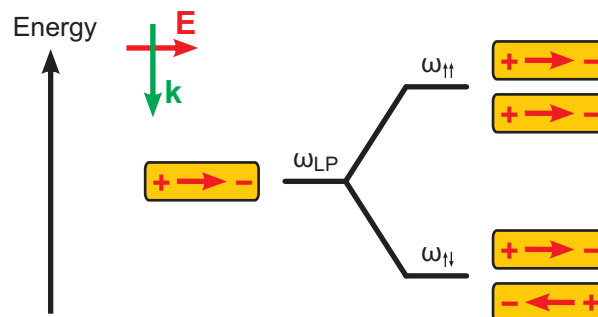


Figure 23: Energy diagram of hybridized localized plasmon resonances in a pair of nanorods.

phase shift of 180° . The symmetric mode $\omega_{\uparrow\uparrow}$ is located at higher frequencies, the anti-symmetric mode $\omega_{\uparrow\downarrow}$ at lower frequencies [Fig. 23]. The closer the nanorods approach each other, the larger is the resonance splitting [Fig. 24(c)]. In principle, the antisymmetric (quadrupolar) mode is an optically dark mode, that can not be excited by an external electromagnetic wave due to the vanishing total electric dipole moment. In order to excite it anyway, a structural asymmetry is necessary which is given either by slightly different lengths or by different materials (glass, air) that partially surround the nanorods of a pair. In stacked structures, the spatial variation of the electric field in propagation direction (retardation) enables the excitation of antisymmetric modes. Additionally, the antisymmetric mode exhibits a magnetic moment due to the opposite electric current direction in each pair which constitutes a partial circular current. For this reason, the symmetric and antisymmetric plasmon modes are also often referred to as electric and magnetic plasmon modes since they induce an electric and magnetic dipole, respectively. The interaction with the magnetic field of the electromagnetic wave can lead to many interesting effects. For this reason nanorod pairs have been considered as building blocks for materials with a negative index of refraction [21]. If the magnetic field of the wave is able to directly excite the antisymmetric plasmon modes has been extensively discussed. A localized plasmon excitation by the magnetic field of an incident electromagnetic wave has been claimed in a number of publications [94, 26]. However, magnetic fields cannot even do work, and by regarding different spatial arrangements of nanorod pairs, it can be proven [75, 118] that only the electric fields of an incident electromagnetic wave excite symmetric as well as antisymmetric localized plasmon modes.

4.2.3 NANOROD PAIRS

In nanorod pairs, the localized plasmon resonance is hybridized. In Fig. 25, the electric current density in a nanorod pair as well as the magnetic field distribution (H_y -component) around the structure was calculated for the symmetric ($\omega_{\uparrow\uparrow}$) and the antisymmetric ($\omega_{\uparrow\downarrow}$) localized plasmon resonance using FDTD simulations. The opposite currents of the antisymmetric mode induce a strong magnetic field between the two nanorods. In the case of the symmetric mode, a weak circular magnetic field around the unidirectional electric current of the nanorod pair can be observed.

The magnitude of the splitting is determined by the coupling strength which can be varied by changing the particle distance. A series of samples of stacked gold nanorod pairs with different vertical distances d ranging from 30 nm to 100 nm was fabricated and compared to FDTD simulations [Fig. 24]. The samples were produced on an Infrasil substrate ($n_{\text{sub}} = 1.45$) using electron beam lithography with a positive resist procedure [Sec. 3.4]. Magnesium fluoride ($n_{\text{MgF}_2} = 1.38$) was used as a spacer layer between the nanorods. MgF_2 layers with thicknesses larger than 70 nm showed a bad layer quality and could not be used for measurements. The length of the nanorods is 320 nm, the width 100 nm and

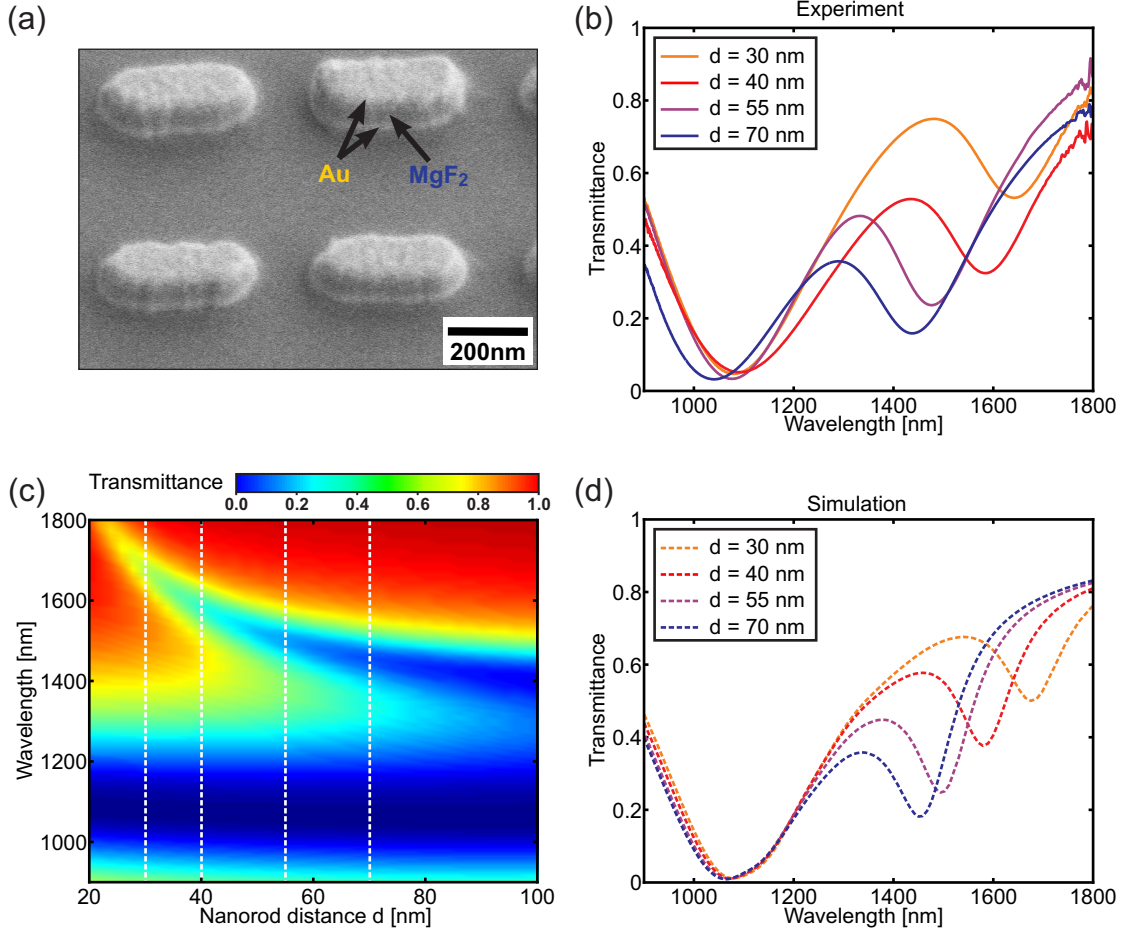


Figure 24: (a) Tilted SEM image of fabricated nanorod pairs. The different Au and MgF₂ layers are clearly visible. Comparison of measured (b) and simulated (d) transmittance spectra of nanorod pairs with different distances. (c) Simulated transmittance spectra for nanorod distances ranging continuously from 20 nm to 100 nm demonstrating the progression of the symmetric and the antisymmetric plasmon mode. The spectra in (c) correspond to vertical cross-sections of the color plot (d) indicated by dashed white lines.

d	resonance splitting (simulation)	resonance splitting (experiment)
30 nm	597 nm	563 nm
40 nm	507 nm	492 nm
55 nm	429 nm	400 nm
70 nm	390 nm	386 nm

Table 1: Comparison of simulated and measured resonance splittings of nanorod pairs.

the thickness 30 nm. The unit cell size is $500 \text{ nm} \times 500 \text{ nm}$. The curves demonstrate how the resonance splitting increases when the nanorods approach each other. The experimentally obtained spectra and splitting magnitudes [Tab. 1] agree very well with the simulation. The deviations can be explained with an imprecise measurement of the MgF_2 layer thickness during the evaporation [see Sec. 3.2].

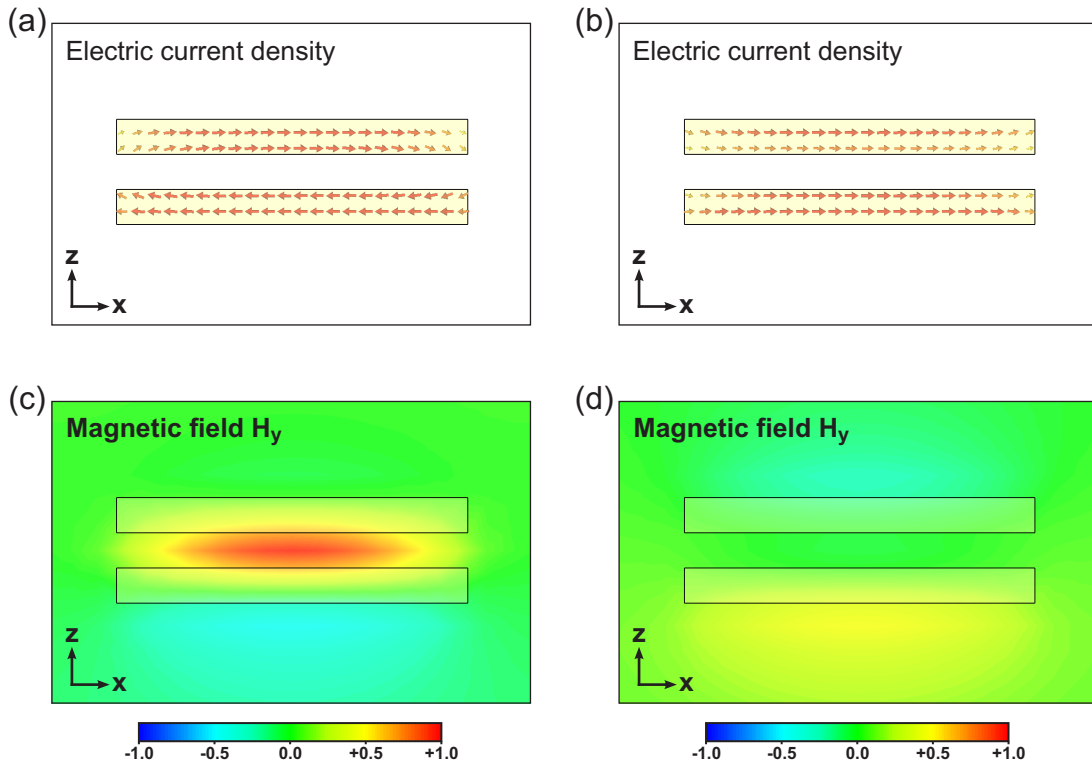


Figure 25: FDTD-Simulation of the electric current density (a,b) and the magnetic field distributions (H_y) (c,d) for the symmetric (a,c) and the antisymmetric (b,d) localized plasmon resonances of a gold nanorod pair.

4.2.4 MIRROR HYBRIDIZATION

The electrostatic concept of image charges can be used to explain the behavior of a plasmonic nanostructure located close to a mirror. The effects of the mirror on the electric field of a charged particle can be modeled by replacing the mirror with the same particle on the other side of the mirror with opposite charge (image charge) [Fig. 26(a)]. This model can be transferred to plasmonics [60] when a localized plasmon is excited for example in a nanorod that is placed close to a metal layer. Also in this situation, the metal layer can be imagined to be replaced with a second nanorod on the other side of the metal layer with an opposite charge distribution [Fig. 26(b)]. This corresponds to the

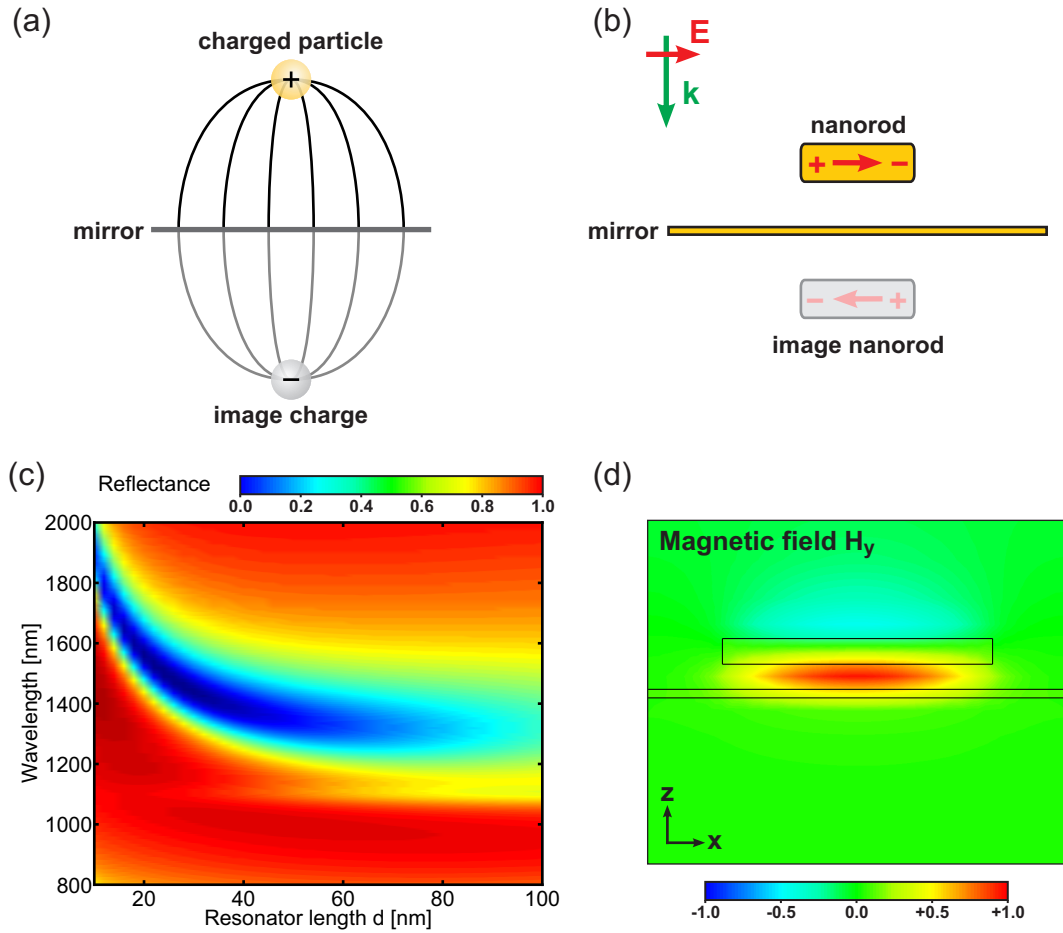


Figure 26: (a) The concept of image charges (b) transferred to plasmonic nanorods. (c) Simulated reflectance spectra for different distances d of the nanorod to the mirror. (d) Magnetic field distribution (H_y -component) at resonance.

situation of a nanorod pair where the antisymmetric plasmon mode is excited. Accordingly, a nanorod close to a metal layer exhibits a localized plasmon mode that is shifted to higher energies the more the nanorod approaches the mirror. Fig. 26(c) displays a series of reflectance spectra for different distances d . In analogy to the antisymmetric mode of a nanorod pair [Fig. 25(c)], a magnetic moment is induced between the nanorod and the mirror [Fig. 26(d)]. The simulated gold nanorods have the same geometrical parameters as in the previous section. The gold mirror has a thickness of 10 nm. The whole system is simulated in vacuum.

4.3 FAR-FIELD COUPLING

4.3.1 TRANSITION FROM NEAR- TO FAR-FIELD COUPLING

All discussed effects so far can be understood by applying the quasi-static approximation and exploring the electric fields. As soon as the particle distance increases and approaches the considered wavelengths, electrodynamic effects like retardation can no longer be neglected. The nanoparticles start to behave similar to Fabry-Pérot-cavities with resonating mirrors. Fig. 27 displays the characteristics of the resonances of a pair of nanorods when the vertical particle distance is increased from the near-field to the far-field coupling regime. In the near-field coupling regime below $d \approx 200$ nm, the hybridized localized plasmon modes converging to the resonance of a single layer for increasing d can be observed. When the distance d exceeds the near-field coupling regime, one observes, instead of a mere vanishing interaction, perturbed Fabry-Pérot-like cavity modes. The perturbation is strongest around the plasmon resonances indicating a coupling of the plasmons of each layer via the far-field. The vertical coupling of stacked structures has the advantage that the emitted dipole radiation is always directed towards the next dipole. In addition, the phase retardation in the dipole excitation allows the excitation of dark eigenmodes (like the antisymmetric plasmon mode of a nanorod pair) that can not be addressed in a lateral arrangement.

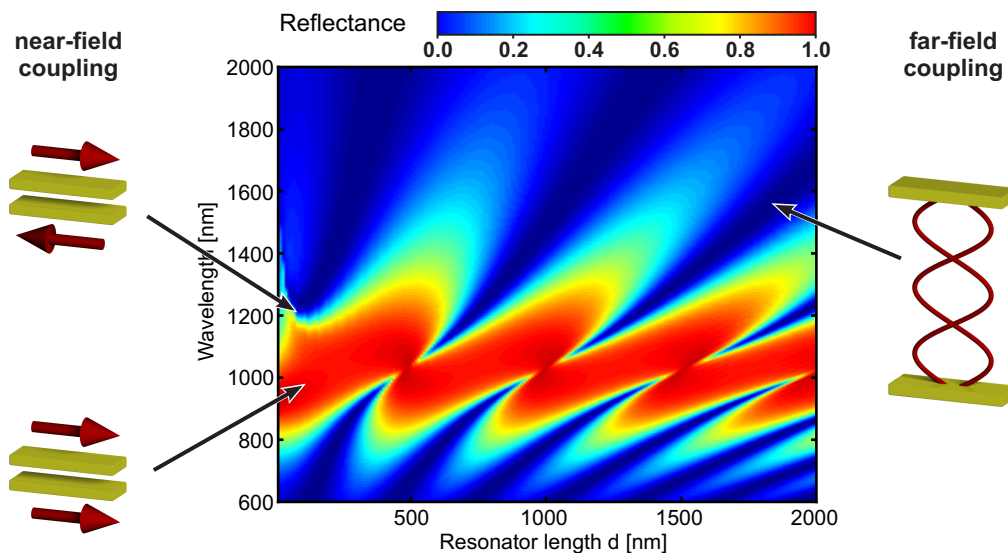


Figure 27: Reflectance spectra for a pair of nanorods with distances ranging from 10 nm to 2000 nm covering the near- and far-field coupling regimes.

4.3.2 PHASE SHIFT MODEL

The spectra of the far-field coupled nanorods can be explained by investigating the phase shifts that occur when an electromagnetic wave is propagating through the system. As pointed out in Sec. 2.3.1, the resonance condition for any resonator implies that the total phase shift $\Delta\varphi_{\text{tot}}$ that a wave accumulates during one round trip in the resonator has to be a multiple of 2π . In the case of a cavity (Eq. 2.21), this leads to a resonance wavelength of

$$\lambda_N = \frac{2n_{\text{cav}}d}{(N+1) - \frac{\Delta\varphi_{\text{refl}}}{\pi}} \quad (4.1)$$

with the mirror distance d and n_{cav} being the refractive index of the material in the cavity. N is an integer and $\Delta\varphi_{\text{refl}}$ is the phase shift upon reflection at a mirror which is π for a perfect metal, but it can be very different from that for real gold and thin metal layers [see Fig. 6]. If the mirrors of the cavity are replaced with resonating elements, like plasmonic nanostructures, the phase shift upon reflection $\Delta\varphi_{\text{refl}}$ has to be replaced with the wavelength-dependent phase shift upon plasmon excitation $\Delta\varphi_{\text{exc}}(\lambda)$ [Fig. 28]¹².

To approximate the plasmon excitation phase shift, a simple model of a driven harmonic oscillator can be assumed for the plasmon excitation. It is described by the differential equation

$$\ddot{\vec{r}} + \gamma_{\text{LP}}\dot{\vec{r}} + \omega_{\text{LP}}^2\vec{r} = -\frac{e}{m_e}\vec{E}_0e^{-i\omega t} \quad (4.2)$$

with the plasmon damping γ_{LP} and the localized plasmon resonance frequency ω_{LP} of the nanostructure. The field of the incident electromagnetic wave $\vec{E}(t) = \vec{E}_0e^{-i\omega t}$ acts as a driving force on the electrons in the metal and excites the plasmon. The solution of Eq. 4.2 leads to

$$\vec{r}(t) = \frac{1}{\omega^2 - \omega_{\text{LP}}^2 + i\gamma_{\text{LP}}\omega} \frac{e}{m_e}\vec{E}(t) \quad (4.3)$$

In analogy to the quasi-free electron model from Sec. 2.2.1, a permittivity for the plasmonic layer can now be derived. The plasmonic layer is in this context treated as a homo-

¹²Due to the dispersive nature of metals, also the phase shift upon reflection $\Delta\varphi_{\text{refl}}$ at metal mirrors is wavelength-dependent. However, compared to the phase shift upon plasmon excitation, this dependence is negligibly weak.

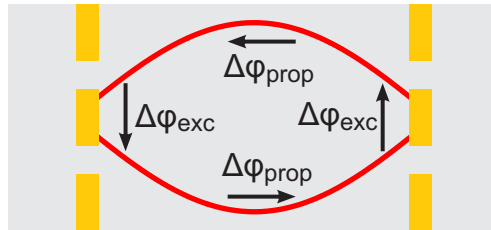


Figure 28: Phase shifts for cavities consisting of nanostructured mirrors.

geneous layer with a permittivity that has a Lorentzian response at the localized plasmon resonance ω_{LP} . This effective permittivity is then given by

$$\varepsilon_{\text{LP}}(\omega) = 1 - \frac{\omega_{\text{p}}^2}{\omega^2 - \omega_{\text{LP}}^2 + i\gamma_{\text{LP}}\omega} \quad (4.4)$$

with the plasma frequency ω_{p} as it is defined in Sec. 2.2.1. To take the influence of a dielectric material with a refractive index n_d in the plasmon layer into account, the non-resonant part of the effective dielectric function $n_{\text{LP}}(\omega)$ can be changed from 1 to n_d . Hence, the refractive index of the plasmon layer is given by

$$n_{\text{LP}}(\omega) = \sqrt{n_d - \frac{\omega_{\text{p}}^2}{\omega^2 - \omega_{\text{LP}}^2 + i\gamma_{\text{LP}}\omega}}. \quad (4.5)$$

Using the Fresnel equations, the reflectivity of such a plasmonic layer embedded between two dielectric layers with the refractive indices n_{cav} and n_{sub} [Fig. 29] can be calculated as

$$R = \frac{R_{12} + R_{23}e^{2ikd}}{1 + R_{12}R_{23}e^{2ikd}} \quad (4.6)$$

with

$$R_{12} = \frac{n_{\text{cav}} - n_{\text{LP}}}{n_{\text{cav}} + n_{\text{LP}}} \quad \text{and} \quad (4.7)$$

$$R_{23} = \frac{n_{\text{LP}} - n_{\text{sub}}}{n_{\text{LP}} + n_{\text{sub}}}. \quad (4.8)$$

The phase shift upon plasmon excitation is then given by

$$\Delta\varphi_{\text{exc}} = \arctan \frac{\text{Im}[R]}{\text{Re}[R]}. \quad (4.9)$$

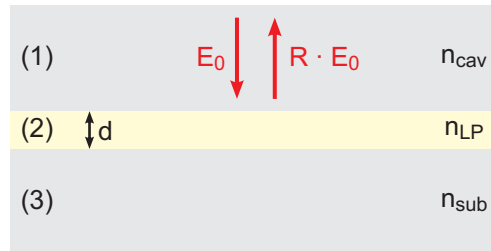


Figure 29: The plasmon layer (2) is treated as a homogeneous layer with an effective permittivity. It is surrounded by two different dielectric materials (1) and (3) representing a substrate and a cavity filling material.

4.3.3 NANOSTRUCTURED CAVITIES

The influence of plasmonic excitations on the resonances of cavities consisting of different nanostructured mirrors is investigated in the following. Cavities consisting of nanorods, nanorod pairs and continuous nanowires are compared to a cavity with plane metal layer mirrors.

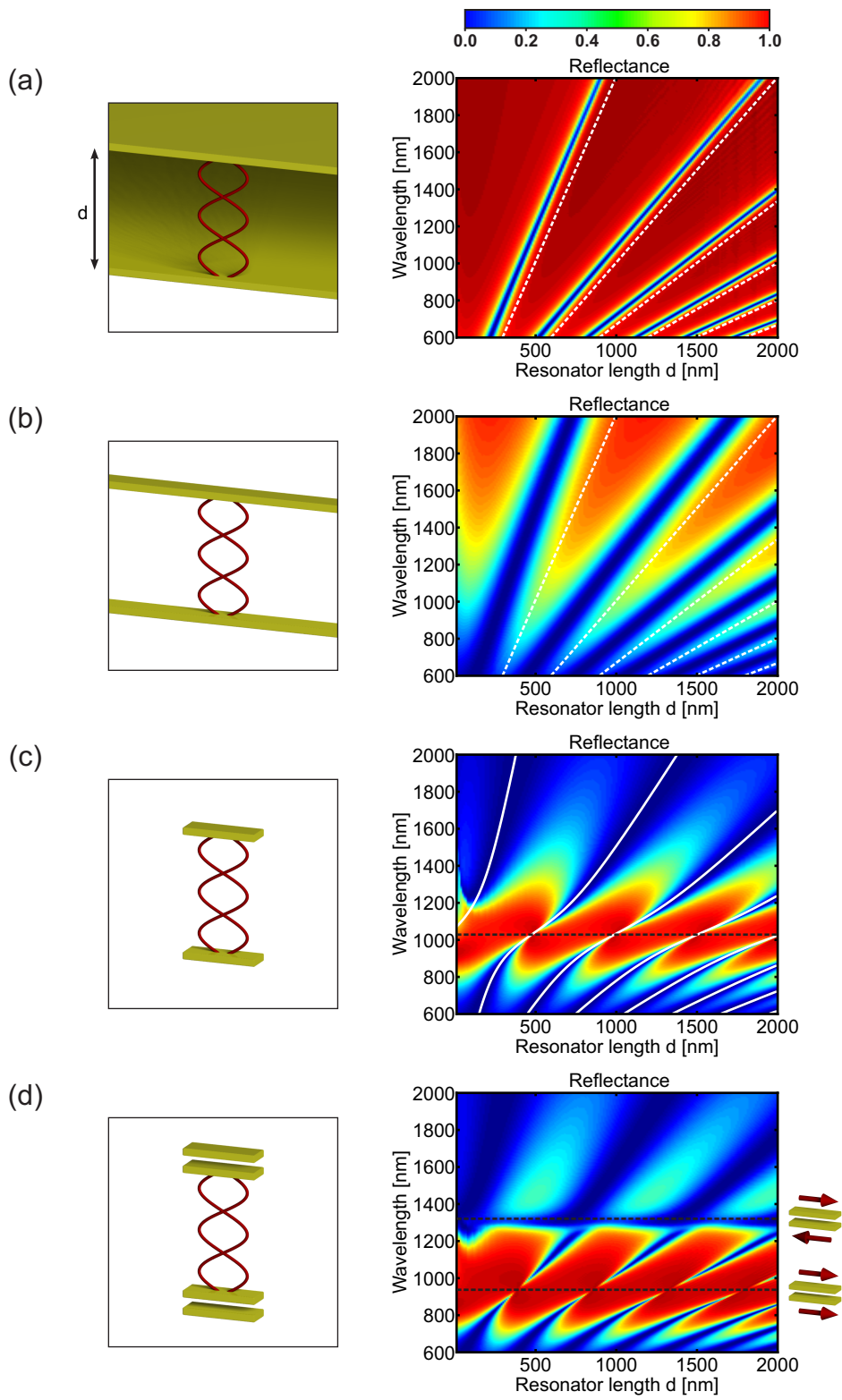
In Fig. 30(a) the resonances of a cavity consisting of thin gold mirrors can be identified in the reflectance plot. Compared to a cavity with perfect mirrors represented by the dashed white lines ($\lambda_N = \frac{2n_{\text{cav}}d}{N}$), the resonances are shifted due to the penetration depth in the gold layer and due to the effects of reflections on a thin layer [see Sec. 2.3.1]. The shift is around $\Delta\lambda \approx 100$ nm at a wavelength of $\lambda = 1000$ nm.

When the metal mirrors are replaced with continuous metal wires (polarization of incident light along the wire), this shift is increased to $\Delta\lambda \approx 200$ nm [Fig. 30(b)] and can be further increased the less metal is present in the structures forming the cavity. Structure sizes smaller than the wavelength cause effects that have to be explained in terms of effective structure parameters like in this case an effective metal density resulting in an effective mirror thickness and a corresponding reflection phase shift that shifts the cavity resonance accordingly.

For the case of two layers of plasmonic nanostructures with a large distance, the phase shift model is applied to calculate the resonances [Eq. 4.9]. For nanorods, the results are displayed as continuous white lines in the colored reflectance plots of Fig. 30(c). The model can accurately reproduce the simulated spectra for nanorod cavities. Fitting parameters are the plasmon damping parameter γ_{LP} and the localized plasmon resonance frequency ω_{LP} . When approaching the localized plasmon resonance (indicated by the horizontal dashed black line), the linewidth of the Fabry-Pérot modes is extremely decreased. Here, the spatial arrangement of the emitters matches their emission wavelength and the phase behavior is strongly modified. This large perturbation due to the strong phase dependence of the cavity resonances in this region will later be explored for plasmon sensing applications [Ch. 7].

In the case of two far-field coupled nanorod pairs [Fig. 30(d)] the additional influence of the hybridized plasmon modes can be observed. Besides the bending of the resonances around the symmetric plasmon resonance, additional perturbations around the antisymmetric plasmon resonance can be observed.

Figure 30 (following page): Reflectance spectra of nanostructured cavities with varying resonator length d . The cavity mirrors are formed by (a) plane metal layers, (b) continuous nanowires, (c) nanorods, and (d) nanorod pairs. The dashed white lines in (a) and (b) indicate the resonances for a cavity with perfect mirrors, the solid white lines in (c) indicate the resonances when the phase shift model is applied. The black lines in (c) and (d) correspond to the localized plasmon resonances of a single layer of nanorods and nanorod pairs.



The following geometric parameters were used for the simulations: The thickness of the plane metal mirrors is 10 nm, the continuous nanowires have a thickness of 30 nm and a width of 100 nm. The nanorods have a length of 300 nm, a width of 100 nm and a thickness of 30 nm. The distance between the two nanorods of a pair is 40 nm. The unit cell size is 500 nm \times 500 nm. The mirrors and nanostructures consist of gold with the simulation parameters defined in Sec. 2.2.2. The surrounding medium of all systems is vacuum including the interior of the cavities.

The simulated spectra could accurately be reproduced experimentally by R. Taubert [113] for the case of two layers of stacked nanowires by a series of fabricated samples covering the near- and far-field coupling regime.

4.3.4 MULTILAYER STACKS

In order to proceed towards an understanding of three-dimensional materials made of plasmonic nanostructures, multilayer stacks of plasmonic nanorods and nanowires have been simulated. The color plots in Fig. 31 show the resonances of five layers of nanorods compared to five ordinarily coupled cavities. In general, each cavity resonance is split into N modes in the case of N coupled cavities. Thinner metal layers lead to a better coupling of the cavities and therefore to a larger splitting. Extensive treatments of coupled cavities can be found in the context of metal-dielectric stacks (or one-dimensional photonic crystals), for example in [104].

For a medium consisting of several layers of nanostructures that are coupled vertically via their far-field, a combination of the effects of coupled multilayer mirror cavities [Fig. 31(a)] and a two-layer far-field coupled nanorod cavity [Fig. 30(c)] can be observed. First, the resonances are split with the splitting magnitude being dependent on the effective density of the plasmon layer determined by the thickness and shape of the nanostructures. The number of split modes is determined by the number of coupled cavities. The formation of band gaps already takes place at a very small number of cavities which can be attributed to the relatively long plasmon lifetime. The cross-sections in Fig. 31 point out the formation of band gaps for a five layer structure. The second effect is the perturbation of the modes around the plasmon resonance frequency. By tuning the plasmon resonance (via the nanorod length) and the layer distance, these kind of structures offer the possibility to fabricate materials with tailored reflection and transmission properties using only a small number of stacked layers.

For the simulations, the same geometric and material parameters as in Sec. 4.3.3 were used. The simulated results could be confirmed experimentally by R. Taubert with a structure consisting of four layers of stacked continuous nanowires [114].

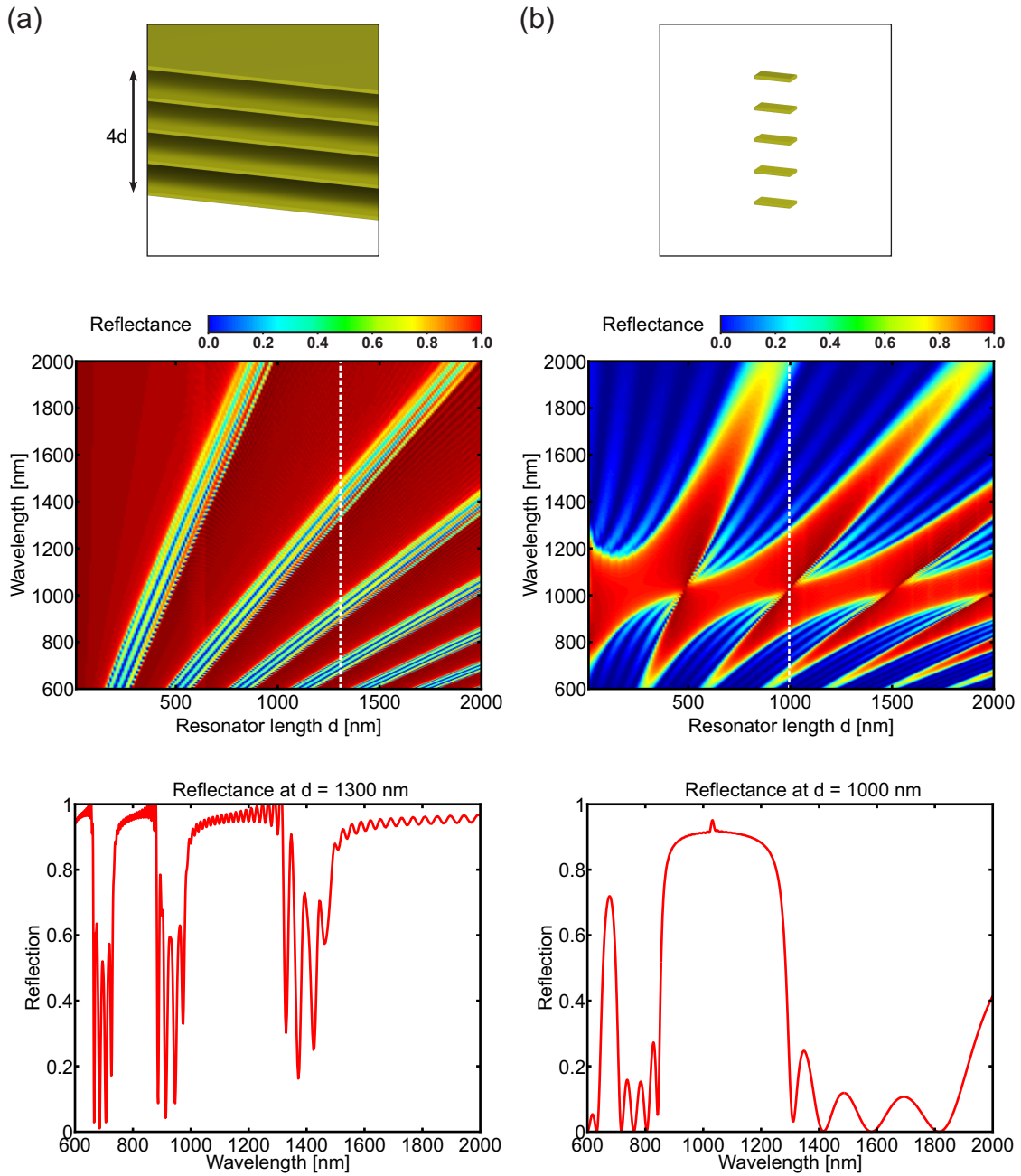


Figure 31: Reflectance plots of multilayer cavities consisting of (a) plane metal layers and (b) metal nanorods. The graphs correspond to cross-sections in the color plots indicated by the dashed white lines.

5 STRONG COUPLING OF PHOTONIC AND LOCALIZED PLASMON MODES

5.1 INTRODUCTION

Microcavities confine the electromagnetic field within a very small volume and allow large field enhancement [111, 91, 88, 5] [see also Sec. 2.3.1]. When combined with radiating species, such as atoms [116], molecules [24, 19, 30, 35], or semiconductor excitons [120], strong coupling between the optical modes of the microcavity and resonant modes of the emitters can occur. This strong coupling has been utilized in the past to demonstrate enhancement and inhibition of spontaneous emission [76, 47] or to tailor the photon statistics [119]. Also vacuum Rabi-splitting of excitons in quantum dots has been observed [100, 128]. An additional feature of microcavities is their ability to couple two radiating systems via the optical far-field over a larger distance [42, 43] [see also Sec. 2.3.1 and Sec. 4.3.3].

In this chapter, strong coupling between localized plasmons in nanorod pairs and photonic modes of a microcavity is presented. Furthermore, it is demonstrated that the field symmetry of the microcavity modes can excite symmetric and antisymmetric localized plasmon modes in a nanorod pair that are associated with electric and magnetic dipoles. The coupling strength depends on the nanorod position in the microcavity. The design allows especially strong coupling of light to the generally weakly excited magnetic dipole and can serve as a model for far-field coupling of localized particle plasmons in individual layers of stacked metallic metamaterials [107, 112]. The work accounts for a better understanding of the coupling of multiple localized plasmons in three-dimensional metamaterials [61, 130].

5.2 STRONG COUPLING

5.2.1 STRONG COUPLING OF QUANTUM EMITTERS AND LIGHT

In the past, strong coupling between photons and many different emitters has been observed. In 1992, it was the first time that mode-splitting due to the strong coupling of a photonic cavity mode to a two-level atom has been observed [116]. In that experiment,

a cavity is tuned in such a way that it has the same resonance frequency as the atomic transition [Fig. 32]. To obtain then a periodic energy exchange between the cavity mode and the atom, there are three important factors that play a key role:

- the coupling strength g of the electric field to the atom which is proportional to the electric field inside the cavity and to the dipole moment of the excited atom state
- radiation losses at the mirrors κ_M
- losses due to spontaneous emission of the atom in any direction κ_E

When two modes of the same energy are coupled, the modes are split around the common resonance frequency ω_0 . In the spectrum, the coupling strength g determines the extent of the splitting. The irreversible decay channels κ_M and κ_E describe the ways a

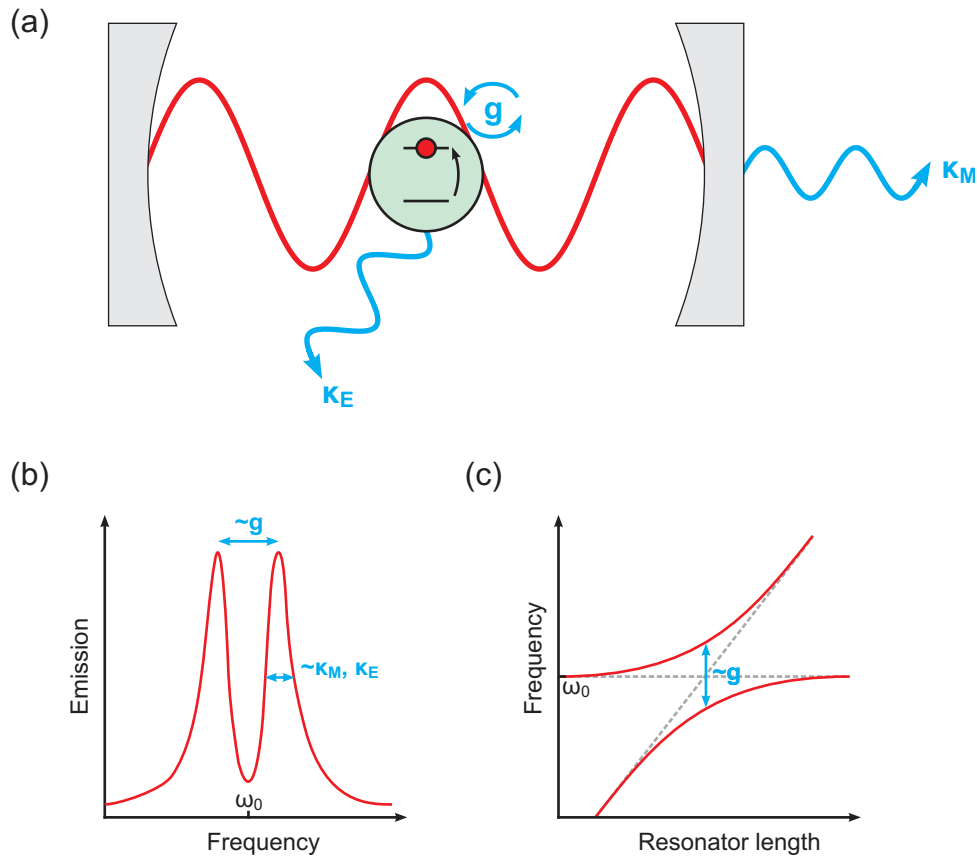


Figure 32: (a) Strong coupling of a two-level atom in a cavity with the coupling strength g and the irreversible decay channels at the mirrors κ_M and due to spontaneous emission κ_E . (b) Splitting of the resonances around the resonance frequency of the emitter ω_0 . (c) Anticrossing behavior of the resonances when the cavity resonance is detuned around the emitter resonance.

Emitter	Cs-Atom	InAs QD	InGaAs QD	GaAs QD
Cavity	Mirrors	Photonic Crystal	Micropillars	Microdisk
Splitting / Linewidth	5	1.3	0.7	2.2
Date of experiment	2004 [9]	2004 [128]	2004 [100]	2005 [92]

Table 2: Comparison of different systems exhibiting Rabi-splitting [48] (QD = quantum dot)

photon can leave the coupled atom-cavity state and determine the linewidth of the resonances. If g is large in comparison, then a mode-splitting can be observed and strong coupling is achieved.

In Tab. 2, some experimental results of the last years are compared. Besides atoms, the same effects can be observed for any quantum emitter, also for quantum dots or quantum wells. Instead of a classical cavity, one can also use a photonic crystal with a photonic band gap, Bragg-mirrors, or metal layers. A measure for the quality of a coupling experiment is the relation of the splitting energy and the spectral linewidth. For atoms, values up to 5 have been achieved, for quantum dots, the best measured value so far is 2.2.

5.2.2 TRANSITION TO PLASMONIC SYSTEMS

The transition of the concept of strong coupling between photonic cavity modes and an emitter to plasmonic systems is straight forward. Instead of the Rabi-splitting for the atoms, which is a quantum effect, now the classical polariton splitting of the plasmons occurs. The atom-field coupling strength becomes the plasmon field coupling strength which is proportional to the plasmon dipole moment and the electric field. Also, radiation losses at the mirrors play a role: in the regarded structures, thin gold metal layers were used as mirrors. Finally, κ_E corresponds to the dephasing rate of the plasmons associated with the damping frequency of the metal. The investigated coupled photonic-plasmonic system consists of an array of gold nanorods or nanorod pairs located inside a microcavity that is made out of a dielectric material surrounded by two gold layers that act as the mirrors [Fig. 33].

This coupled photonic-plasmonic system can be described with the Hamiltonian

$$H = \begin{pmatrix} E_N & g \\ g & E_{LP} \end{pmatrix} \quad (5.1)$$

with the energy of the N -th photonic cavity mode $E_N = \hbar\omega_N$, the energy of the localized plasmon mode $E_{LP} = \hbar\omega_{LP}$, and the coupling constant g . The solution of the stationary

Schrödinger equation

$$H\Psi = \begin{pmatrix} E_N & g \\ g & E_{LP} \end{pmatrix} \begin{pmatrix} \psi_N \\ \psi_{LP} \end{pmatrix} = E \begin{pmatrix} \psi_N \\ \psi_{LP} \end{pmatrix} \quad (5.2)$$

with the eigenstate of the polariton Ψ being composed of the eigenstates of the cavity ψ_N and the plasmon ψ_{LP} yields the dispersion of the coupled system. At the point where E_N equals E_{LP} , this results in a mode splitting of $2g$.

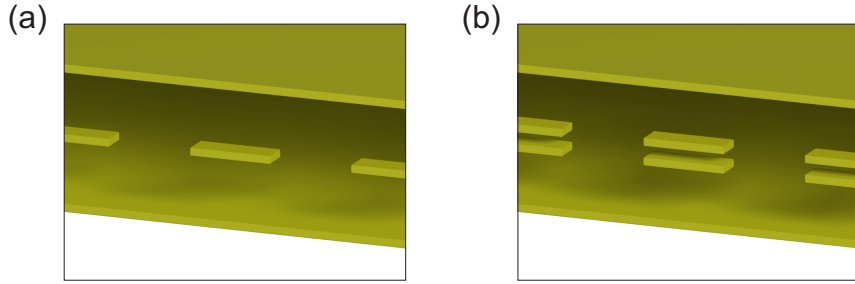


Figure 33: (a) Nanorods and (b) nanorod pairs in a microcavity constitute a strongly coupled photonic-plasmonic system.

5.3 SINGLE NANORODS IN A MICROCAVITY

At first, a layer of single nanorods is placed into the center of a microcavity [Fig. 34]. The geometric parameters of the nanorods are again $300 \text{ nm} \times 100 \text{ nm} \times 30 \text{ nm}$ (length \times width \times thickness) with an array unit cell size of $500 \text{ nm} \times 500 \text{ nm}$. To compare the simulated spectra with experimental measurements, the simulated material parameters were adjusted to the fabricated samples. This means the cavity is filled with a dielectric with the refractive index $n_{IC1} = 1.40$ and is surrounded by a substrate with $n_{\text{sub}} = 1.45$ on the lower side and by air on the upper side. The mirrors as well as the nanorods themselves are made out of gold with the parameters from Sec. 2.2.2. The localized plasmon resonance wavelength of the isolated nanorod (in the dielectric medium) is in this case $\lambda_{LP} = 1480 \text{ nm}$.

The resonances of an empty cavity appear as straight lines in the color-coded reflectance plot of Fig. 34 and are here indicated by black dashed lines and their mode numbers N . The localized plasmon eigenmode is indicated by the horizontal white dashed line. When the resonance wavelengths of the cavity are close to the plasmon resonance of the nanorod, the described polariton splitting can be observed. A closer look reveals that only the odd cavity modes ($N = 1, 3, 5, \dots$) are influenced. They show a huge anticrossing with a splitting of several hundred nanometers whereas the even modes ($N = 2, 4, 6, \dots$) remain totally unperturbed.

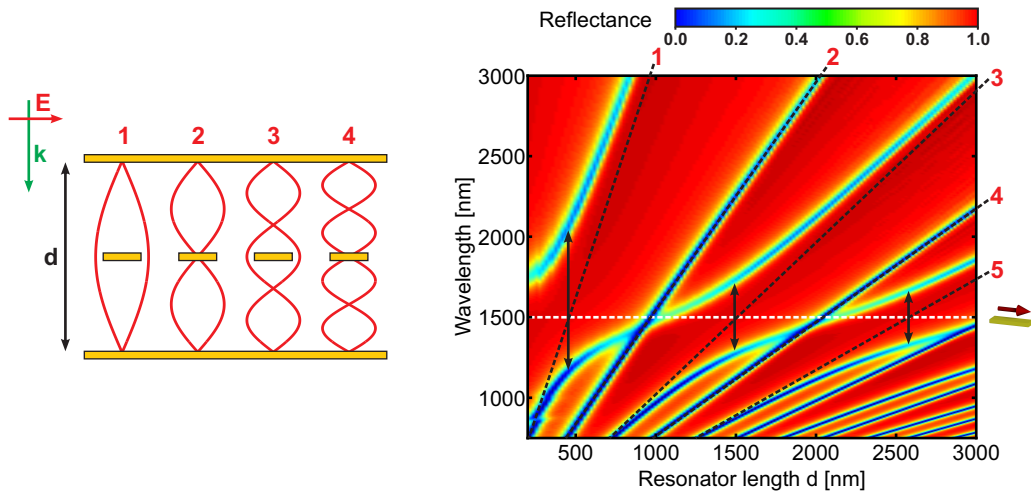


Figure 34: Single nanorods in a microcavity and the corresponding reflectance plot for different wavelengths and resonator lengths. The dashed white and black lines correspond to the unperturbed plasmon and cavity modes. Around every second intersection of the modes, an anticrossing is observable (indicated by black arrows).

The mode splitting is proportional to the coupling strength g which is proportional to the electric field strength. Hence, the behavior of the modes can be explained by regarding the symmetry of the electric fields in the cavity: For the odd modes, there is an electric field anti-node located in the center of the cavity where the nanorods are located. This means the field strength at these positions is very high leading to a large interaction and therefore a strong coupling of the photonic cavity mode to the plasmon. For the even cavity modes, the situation is totally different. Here, we have an electric field node in the center of the cavity. This means that the field is close to zero at the position of the nanorods. Hence, the plasmons cannot be excited, no interaction can take place, and the modes remain unaffected.

5.4 NANOROD PAIRS IN A MICROCAVITY

5.4.1 ELECTRIC AND MAGNETIC COUPLING

Very interesting effects occur when the single nanorods are replaced by nanorod pairs [Fig. 35(b)]. In addition to the symmetric plasmon mode of the nanorod pair, the anti-symmetric mode can interact with the cavity modes. The plasmonic structure can now

exhibit two different resonances and Eq. 5.2 has to be extended to

$$H\Psi = \begin{pmatrix} E_N & g_{\uparrow\uparrow} & g_{\uparrow\downarrow} \\ g_{\uparrow\uparrow} & E_{\uparrow\uparrow} & 0 \\ g_{\uparrow\downarrow} & 0 & E_{\uparrow\downarrow} \end{pmatrix} \begin{pmatrix} \psi_N \\ \psi_{\uparrow\uparrow} \\ \psi_{\uparrow\downarrow} \end{pmatrix} = E \begin{pmatrix} \psi_N \\ \psi_{\uparrow\uparrow} \\ \psi_{\uparrow\downarrow} \end{pmatrix} \quad (5.3)$$

with the indices $\uparrow\uparrow$ and $\uparrow\downarrow$ denoting the symmetric and antisymmetric localized plasmon resonance.

In the considered case, the two nanorods are separated by a 40 nm thick spacer with the refractive index $n_{\text{MgF}_2} = 1.38$. All other material parameters are the same as in the previous section. The resonance wavelengths of an isolated nanorod pair are then $\lambda_{\uparrow\uparrow} = 1320$ nm for the symmetric and $\lambda_{\uparrow\downarrow} = 1760$ nm for the antisymmetric plasmon mode.

The modifications of the resonances in the reflectance plots of Fig. 35(b) explain what is going on in this coupled system: The odd modes are only split around the resonance wavelength of the symmetric plasmon mode whereas the even modes are only split around the resonance wavelength of the antisymmetric plasmon mode. In the center of the resonator, the electric field vectors of the odd modes point into the same direction for both nanorods of a pair, so only the symmetric mode can be excited. The field amplitude is close to the maximum for the odd modes near the nanorod spatial region, therefore also the coupling $g_{\uparrow\uparrow}$ is strong. The even modes, however, possess an electric field node directly in between the two nanorods, resulting in opposite directions of the electric field vector for each nanowire, exciting only the antisymmetric mode. Since the field amplitude is low around the node, the strong coupling between the even modes and the plasmon $g_{\uparrow\downarrow}$ is less pronounced. One might also look at the interaction from a magnetic viewpoint [67]. The magnetic field in the microcavity is maximum at the nodes of the electric field. Hence, the interaction with the antisymmetric (magnetic) nanorod pair modes is then strongest at such locations.

5.4.2 VARIATION OF PLASMON POSITION

To verify the explanations of the previous section, the nanorod pairs are placed at different positions in the cavity. The nanorods are positioned in such a way that the ratio of the distances to the two gold cavity mirrors are $d_1 : d_2 = 1 : 2$ and $1 : 3$. When placed around an electric field node of the third cavity mode [Fig. 36(a)], this mode can couple only to the antisymmetric plasmon mode and not to the symmetric plasmon mode anymore. The other cavity modes couple only to the symmetric mode. Similar observations apply for nanorod pairs placed around the electric field node of the fourth cavity mode [Fig. 36(b)].

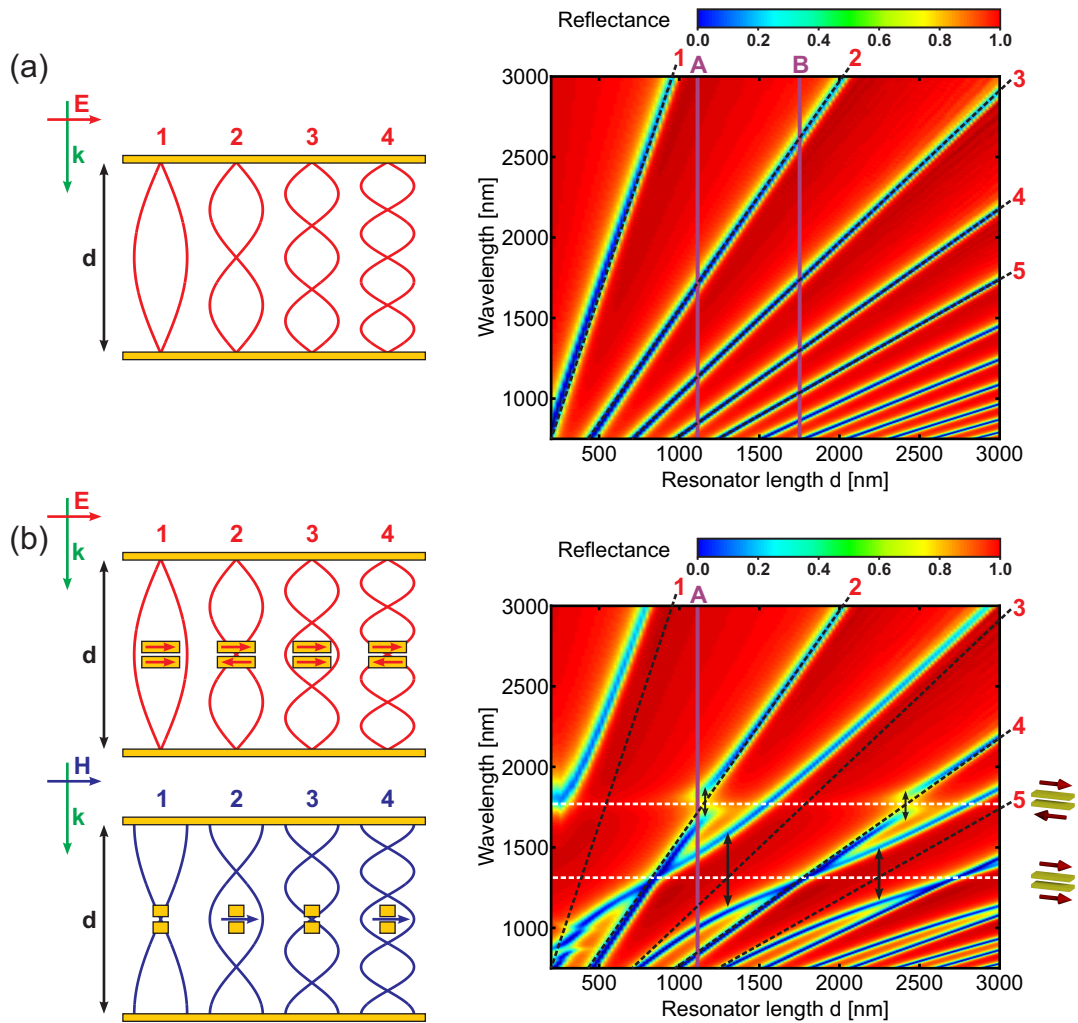


Figure 35: (a) Empty microcavity and (b) nanorod pairs in a microcavity with the corresponding reflectance plots for different wavelengths and resonator lengths. The dashed white and black lines correspond to the unperturbed plasmon and cavity modes. The mode splitting is indicated by the black arrows. The vertical violet lines (marked A and B) denote the positions of the fabricated samples [see Sec. 5.4.4].

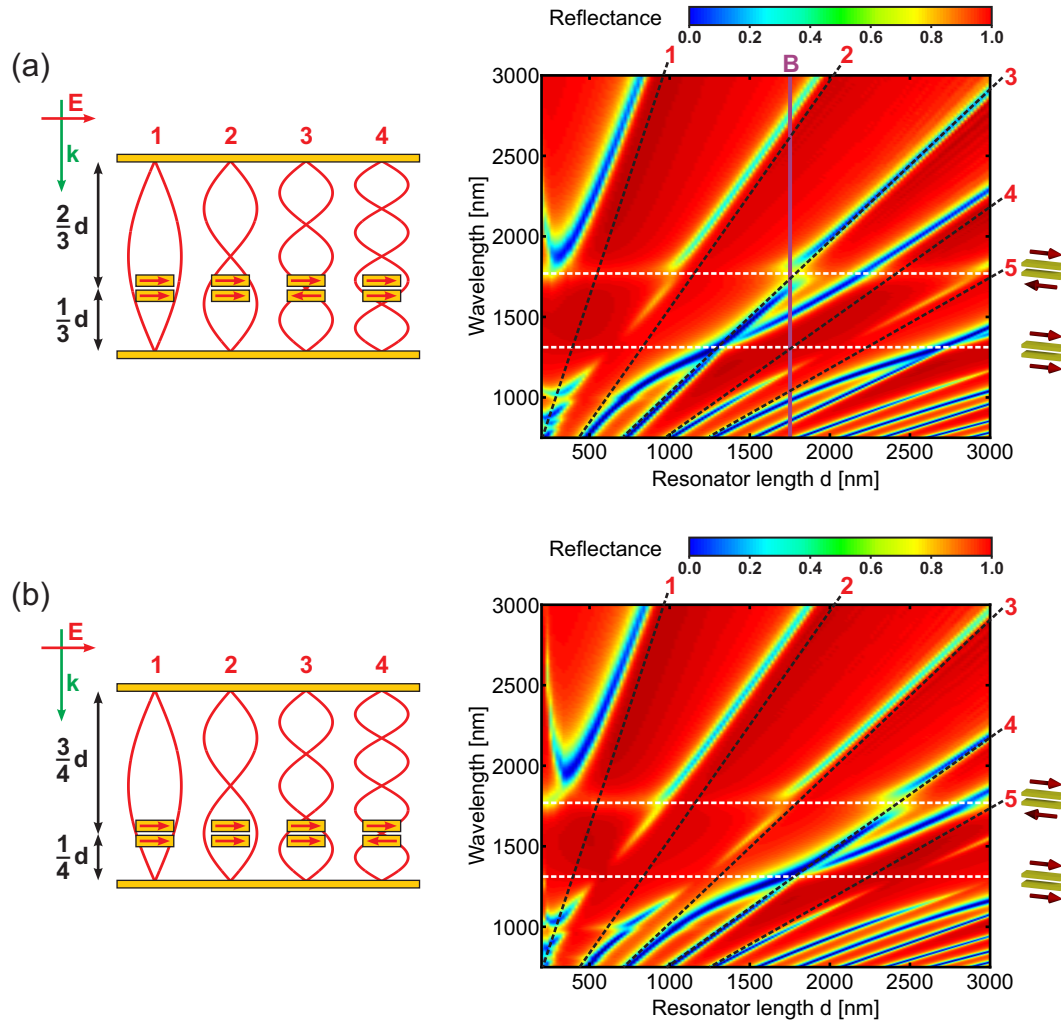


Figure 36: Nanorod pairs in a microcavity placed at an electric field node of the (a) third and (b) fourth cavity mode including the corresponding reflectance plot for different wavelengths and resonator lengths. The dashed white and black lines correspond to the unperturbed plasmon and cavity modes. The vertical violet line (marked B) denotes the positions of the fabricated sample [see Sec. 5.4.4].

5.4.3 NATURE OF THE MODES

The field plots in Fig. 37 provide a deeper insight concerning the nature of the split modes. In a nanorod pair, the electric fields in the nanorods point in the same direction for the symmetric and in opposite directions for the antisymmetric plasmon mode [see Fig. 25]. The coupling of the third resonator mode to the symmetric plasmon mode is illustrated in

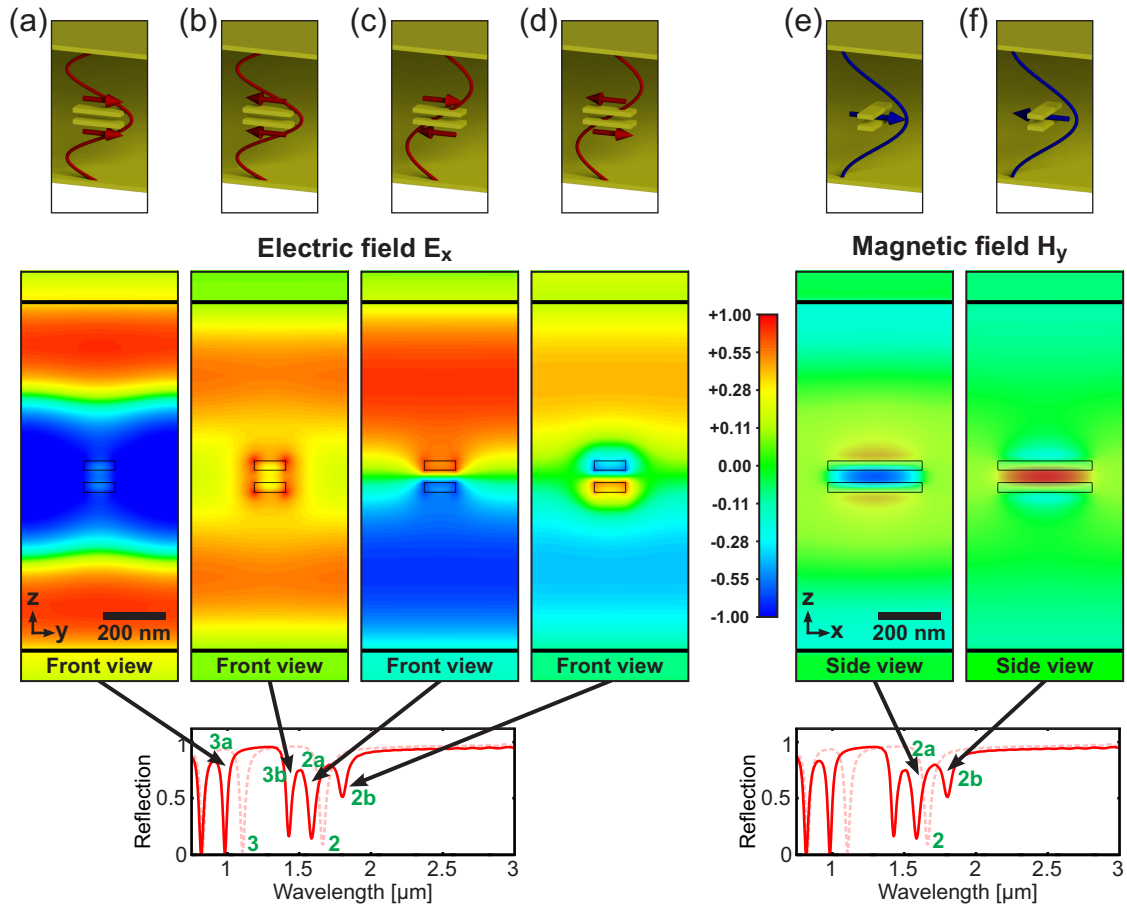


Figure 37: Plots of the electric (a-d) and magnetic (e,f) field distributions (logarithmic color scale) at the various resonances of a pair of nanorods in a microcavity. (a) and (b) show the x-component of the electric field in the y-z-plane for the third cavity mode (3) that is split in two modes (3a and 3b) due to strong coupling to the symmetric plasmon mode. (c) and (d) show the same field for the second cavity mode (2) that is split in two modes (2a and 2b) due to strong coupling to the antisymmetric plasmon mode. The reflectance spectra below corresponds to cross-sections (marked A) of the color plots in Fig. 35(a) and (b). The solid lines denote the reflectance of nanorod pairs in a microcavity, the dashed lines show the unperturbed modes of an empty cavity [compare with Fig. 39]. (e) and (f) show the y-component of the magnetic field of the split second resonator mode (2) in the x-z-plane.

Fig. 37(a, b). The electric field points into the same direction in both nanowires, whereas it points into opposite directions for the coupling of the second resonator mode to the antisymmetric plasmon mode in Fig. 37(c, d). Note that the two split resonances of one microcavity mode differ in such a way that the plasmon oscillation is in phase with the microcavity mode for the resonance at the lower wavelength and antiphase for the resonance at the higher wavelength. Fig. 37(e, f) finally shows magnetic fields that belong to the third cavity mode and the corresponding strong magnetic dipoles that are exhibited by the antisymmetric plasmon modes. For the split mode with the lower wavelength, the induced magnetic dipole oscillates in phase with the magnetic field of the cavity mode, for the split mode with the higher wavelength, the magnetic dipole oscillates antiphase.

5.4.4 FABRICATION DETAILS

The samples were fabricated using physical vapor deposition [Sec. 3.2] for the metals and the magnesium fluoride (MgF_2) spacer layers, spin coating for the thick dielectric layers in the microcavity, and electron beam lithography for the nanostructuring. With these techniques the investigated structures can be manufactured in a layer-by-layer fashion. First, a 20 nm thick gold layer serving as the lower mirror is evaporated on an Infrasil glass substrate that has been coated with 3 nm chromium for a better adhesion of the gold. Thereafter, the first dielectric spacer between the gold-layer and the later nanorods is spin-coated. For the spacer we use the polysiloxane-based spin-on glass IC1-200 in different mixing ratios with butanol, resulting in different layer thicknesses [see Sec. 3.2]. The spacer consists of one or more dielectric coating layers with different mixing ratios. Subsequently, the positive resist is spun onto the sample in which the nanorod pattern is written by electron beam lithography. After the exposure and the development, the sample is coated with 30 nm Au, 40 nm MgF_2 , and 30 nm Au. By leaving the sample in acetone for several hours, the unexposed PMMA as well as the gold and magnesium fluoride layers thereon are removed (lift-off), and only the nanorod pairs on the dielectric coating remain [see also Sec. 3.4]. The period of the nanorod array is 500 nm in both directions, the length of the rods is around 300 nm, the width 100 nm. For planarization a 100 nm thick layer of IC1-200 and subsequently the upper dielectric spacer is spun on the sample. Finally, 20 nm gold is evaporated forming the upper mirror of the cavity.

Two samples (A and B) have been produced in the above explained manner [Fig. 38] to confirm the simulated results experimentally. One sample (A) has been produced with the nanorod pairs located in the center of the resonator. The resonator length of sample A is 1100 nm. This is approximately the length where the second resonator mode wavelength equals the antisymmetric plasmon mode wavelength. By regarding the reflectance plot in Fig. 35(b), one recognizes that both kind of splittings (around the symmetric and around the antisymmetric plasmon mode) should be visible in a measured spectrum at this position. In the second sample (B) the nanorod pairs are positioned in such a way that the

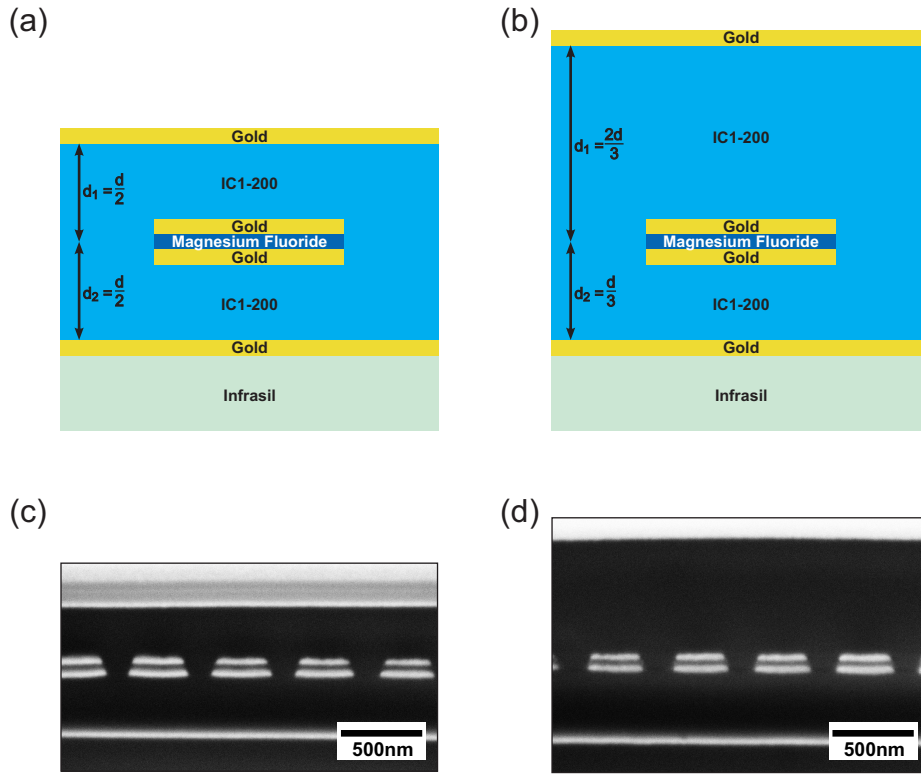


Figure 38: (a, b) Sketches of the two fabricated samples A and B. (c, d) SEM-images of focussed ion beam cuts of the two samples providing a side view on the different layers.

ratio of the distances to the two gold cavity mirrors is $d_1 : d_2 = 1 : 2$. The total resonator length is 1740 nm. Around this length, the wavelength of the third resonator mode equals the antisymmetric plasmon mode wavelength. From Fig. 36(a) one can expect to see a coupling of the third resonator mode to the antisymmetric plasmon mode and of the fourth resonator mode to the symmetric plasmon mode under these conditions.

5.4.5 EXPERIMENTAL RESULTS

Each measured reflection spectrum of a fabricated sample [Fig. 39] corresponds to one cross-section in the color-coded reflectance plots of Figs. 35 and 36(a) (marked as vertical violet lines A and B). Additional reflection spectra were recorded away from the structure to measure the unperturbed resonance modes and thus determine the resonator length. The reflection and transmission spectra have been measured with a Fourier transform infrared spectrometer [see Sec. 3.5] using a Si-diode and an MCT-detector and linearly polarized light.

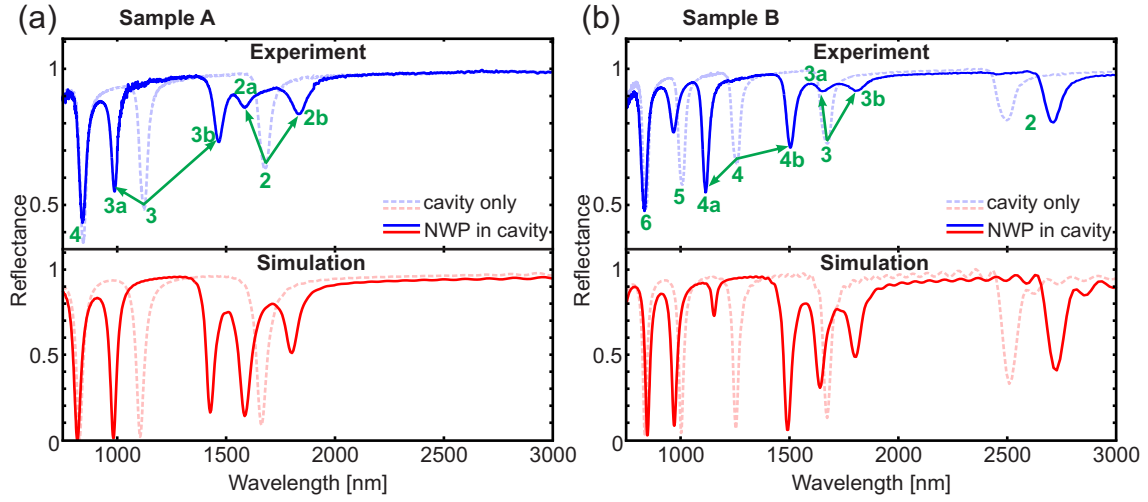


Figure 39: Comparison of measured and simulated reflection spectra. (a) Sample A: Nanorod pair in a central position in the resonator ($d_1 = d_2 = 550$ nm). (b) Sample B: Nanorod pair in a non-central position in the resonator ($d_1 = 580$ nm, $d_2 = 1160$ nm). The dashed lines in the background correspond to the reflectance spectra of an empty cavity.

The measured spectrum of sample A is in good agreement with the simulation [Fig. 39(a)]. Around $\lambda_{\uparrow\downarrow} = 1760$ nm, the splitting of the second mode (2) into two peaks (2a, 2b) around the antisymmetric plasmon mode can be clearly observed. Additionally, the large splitting of the third mode ($3 \rightarrow 3a, 3b$) due to its strong coupling to the symmetric plasmon mode is evident. Finally, the higher modes remain mostly unaffected for this resonator length. The relative difference in the strength of the modes in experiment and simulation can be explained by the fact that the thickness of the spacer layers between nanorod pair and metal mirror is subject to variations.

Sample B has a resonator length of 1740 nm. Around this length, the wavelength of the third resonator mode (3) equals the antisymmetric plasmon mode wavelength. Due to the non-central position of the nanorod in the cavity, strong coupling between the third mode and the antisymmetric plasmon mode evident through a large mode splitting can be observed [see Fig. 39(b)]. The strong coupling of the fourth mode (4) to the symmetric plasmon mode can also be seen in the measured spectrum characterized by a splitting into two well-separated peaks (4a and 4b). The second resonator mode (2) does not split up for this resonator length and is only slightly shifted.

5.4.6 SPLITTING ENERGIES

The splitting of the modes is determined by the strength of the coupling. As pointed out in Sec. 5.2.1, strong coupling is achieved when the ratio of the splitting and the linewidth of the modes is larger than 1. In Tab. 3, the simulated and measured splitting wavelengths and energies, as well as the ratios of the splittings over the linewidths are compared for the different coupled modes. The simulated splitting values are taken at resonator lengths corresponding to those of the fabricated samples [Sec. 5.4.4]. These resonator lengths do not always correspond exactly to the values where the unperturbed plasmon and cavity modes would intersect. The splitting energies simulated around the exact crossing of the modes are slightly smaller [see Fig. 35(b)]: for the coupling to the symmetric plasmon mode, a splitting energy of 354 meV (38 % of resonance energy) was simulated, for the coupling to the antisymmetric mode the corresponding value was 82 meV (12 % of resonance energy), both for the structure with the nanorod pair in the center of the cavity. For the off-central position of the nanorod pairs, slightly smaller values were determined. All measured and simulated ratios of the splitting energy and the linewidth of the resonances are larger than 1 (up to 8.9 for the symmetric coupling). Therefore, strong coupling of photonic and localized plasmonic modes has been demonstrated for all studied structures.

$d_1 : d_2$	Coupled modes	Splitting		$\frac{\text{Splitting energy}}{\text{Resonance energy}}$	$\frac{\text{Splitting}}{\text{Linewidth}}$
1:1	$\uparrow\downarrow$ to 2	216 nm (253 nm)	94 meV (108 meV)	13% (15%)	2.7 (2.5)
1:1	$\uparrow\uparrow$ to 3	444 nm (479 nm)	392 meV (410 meV)	42% (44%)	8.9 (8.0)
1:2	$\uparrow\downarrow$ to 3	161 nm (152 nm)	68 meV (63 meV)	10% (9%)	2.0 (1.5)
1:2	$\uparrow\uparrow$ to 4	338 nm (388 nm)	244 meV (288 meV)	26% (31%)	6.7 (6.5)

Table 3: Mode splitting of nanorod pairs in a microcavity at different positions. d_1 and d_2 are the distances of the nanorods to the lower and upper cavity mirror. The coupled plasmon modes are indicated by $\uparrow\uparrow$ (symmetric) and $\uparrow\downarrow$ (antisymmetric), the coupled cavity modes are defined by their mode number N . The numbers in brackets are the measured values.

5.5 MULTILAYER NANORODS IN A MICROCAVITY

Finally, the effects of multiple layers of nanorods in a cavity are investigated. In agreement with Sec. 4.3.4, the splitting of each mode into a number of modes corresponding to the number of subcavities can be observed [Fig. 40]. However, in contrast to the case without limiting mirrors on the upper and lower side, the resonances remain well-separated and do not start to form band gaps. Here, the effect of the cavity of allowing only resonances at well-defined frequencies can be observed. In the case of nanorod pairs in a cavity, also the interaction with the antisymmetric plasmon mode manifests itself as small anticrossings around the plasmon resonance frequency.

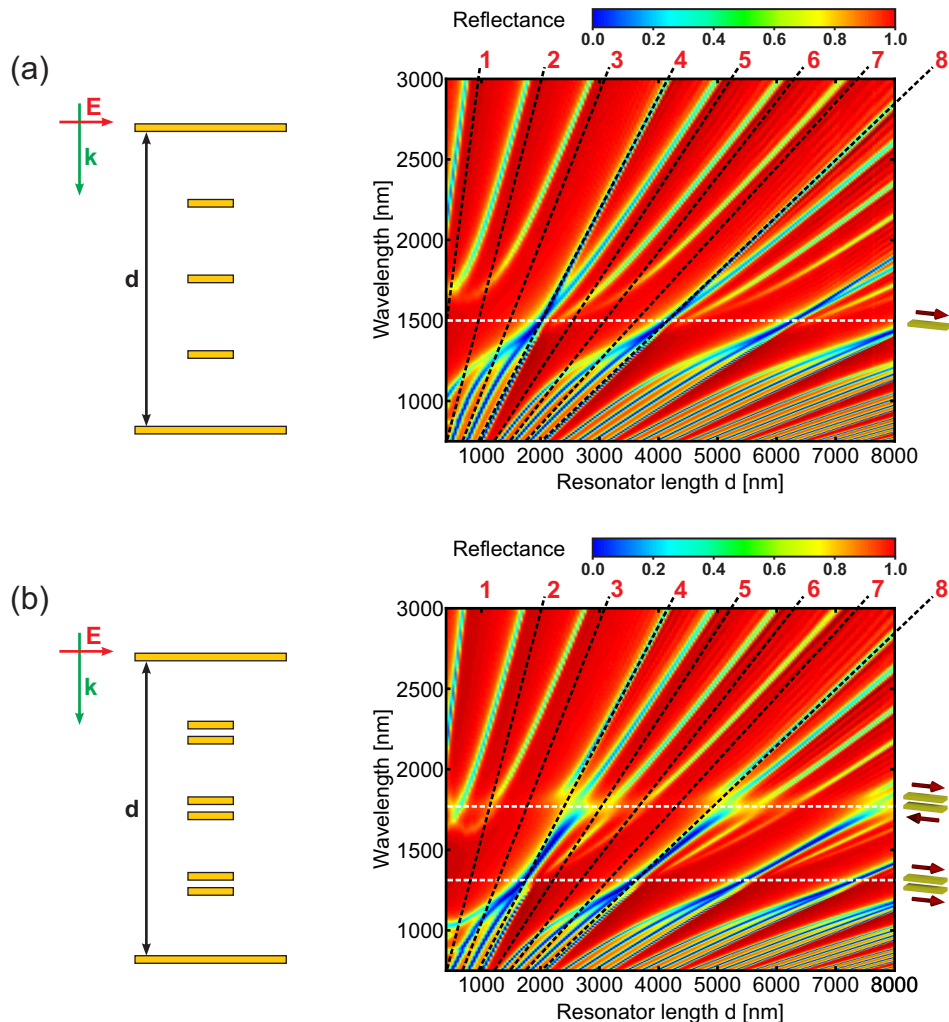


Figure 40: Reflectance plots of three layers of (a) single nanorods and (b) nanorod pairs in a microcavity for different resonator lengths d . Black and white dashed lines denote the unperturbed resonances of cavities and nanorods / nanorod pairs.

To understand the features of the resonances in more detail, it is again helpful to look at the symmetry of the electric fields of the cavity modes. The cavity modes with $N = 4, 8, 12, \dots$ possess electric field nodes at the positions of the single nanorods and in between two nanorods of a pair. This means on the one hand that the field strength is very low at the positions of the single nanorods, therefore no interaction takes place and the corresponding cavity modes remain unperturbed and appear as straight lines in Fig. 40(a). On the other hand, in the case of nanorod pairs, the electric field points into different directions for each nanorod of a pair, therefore the antisymmetric plasmon mode can be excited and small mode splittings appear around the antisymmetric plasmon resonance in Fig. 40(b).

All other modes have non-vanishing electric fields at the positions of the nanorods, so they can interact with the symmetric plasmon mode and show quite pronounced anti-crossings around the single nanorod and the symmetric nanorod pair resonance.

6 STRONG COUPLING OF PHOTONIC AND SURFACE PLASMON MODES

6.1 INTRODUCTION

In this chapter, strong coupling of surface plasmon modes on a thin metal layer via localized plasmons of nanowires to photonic microcavity modes is investigated. In analogy to the previous chapter, a modified environment is created by a photonic microcavity which manipulates the coupling strength of light to localized and surface plasmons and influences the plasmon resonances. In particular, an array of nanowires is placed close to a mirror, and a second mirror is positioned near Bragg distance. The distance has to be accurately controlled, since strong coupling can only be observed when the resonances of the photonic microcavity and the plasmons intersect. The coupling becomes evident from an anti-crossing of the resonances when the cavity resonance is detuned around the plasmon resonances. The resonant modes of the coupled system are experimentally determined for different resonator lengths by applying external pressure to the microcavity while recording the spectra. Excellent agreement with simulations is achieved.

Furthermore, it is demonstrated that a strong plasmon-plasmon interaction over far-field distances can be achieved by placing a second layer of nanowires also close to the opposite mirror of the cavity. The far-field interaction, which is mediated by the photonic microcavity modes, causes a splitting of both the localized and the surface plasmon modes.

6.2 STRUCTURE GEOMETRY AND COUPLING SCHEME

6.2.1 EXCITATION OF SURFACE AND LOCALIZED PLASMONS

In an isolated continuous metal nanowire, localized plasmons can be excited when the incident light is polarized perpendicular to the wire. The localized plasmon resonance wavelength λ_{LP} is determined by the width and thickness of the wire as well as the material parameters of the metal and the dielectric environment [see Sec. 2.4.4].

Placing a thin metal layer near an array of nanowires has two effects [Fig. 41(a)]. First, in analogy to electrostatics, the effects of a mirror close to a charged particle is equal to the

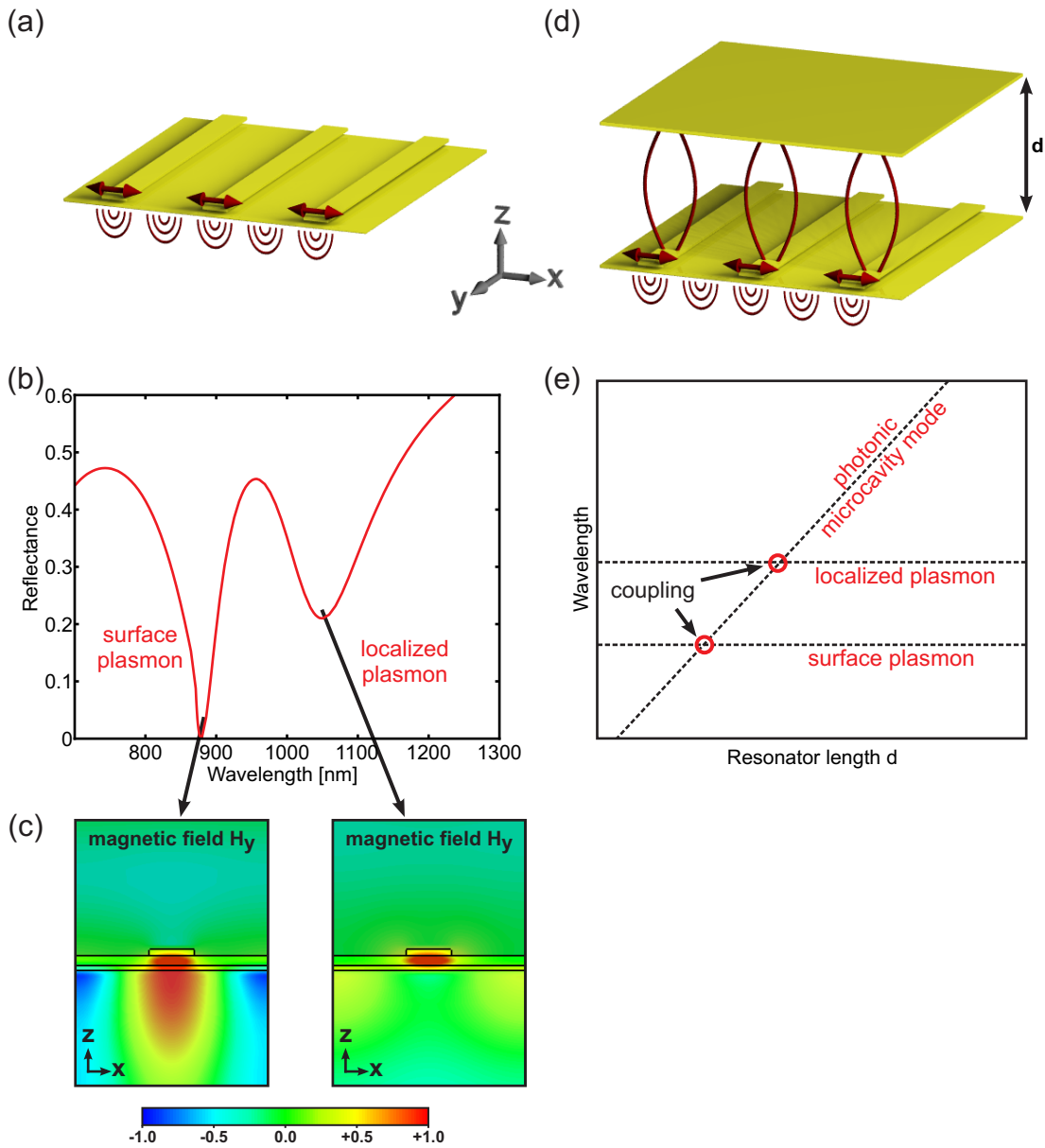


Figure 41: (a) In an array of metal nanowires close to a thin metal layer localized and surface plasmons can be excited (b). (c) The magnetic field plots of the two resonances reveal the nature of the two plasmon modes. (d) By adding a second metal layer, the microcavity modes can couple to the plasmon modes for those mirror distances d where the microcavity modes intersect with plasmon modes (e). The red lines in the structure illustrations indicate the standing electric fields. Illumination is from below with polarization along the x -direction.

effect of an image charge placed on the opposite side of the mirror with opposite charge [see Sec. 4.2.4. Hence, the system of a nanowire placed closely above a mirror resembles very much the system of a pair of stacked nanowires where the antisymmetric plasmon mode (magnetic mode) is excited [60, 12, 39]. Depending on the distance of the wire to the mirror, the resonance wavelength is shifted towards higher wavelengths. Using a dielectric spacer of 30 nm with a refractive index of $n = 1.38$ between wire and mirror and a mirror thickness of 15 nm, the localized plasmon resonance is shifted to $\lambda_{LP} = 1050$ nm for nanowires with a thickness of 20 nm and a width of 140 nm. In the same manner as for a nanowire pair, a magnetic dipole is induced for a nanowire close to a mirror.

The second effect is the grating-induced excitation of propagating surface plasmons on the metal-substrate interface [38, 17] [see Sec. 2.3.2]. For the used parameters, a nanowire period of $p_x = 600$ nm allows surface plasmons with a resonance wavelength of $\lambda_{SP} = 880$ nm [Fig. 41(b)]. By plotting the magnetic fields, the two resonances can be identified [Fig. 41(c)].

6.2.2 ENHANCING LIGHT-PLASMON COUPLING BY A PHOTONIC MICROCAVITY

In order to obtain strong coupling of light to the plasmon modes, a microcavity is formed by positioning a second mirror at a distance d to the nanowires [Fig. 41(d)]. The mirror consists of a 100 nm thick gold layer. When the distance d is varied, a strong interaction with the plasmon modes is expected each time when the cavity resonance is equal to a plasmon resonance [Fig. 41(e)]. From a magnetic point of view, the cavity modes can be coupled very effectively to the magnetic plasmon modes due to their strong magnetic field (anti-nodes) near the mirrors. The mode coupling causes an anti-crossing of the resonances and can be observed in the simulated reflectance plot of Fig. 44(a). The simulations were performed using a Fourier model based Maxwell solver [see Sec. 2.5.2]. Gold is described by a Drude model with the plasma frequency $\omega_p = 1.37 \times 10^{16}$ THz [85] and the damping frequency $\omega_c = 3.6 \times 10^{14}$ THz. To account for surface scattering and grain boundary effects in thin films as well as inhomogeneous broadening due to fabrication imperfections, the damping is here chosen about three times larger than the reported values for bulk gold.

6.2.3 FABRICATION AND MEASUREMENT TECHNIQUE

The experimental realization of this structure has been accomplished as follows: First, a gold layer and a magnesium fluoride layer ($n_{MgF_2} = 1.38$) are evaporated on a glass substrate ($n_{sub} = 1.45$). The nanowires are fabricated by electron beam lithography using a positive resist procedure with a final lift-off [Sec. 3.4]. Fig. 42 displays a top and side view of the fabricated structure. The second mirror is evaporated on a second glass substrate which is then turned around and pressed onto the nanowire array. The pressure

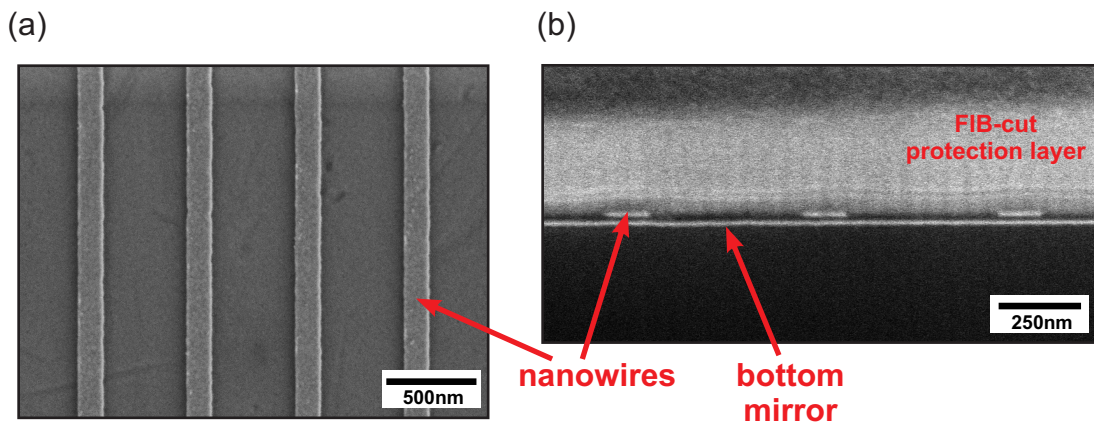


Figure 42: Scanning electron microscope image of the structure. (a) Top view and (b) side view obtained by a focussed ion beam cut.

is applied via a small annular stamp around the region where the nanowire array with a total size of $700\ \mu\text{m} \times 700\ \mu\text{m}$ is written [Fig. 43]. Using this technique, the microcavity length can be tuned from several micrometers to only a few hundred nanometers by simply changing the mechanical pressure. By placing the whole device in a Fourier-transform infrared spectrometer (Bruker Vertex 80) with an attached infrared microscope [Sec. 3.5], the behavior of the resonances of the system can be measured by recording the reflected light for a series of different microcavity lengths. Furthermore, the sample was placed on a wedge to obtain normal incidence from the microscope's Cassegrain objective [see Sec. 3.5]. The reflectance plot that was experimentally obtained in this way [Fig. 44(b)] corresponds very well to the simulated one.

In order to determine the actual distance of the mirrors, the polarization is turned by 90° . This way, the incident light is polarized along the continuous nanowires. Hence,

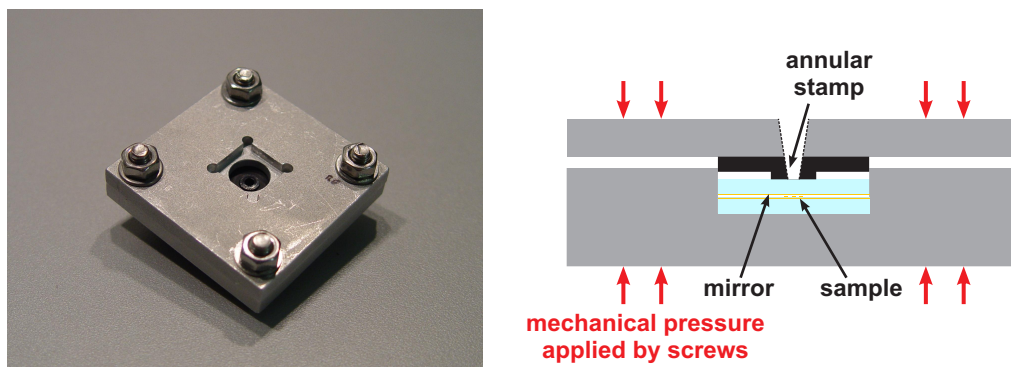


Figure 43: Setup used to press the mirror onto the sample.

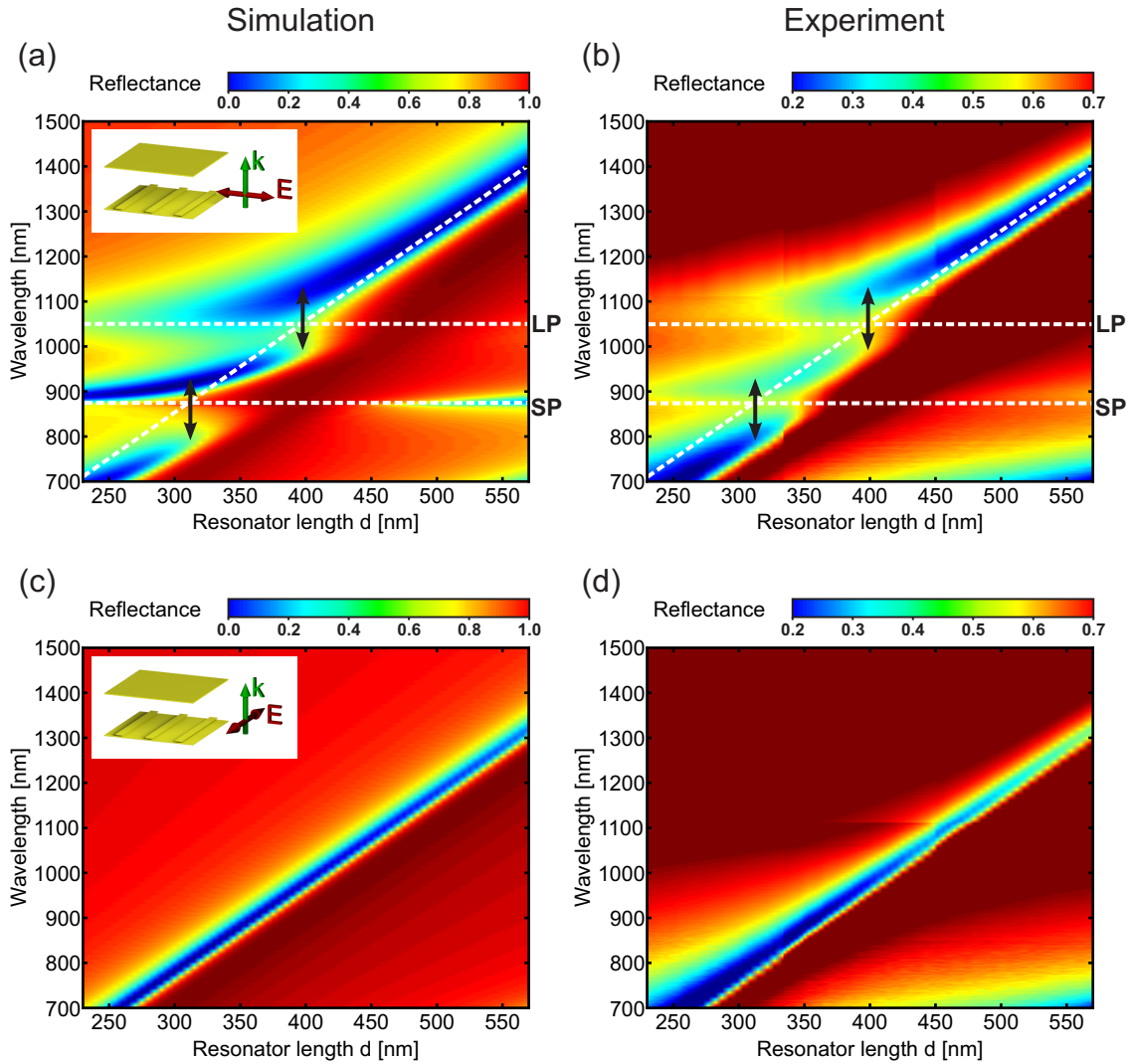


Figure 44: (a,c) Simulated and (b,d) measured reflectance for different microcavity lengths d . For incident light polarized perpendicular to the nanowires (a,b), the anticrossings of the modes caused by the strong coupling of the plasmons to the cavity modes can be observed (indicated by black arrows). The white dashed lines denote the localized plasmon (LP) and surface plasmon (SP) resonances as well as the unperturbed cavity resonance. For incident light polarized along the continuous nanowires (c,d), only the cavity modes are excited.

no plasmons can be excited and only the unperturbed cavity resonances are detected [Fig. 44(c,d)]. It has to be taken into account that a certain apparent length increase of the cavity occurs [29, 22], since the reflection phase shifts of the light on the metal layers is slightly larger than π . By comparing to simulations, this apparent length increase has been determined as $\delta_{\parallel} = 90$ nm for polarization along the nanowires. For polarization perpendicular to the nanowires, the phase shift upon reflection is different due to the additional

resonant plasmon excitation resulting in an apparent length increase of $\delta_{\perp} = 128$ nm. The relation between the first order resonance of the cavity λ_1 , the mirror distance d , and the apparent length increase δ is given by $\lambda_1 = 2(d + \delta)$.

6.2.4 MODE SPLITTING

In Fig. 45, the simulated and experimentally determined reflection spectra are plotted for two different cavity lengths $d_{SP} = 310$ nm and $d_{LP} = 395$ nm. At these distances, the resonance wavelength of the cavity corresponds to the surface plasmon and the localized plasmon resonances and the splitting energies can be directly observed. The reflectance spectra (red curves) correspond to cross-sections of Fig. 44 at the positions indicated by the black arrows. For comparison, the unperturbed plasmon resonances are plotted in the graphs as well (dashed gray curves). The simulated magnitudes of the splittings are 131 nm for the surface plasmon and 126 nm for the localized plasmon which correspond to splitting energies of 224 meV and 141 meV. Experimentally, slightly smaller splittings were measured: 122 nm for the localized plasmon and 119 nm for the surface plasmon resonance. These values are quite large and correspond to splitting/resonance energy ratios of about 1:10 indicating strong coupling.

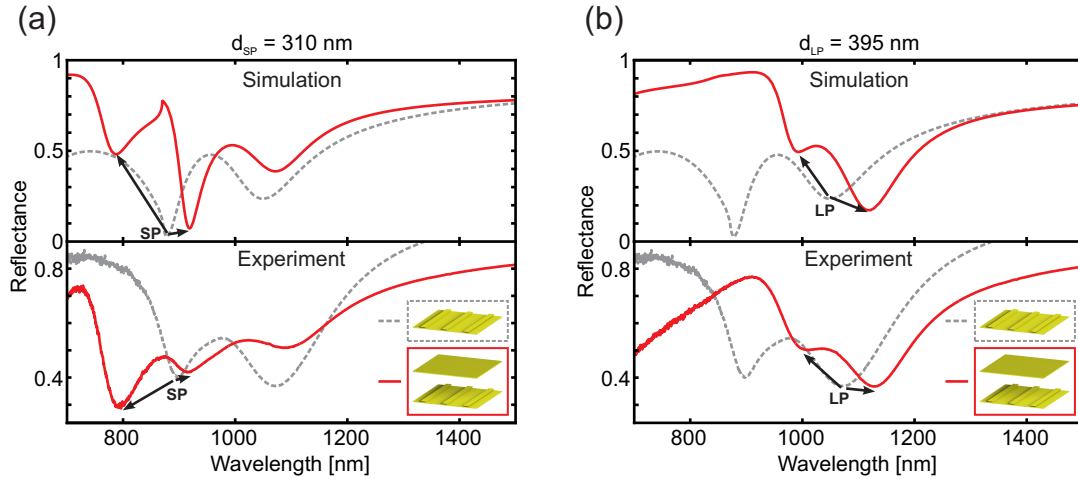


Figure 45: Simulated and measured reflectance spectra (red curves) at those cavity lengths where the resonance wavelength of the microcavity corresponds to the (a) surface plasmon (SP) and (b) localized plasmon (LP) resonances. The dashed gray curves in the background correspond to the unperturbed plasmon resonances of the structure without the second mirror.

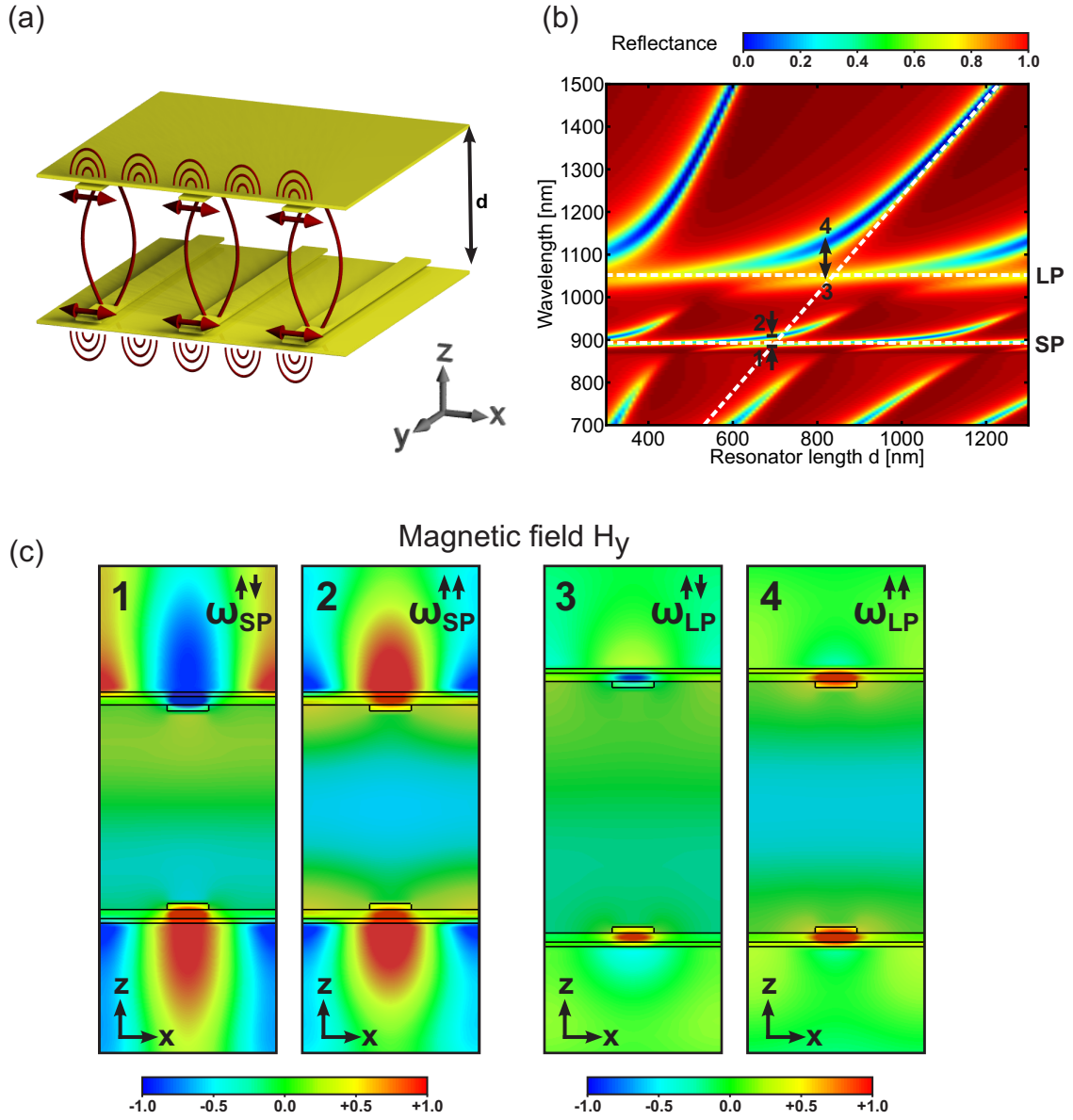


Figure 46: (a) Nanowires located close to both mirrors of the cavity allow surface and localized plasmon far-field coupling mediated by the cavity. (b) Reflectance plot for different cavity lengths d . The white dashed lines denote the unperturbed plasmon and cavity resonances. (c) Magnetic field plots of the split resonances at the positions (1-4) marked in the reflectance plot.

6.3 CAVITY-ASSISTED FAR-FIELD INTERACTIONS

Photonic cavity modes can mediate far-field coupling of emitters. This concept can also be applied to couple plasmons via the far-field [see Sec. 4.3]. By positioning a second layer of nanowires close to the second mirror of the cavity [Fig. 46(a)], a coupled photonic-plasmonic system is created which allows the interactions of the plasmons on one side of the cavity with the plasmons on the other side. The thickness of both mirrors is now 15 nm, all other parameters are the same as in the previous section. The coupling causes an additional splitting both of the surface plasmon and the localized plasmon modes. On the reflectance plot for different cavity lengths d [Fig. 46(b)], the additional splittings occur around the unperturbed plasmon modes each time when a cavity resonance frequency equals a plasmon resonance frequency. On the magnetic field plots [Fig. 46(c)], the nature of the different modes is revealed. The surface plasmon splits into a symmetric mode $\omega_{\text{SP}}^{\uparrow\uparrow}$ and an antisymmetric mode $\omega_{\text{SP}}^{\uparrow\downarrow}$ with the surface plasmons on the two sides of the cavity oscillating in phase or anti-phase. The same can be observed for the localized plasmons.

The symmetry of the electric field in the cavity determines which of the split plasmon modes exhibits the higher and which one the lower resonance frequency. For an interaction with the first cavity mode (and all subsequent odd cavity modes), the electric field points in the same direction for both sides of the cavity. Therefore, the localized plasmons on both sides of the cavity are preferably excited in phase inducing magnetic moments that point in opposite directions ($\omega_{\text{SP}}^{\uparrow\downarrow}$ and $\omega_{\text{LP}}^{\uparrow\downarrow}$). At a slightly higher frequency, the plasmons oscillate antiphase inducing magnetic moments pointing in the same direction ($\omega_{\text{SP}}^{\uparrow\uparrow}$ and $\omega_{\text{LP}}^{\uparrow\uparrow}$). For the second (and all subsequent even cavity modes), the situation is exactly inverted. The marked positions (1-4) in Figs. 46(b) and (c) belong to the second cavity mode, therefore the antisymmetric plasmon resonances $\omega_{\text{SP}}^{\uparrow\downarrow}$ and $\omega_{\text{LP}}^{\uparrow\downarrow}$ are located at lower wavelengths and the symmetric plasmon resonances $\omega_{\text{SP}}^{\uparrow\uparrow}$ and $\omega_{\text{LP}}^{\uparrow\uparrow}$ at higher wavelengths.

The values for the mode splitting in the simulations are 25 nm for the surface plasmon and 80 nm for the localized plasmon. These splittings are only observable when the damping parameter is reduced to the theoretical value. Therefore, an experimental realization of the far-field coupled plasmons could not yet be achieved.

7 CAVITY-ENHANCED PLASMONIC SENSING

7.1 INTRODUCTION

In this chapter, a method to enhance the sensing properties of a localized plasmon sensor using a microcavity is presented. At first, the general idea of localized plasmon resonance sensing is reviewed and different methods to characterize a sensor are presented. Subsequently, the new concept to enhance these kind of sensors is introduced. It is based on the combination of localized plasmons in nanostructures and a photonic microcavity. Metal nanorods that are placed near Bragg distance above a metal mirror form a Fabry-Pérot microcavity and constitute a coupled photonic-plasmonic system. The localized plasmon resonances of the nanorods and the phase shifts upon plasmon excitation are extremely sensitive to changes in the refractive index of the material surrounding the nanorods. Compared to the plasmonic nanorods alone, the coupled photonic-plasmonic system allows for a much more sensitive detection of small refractive index changes. The field distributions as well as the dependence on the unit cell size and the incident angle are analyzed. Finally, experimental results with water and glucose solutions that are channeled over a fabricated sample using a special sensing cell are presented.

7.2 LOCALIZED PLASMON RESONANCE SENSING

7.2.1 GENERAL PRINCIPLE

One of the most prominent features of plasmonic nanostructures in terms of practical applications is their use as localized surface plasmon resonance (LSPR) sensors [124, 51, 3]. The spectrum of sensing applications implies medical demands such as the detection of biomolecules [33, 57, 11, 125], safety-related concerns such as the measurement of gas concentrations [73, 82] as well as monitoring chemical reactions [53]. In all mentioned areas, the detection of small quantities preferably down to single molecules is desired. Therefore, all sensors have to be evaluated with respect to their sensitivity upon marginal changes of the environment. Localized plasmon resonances in metallic nanostructures have the potential to provide these properties [36].

The electric fields of the localized plasmons surround the nanostructures which associates the spectral position of the resonances to the refractive index of the environment

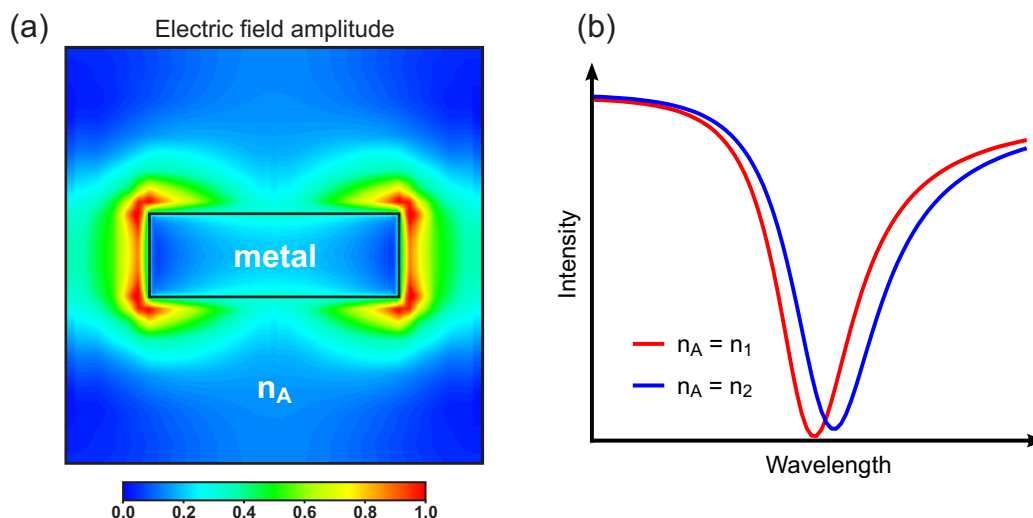


Figure 47: The principle of LSPR sensing: (a) the total time averaged electric fields of an excited plasmon in a nanostructure, here a nanorod, outreach the metal, therefore (b) the resonance frequency of a plasmonic nanostructure depends on the refractive index n_A of the surrounding medium.

[79, 6] [Fig. 47]. An increase in the refractive index n_A of the surrounding medium causes a redshift of the plasmon resonance [see also Fig. 12(e)]. These spectral shifts can be detected and give information about changes in the analyte. By a functionalization of the nanoparticle surfaces, the sensitivity can be extended from a mere detection of refractive index changes towards selective detection of a certain molecule concentration [34, 81].

Besides localized plasmon resonances, also propagating surface plasmon resonances can be used for sensing [40]. The obtained sensitivities are generally higher but due to the more difficult excitation of surface plasmon modes [see Sec. 2.3.2], these concepts require rather complex experimental setups.

7.2.2 STRUCTURE DEPENDENCE

The magnitude of the spectral shift is very dependent on the structure geometry. In Fig. 48 the plasmon resonance shifts of different geometric structures are compared¹³. The more symmetric a structure is, the smaller is the plasmon resonances shift. While nanospheres and nanocubes are among the least sensitive structures, more complex geometries like nanobipyramids and nanobranches exhibit very large shifts. At those complicated structures with rather sharp edges, the amount of electric field outside the nanostructure is much higher than for simple structures like nanospheres. The sensitivity of nanorods lies

¹³The data is taken from Chen et al. [13] and is based on measurements of gold nanoparticles of different shape and size in different concentrations of glycerol in water.

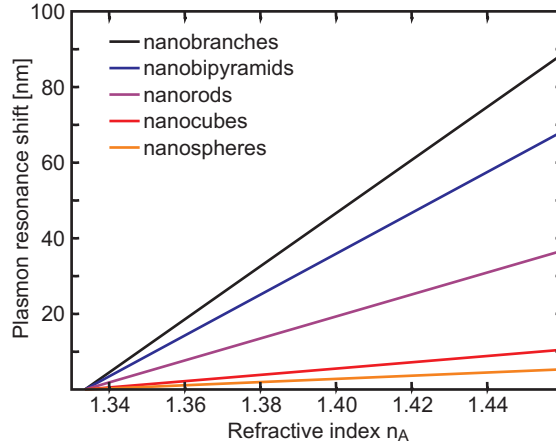


Figure 48: Dependence of the plasmon resonance shift on the particle shape [13].

between the complex and the very symmetric structures.

To demonstrate the concept of enhancing the sensitivity of a certain plasmonic nanostructure, we chose nanorods mainly due to their relatively easy fabrication using electron beam lithography. The aspect ratio (length divided by width) of a nanorod has a big influence on the sensitivity. The optimal aspect ratio for sensitive nanorods has been determined to be between 3 and 4 [6] which corresponds to the nanorods used in this thesis.

7.2.3 CHARACTERIZATION OF SENSING PROPERTIES

Comparing sensitive structures using only their sensitivity S defined as the plasmon resonance shift $\Delta\lambda$ divided by the refractive index change Δn is not always adequate. Depending on the regarded spectral region and on the detection methods, the sensitivity of a structure is not a sufficient measure to define its sensing properties. The absolute wavelength and the linewidth of the resonance are also crucial factors for a sensor. Therefore, a figure of merit FOM is defined [108] as the sensitivity S divided by the full width at half maximum $FWHM$ of a Lorentz-shaped resonance. Since the detection of the spectral shift of a resonance requires a spectrometer, a more practical way of detection that will be used in biosensors is the measurement of the reflected or transmitted light intensity for one particular wavelength [Fig. 49] using for example a laser diode. To take this into account, a new sensitivity usually referred to as S^* can be defined as the intensity variation ΔI for a given refractive index change Δn . Furthermore, the absolute intensity is a substantial factor because small intensity variations are much easier to detect when the overall intensity is already low. Therefore, a new figure of merit FOM^* is defined [6, 65] as the sensitivity S^* divided by the absolute intensity I . According to this, the various

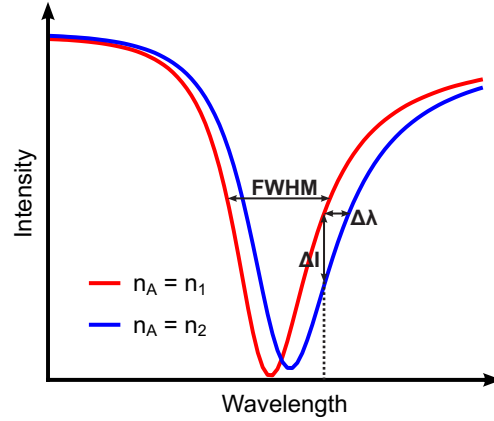


Figure 49: Spectral shifts $\Delta\lambda$ as well as the variations of the transmitted or reflected intensity ΔI can be detected.

definitions of the sensing capabilities of a given structure are specified as follows:

$$S = \frac{\Delta\lambda}{\Delta n} \quad (7.1)$$

$$S^* = \frac{\Delta I}{\Delta n} \quad (7.2)$$

$$FOM = \frac{S}{FWHM} \quad (7.3)$$

$$FOM^* = \frac{S^*}{I}. \quad (7.4)$$

In order to obtain high values for these parameters, it is required to have resonances that exhibit not only a large spectral shift but possess also a small linewidth and a large modulation depth.

7.3 CAVITY-ENHANCED SENSING

7.3.1 LINEWIDTHS AND SENSING PRINCIPLE

As pointed out in the previous section, the large linewidth of plasmon resonances is a major problem because it impairs the sensing properties fundamentally. A plasmon resonance of a nanorod in the near-infrared region, for example, has a linewidth of typically a few hundred nanometers resulting in a very low Q-factor. This is a big drawback because for any practical applications large intensity variations of the reflected or transmitted light at a certain wavelength are desired.

The reason for the large linewidth of plasmon resonances is the strong radiative damping of the metal [110]. An effective way of decreasing the linewidth is to couple the plasmon to a system with a narrow resonance. This concept has already been applied

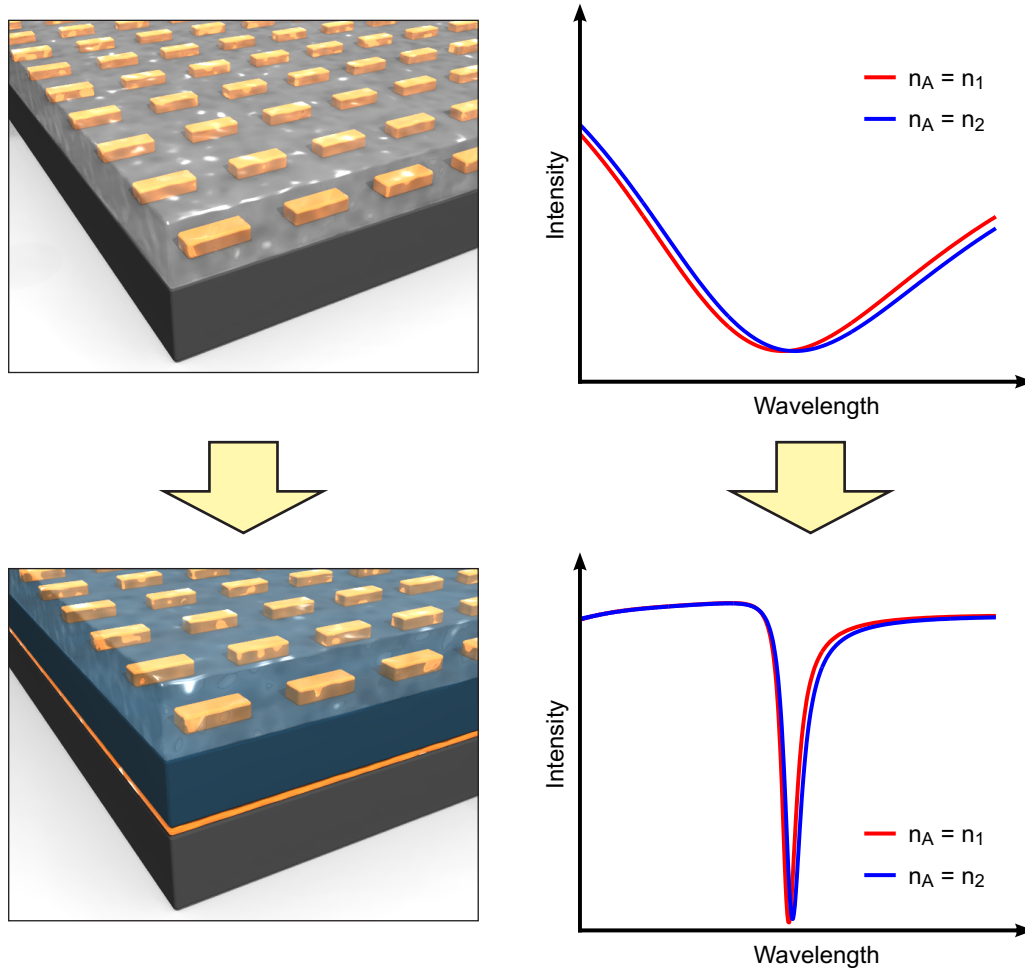


Figure 50: Decreasing the linewidth of a localized plasmon resonance by coupling to a photonic microcavity.

successfully in the context of the plasmonic analog of electromagnetically induced transparency (EIT) [63, 54] where a broad plasmonic dipole is coupled to a narrow plasmonic quadrupole resonance. The resulting structure exhibits sharp peaks and superior sensing properties.

In a similar way, the plasmonic resonances can be coupled to a photonic microcavity [4] [see also Ch. 5]. Here, the linewidth of the coupled photonic-plasmonic resonance arises from the *cavity* Q-factor due to the modified photonic density of states and hence the modified radiative damping rate. As a result, the idea of a combination of plasmonic nanostructures with a Fabry-Pérot microcavity provides a way of decreasing the linewidth of the resonances and therefore improving the sensing properties of nanostructures [Fig. 50].

7.3.2 PHASE SHIFTS

The sensitivity of the coupled photonic-plasmonic structure arises from a strong phase dependence of the localized plasmon excitation in the nanorods [Fig. 51] which can be explained with a simple effective medium model accounting for the phase shifts. In analogy to Secs. 2.3.1 and 4.3.2, the total phase shift that a wave accumulates during one round trip in the cavity is the sum of the phase shifts due to the propagation of the wave through the cavity $\Delta\varphi_{\text{prop}}$, the phase shifts upon reflection at the cavity mirrors $\Delta\varphi_{\text{refl}}$, and the phase shifts that occur on plasmon excitation $\Delta\varphi_{\text{exc}}$. The resonance condition for the cavity sensing structure is then given by

$$\Delta\varphi_{\text{tot}} = 2\Delta\varphi_{\text{prop}} + \Delta\varphi_{\text{refl}} + \Delta\varphi_{\text{exc}} = (N + 1) \cdot 2\pi. \quad (7.5)$$

This leads to the expression

$$\lambda_N = \frac{2n_{\text{cav}}d}{(N + 1) - \frac{1}{2\pi}(\Delta\varphi_{\text{refl}} + \Delta\varphi_{\text{exc}}(n_A))} \quad (7.6)$$

for the resonance wavelengths λ_N of the whole system with n_{cav} being the refractive index of the material in the cavity and d the distance between the mirror and the nanorod array. The phase shift upon reflection at the mirror $\Delta\varphi_{\text{refl}}$ can be calculated using Eq. 2.17. The plasmon excitation phase shift $\Delta\varphi_{\text{exc}}$ is dependent on the refractive index of the analyte n_A and can be calculated using the driven harmonic oscillator model with the assignment

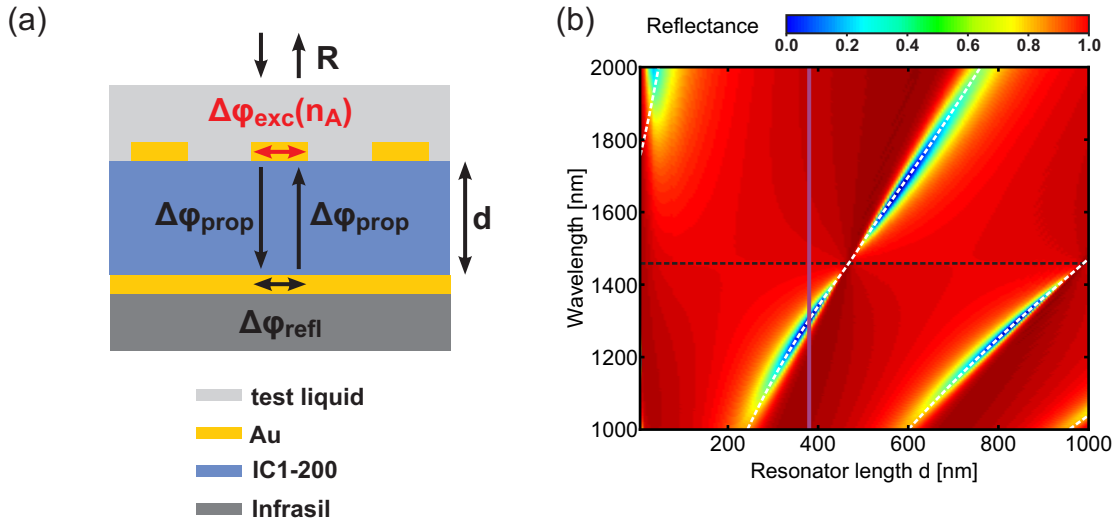


Figure 51: Nanorods combined with a cavity: (a) Phase shifts and (b) reflectance plot for different wavelengths and distances. The vertical violet line represents the fabricated sample, the dashed white lines denote the calculated resonances using Eq. 7.6, the dashed black line is the unperturbed localized plasmon resonance of the nanorods.

of an effective permittivity to the nanostructured layer [Sec. 4.3.2] using Eq. 4.9 with the corresponding refractive indices for the analyte n_A and the cavity n_{cav} .

This way, the phase shifts become dependent on the refractive index n_A of the material surrounding the nanostructure. A change in this refractive index causes a shift of the localized plasmon resonance wavelength λ_{LP} of the nanorod. Therefore, the phase shift upon plasmon excitation $\Delta\phi_{exc}$ is changed. As a result, the total phase shift is changed and the resonance condition [Eq. 7.5] for the cavity is no longer fulfilled for the same wavelength. Due to the small linewidth, a slight spectral shift of the resonance causes a large intensity variation ΔI . The reflected light intensity at the former minimum is therefore now substantially different from zero. This results in large values of the sensitivity S^* and the figure of merit [Sec. 7.4.4] when the nanorods are placed at around Bragg distance to the mirror [Sec. 7.3.3]. The calculated resonances using Eq. 7.6 agree very well with the simulated reflectance plot in Fig. 51(b).

7.3.3 OPTIMAL SENSING STRUCTURE PARAMETERS

The largest changes in $\Delta\phi_{exc}$ can be obtained when the resonance of the coupled system [white dashed line in Fig. 51(b)] is close to the plasmon resonance of the nanorod [black dashed line in Fig. 51(b)]. However, exactly at the plasmon resonance the reflected light intensity is equal to 1 since no light is transmitted by the nanorods array under this condition. Therefore, no resonance can be observed here. The ideal wavelength for sensing is about 10% above or below the plasmon resonance wavelength.

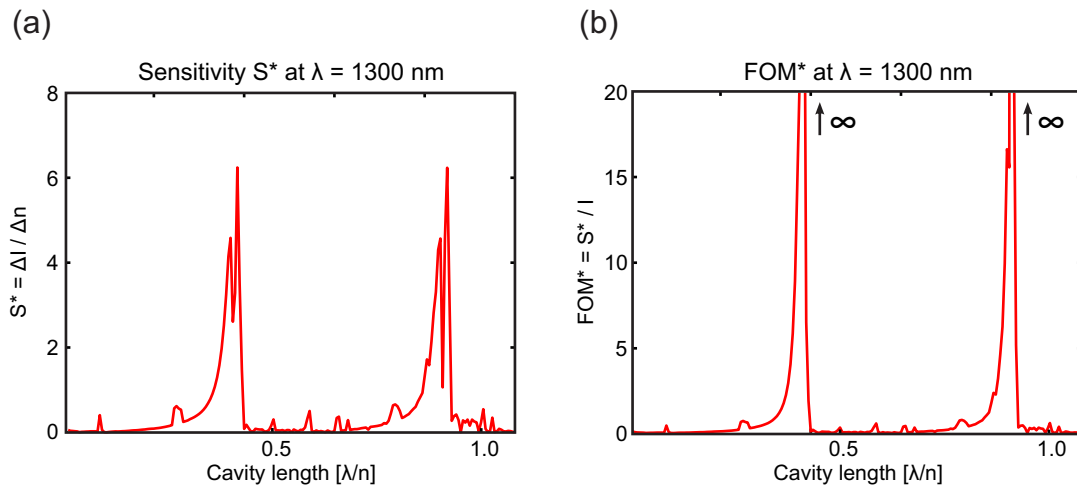


Figure 52: Sensitivity S^* and figure of merit FOM^* calculated from simulations for materials with refractive indices $n_1 = 1.33$ and $n_2 = 1.37$ surrounding the nanorods. The values are enhanced when the nanorods are placed around Bragg distance to the mirror.

The distance of the nanorods to the mirror then has to be near Bragg distance ($d_{\text{Bragg}} = \frac{N\lambda}{2}$). Under these conditions, the largest enhancement of the sensitivity S^* and the figure of merit FOM^* can be observed [Fig. 52]. The actual deviations from the exact Bragg distance are due to reflection phase shifts at the mirror and at the nanorod layer that are not equal to π . Applying Eq. 7.6 leads for the regarded wavelength of $\lambda = 1300$ nm to a matching resonator length of $d = 380$ nm which agrees very well with the experiments [see Sec. 7.4.4]. The highest observed value for the sensitivity S^* is 6.1. Zero reflectance in simulations [see Fig. 58(a)] leads to an infinite FOM^* for the resonance wavelength.

For the simulations, nanorods with a length of 380 nm, a width of 100 nm, and a thickness of 70 nm were used. The unit cell size is $500 \text{ nm} \times 500 \text{ nm}$, the thickness of the mirror is 40 nm. The refractive indices of the substrate, the spacer and the analyte are $n_{\text{sub}} = 1.45$, $n_{\text{IC1}} = 1.40$, and $n_{\text{H}_2\text{O}} = 1.33$, respectively. For gold, the quasi-free electron model with the parameters from Sec. 2.2.2 was applied.

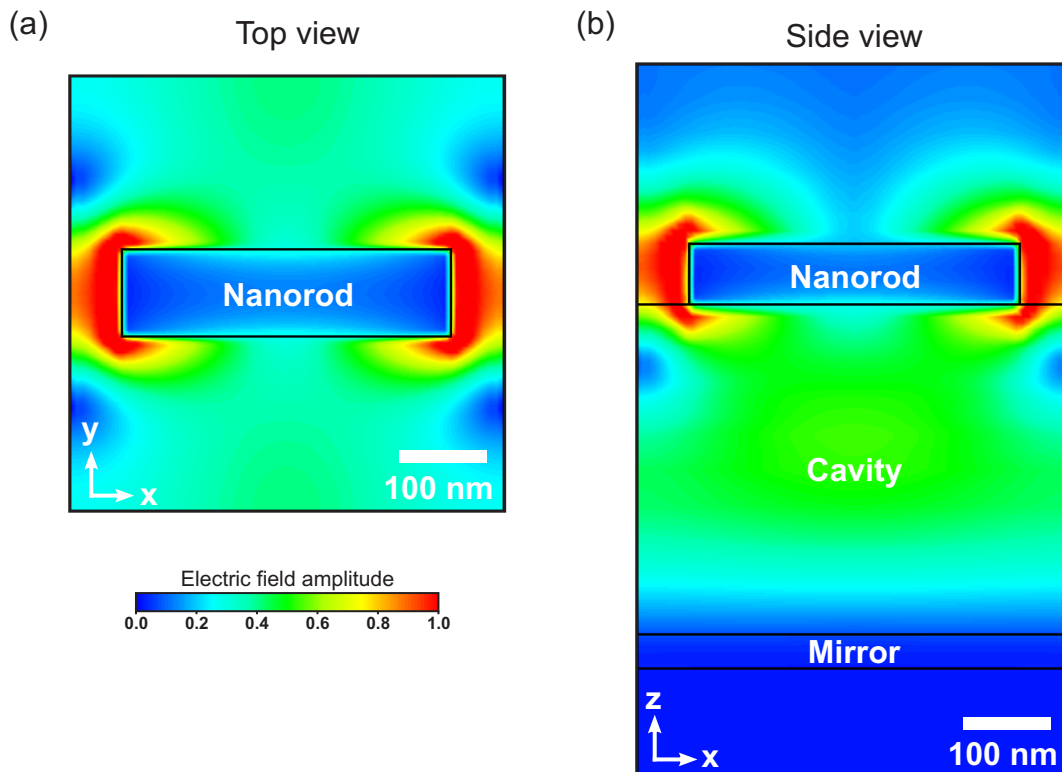


Figure 53: Distribution of the time-averaged total electric field in the sensor structure. The (a) top view and (b) side view of a unit cell reveal the strong field localization at the nanorod ends and in the cavity. Structure parameters are the same as defined in Sec. 7.3.3.

7.3.4 FIELD LOCALIZATION

The field distributions in Fig. 53 for a cavity length of $d = 380$ nm point out the concentration of the electric fields at the nanorod ends and inside the cavity at the resonance wavelength of $\lambda = 1300$ nm. Due to the strong field localization between the nanorods, the sensing volume is very small. Only where the electric fields outreach the structure, a change in the environment can have an influence on the plasmon resonance. A functionalization of the nanorod ends can make the localized sensor selective for only a certain kind of molecules which is favorable for biochemical or medical applications. Additionally, the field localization inside the cavity might be utilized for sensing which would further increase the structure's sensitivity. This could be achieved by using porous media or by placing the nanorods on pillars. Further improvements include a combination of the cavity structure with micro- and nanofluidic techniques [41, 125].

7.3.5 UNIT CELL SIZE AND INCIDENT ANGLE

In this section, the effects of changing the lateral distance between the nanorods and of changing the angle of the incident light are investigated. In Fig. 54, the periods in x - and y -direction p_x and p_y are varied and the reflectance for each period is plotted around the resonance of the combined cavity-nanorod structure.

Changing p_x does not affect the resonance of the system unless the distance between two nanorods is less than about 120 nm which means in this case a period in x -direction smaller than 500 nm. However, the system's resonance is very dependent on the period in y -direction. By enhancing p_y from 200 nm to 700 nm, the resonance wavelength is shifted from 1160 nm to 1420 nm. This behavior can be explained by regarding the dipole emission patterns of the nanorods [see Sec. 4.2.1]. In oscillation direction (x -direction) almost no radiation is emitted which means that an interaction to neighboring nanorods can only take place via the near-field. Most radiation is emitted perpendicular to the nanorod (in y -direction). In resemblance to cavities consisting of nanorods [Sec. 4.3.3], the resonance wavelength is very dependent on the nanorod distance. Although the variations in the resonances are quite remarkable, the principle of the sensor remains valid also for large unit cells. Therefore, in principle only one element can be used for the detection of very small quanta which, in combination with the strong field localization, justifies the designation as localized sensor.

The dependence of the resonances on the incident angle of light θ is plotted in Fig. 55. For incident angles of less than 10° , no changes can be observed. For larger incident angles, the resonances are shifted towards lower wavelengths until the system breaks down at around $\theta = 40^\circ$ and other effects like Rayleigh-Wood anomalies dominate the behavior of the sensor. The large independence on the incident angle is useful for many possible applications.

For the simulations, the same structure parameters as in Sec. 7.3.3 are used.

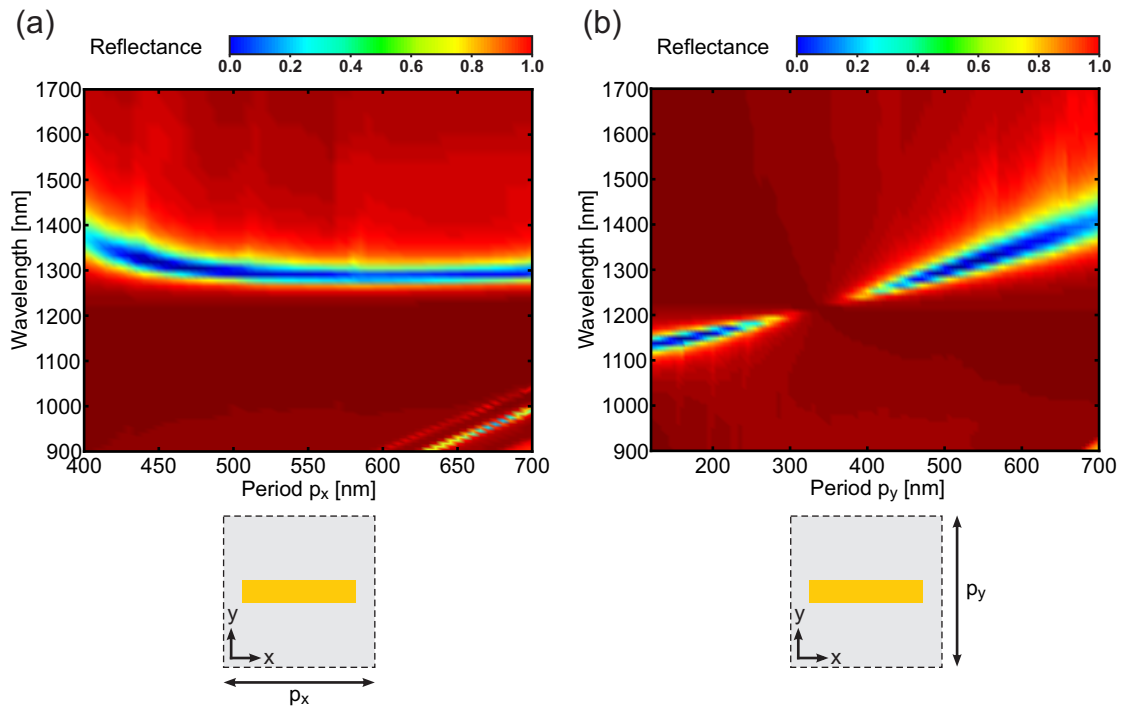


Figure 54: Reflectance plots of the combined cavity-nanorod structure for different periods in (a) x -direction and (b) y -direction.

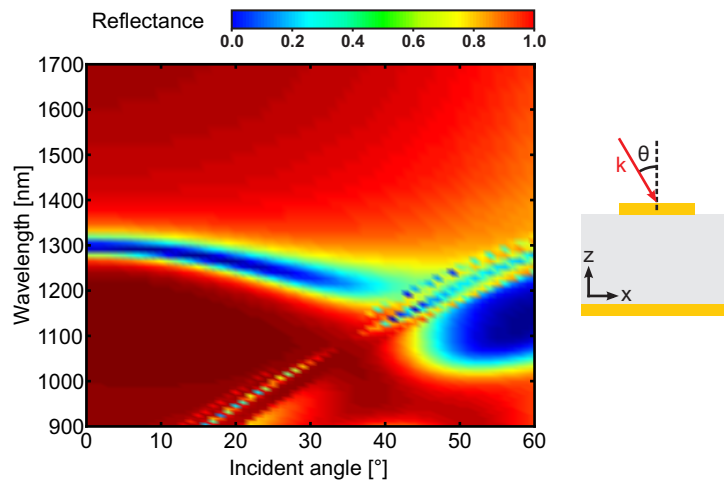


Figure 55: Reflectance plots of the combined cavity-nanorod structure for different incident angles θ .

7.4 EXPERIMENTAL RESULTS

7.4.1 SAMPLE FABRICATION

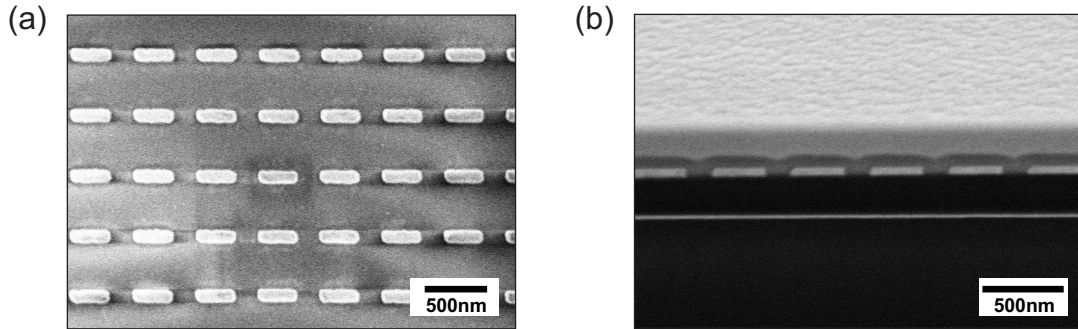


Figure 56: (a) Top view and (b) side view of the cavity sensing structure. For the side view, a hole was cut in the structure using a focussed ion beam. A protection layer had to be evaporated for the cut which is visible above the nanorods.

The sample was fabricated using thermal evaporation for the gold layers, spin-coating for the dielectric spacer, and electron-beam lithography for the nanostructuring. The thickness of the lower gold layer is 40 nm. The material of the dielectric spacer is the polysiloxane-based spin-on glass IC1-200 with a refractive index of $n_{IC1} = 1.40$ and a layer thickness of 380 nm. The nanorods have a thickness of 70 nm, a length of 380 nm, and a width of 100 nm. The unit cell size of the nanorod array is $500 \text{ nm} \times 500 \text{ nm}$ which is well below the distance where Rayleigh- or Wood-anomalies cause problems [16]. The total size of the nanorod array is $100 \mu\text{m} \times 100 \mu\text{m}$. Fig. 56 shows SEM images providing a top and a side view on the structure. For comparative measurements, the same nanorod array was also fabricated without the cavity directly on a glass substrate.

7.4.2 EXPERIMENTAL SETUP

The method of enhancing the sensitivity S^* and the figures of merit FOM and FOM^* of a plasmonic sensor was experimentally demonstrated using water and glucose solutions. Using a microfluidic sensing cell [66, 74] attached to a number of syringes, the different liquids were channeled over the sample. The cell [Fig. 57] consists of a metallic sample substrate holder and two layers made of PDMS (polydimethylsiloxane) and polycarbonate directing the liquids from the fluid connectors to the sample surface via $80 \mu\text{m}$ thin channels. The spectra were measured at opening angles from 10° to 24° with the FTIR-spectrometer and an attached infrared microscope [see Sec. 3.5].

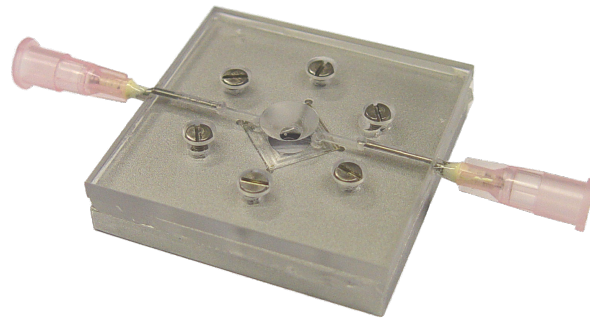


Figure 57: The microfluidic sensing cell [74].

7.4.3 MEASURED SPECTRA

In Fig. 58, the simulated and experimental spectra for both bare nanorods and nanorods combined with the cavity are compared. The shifts of the resonances for the nanorods surrounded by water ($n_1 = 1.3198$ [8]) and by a 25%-solution of glucose in water ($n_2 = 1.3594$ [127]) can be observed. The refractive index change is hence $\Delta n = n_2 - n_1 = 0.0396$. The refractive indices of the liquids are taken at a wavelength of 1300 nm. The decrease of the resonance linewidth when the cavity is added to the nanorods is very distinct. The linewidth of the peak decreases drastically from 900 nm to 50 nm in simulation and from 600 nm to 90 nm in experiment. In order to accurately compare both structures, the configuration with the best FOM^* was used, which is the detection of transmittance for the nanorods alone and the detection of reflectance for the nanorods combined with the cavity.

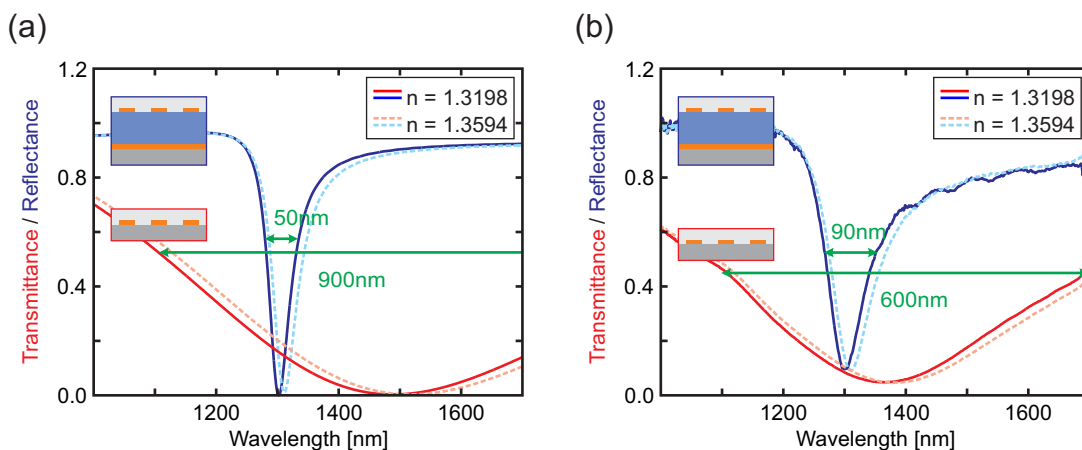


Figure 58: (a) Simulated and (b) experimental spectra of bare nanorods (red curves) compared to nanorods combined with a cavity (blue curves) for liquids with two different refractive indices surrounding the nanorods.

7.4.4 SENSITIVITY AND FIGURE OF MERIT

From the spectra and the refractive index difference, the sensitivities and figures of merit [Eqs. 7.1 to 7.4] can be calculated. The values for the calculated sensitivity S and figure of merit FOM as well as the maximum values for the sensitivity S^* and the figure of merit FOM^* are summed up in Tab. 4 both for simulated and measured data from nanorods alone and from nanorods combined with a cavity.

It turns out that the sensitivity $S = \Delta\lambda/\Delta n$ actually decreases by a factor of 2.5 in simulations and 2.3 in experiments when the cavity is added to the nanorods. This is likely due to the fact that the mode volume increases due to the cavity. Nevertheless, since the linewidth of the peak decreases drastically, the figure of merit $FOM = S/FWHM$ increases by a factor of 7.1 in simulations and by a factor of 3.1 in the experimental measurement. The small linewidth has also a large effect on the sensitivity S^* since a small shift causes a high variation in the reflected intensity. The observed increase for the maximum sensitivity S_{\max}^* is 5.5 in simulation and 3.7 in experiment. At the minimum, the fraction of the reflected light intensity is only 9%, resulting in an enhancement factor of 3.5 for the measured figure of merit FOM^* . In the simulations, zero reflected intensity at the resonance of the cavity results in a theoretically infinite value for FOM^* . The dependence of S^* and FOM^* on the wavelength is plotted in Fig. 59. The shape of the curves of S^* and FOM^* (two close maxima and a minimum in between with a kink at 0)

Structure	Nanorods alone	Nanorods + Cavity	Enhancement factor
$\Delta\lambda$	35 nm (27 nm)	14 nm (12 nm)	0.4 (0.4)
S	884 nm/RIU (682 nm/RIU)	354 nm/RIU (303 nm/RIU)	0.4 (0.4)
FOM	1.0 (1.1)	7.1 (3.4)	7.1 (3.1)
S_{\max}^*	1.1 (0.9)	6.1 (3.3)	5.5 (3.7)
FOM_{\max}^*	47 (5.9)	$\rightarrow \infty$ (20.8)	$\rightarrow \infty$ (3.5)

Table 4: Summary of the determined sensitivities and figures of merit. The values in brackets denote the experimental values.

originates from the fact that $\Delta I = 0$ where the curves for the two different liquids intersect, whereas close by, the slope increases (\Rightarrow large S^*) and the absolute intensity is still very low (\Rightarrow large FOM^*). The deviations between simulated and experimental values are most likely due to fabrication imperfections and non-normal light incidence.

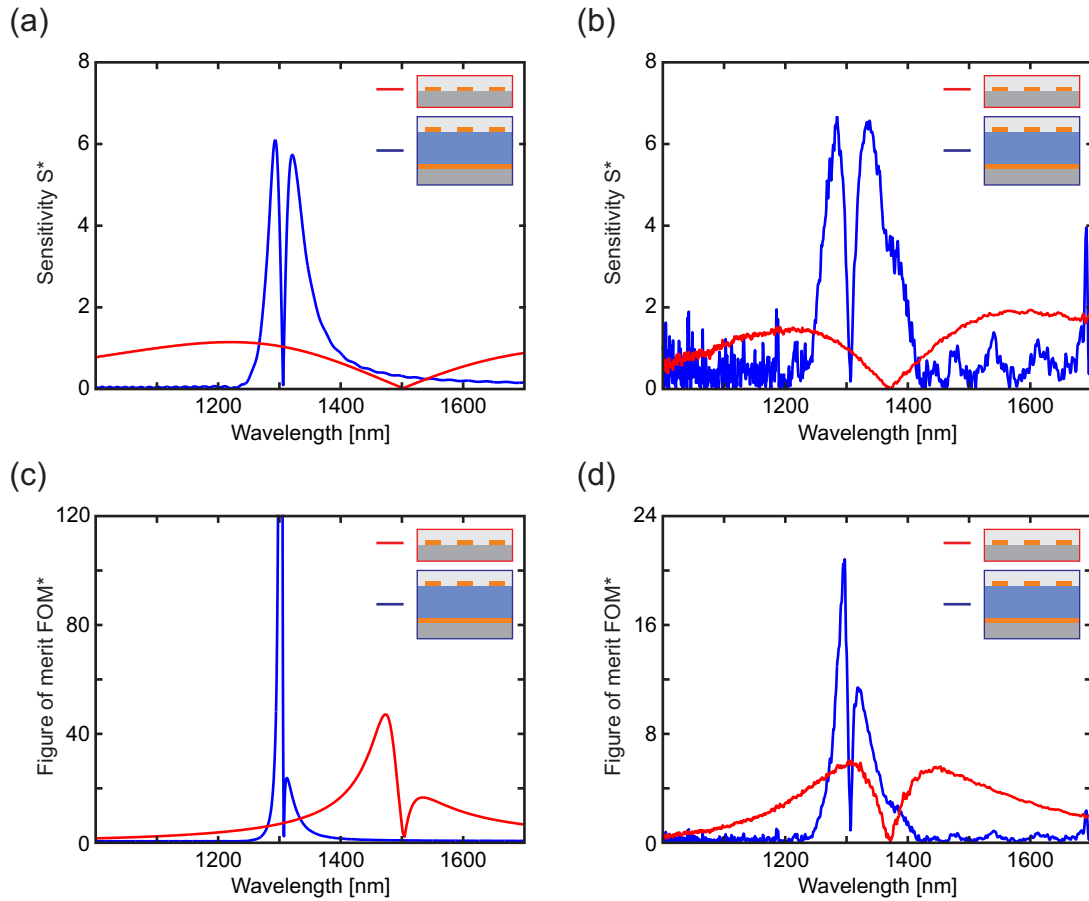


Figure 59: (a, b) Sensitivity S^* and (c, d) figure of merit FOM^* for different wavelengths determined from the (a, c) simulated and (b, d) measured spectra. Red curves correspond to nanorods alone, blue curves to nanorods combined with a cavity.

8 CONCLUSIONS

8.1 SUMMARY

This thesis provided an investigation of the plasmon-plasmon as well as the light-plasmon coupling strength and range in multilayer nanostructures and demonstrated the manipulation of the plasmon resonances by modifying the environment using microcavities. Different models, such as the dipole model, image charges and plasmon hybridization as well as a consideration of phase shifts and the assignment of effective resonant permittivities were used to explain the observed behavior of near- and far-field coupled nanostructures.

In analogy to the strong coupling of atoms or quantum dots to photonic cavity modes, it was demonstrated that also localized plasmons and propagating surface plasmons can be coupled strongly to light. In particular, it was shown that either the symmetric (electric) or the antisymmetric (magnetic) hybridized plasmon modes of nanorod pairs can exhibit strong coupling to standing waves in a microcavity depending on the position of the nanostructure in the cavity. The behavior is explained by the direction of the electric field vectors of the resonator modes at the positions of the nanorods. The splitting can be as large as 82 meV for the magnetic and 354 meV for the electric mode which is very large, as the splitting is 36% of the resonance energy. The experimentally observed splitting-to-linewidth ratio can be as large as 10 for the symmetric (electric) mode and 2.5 for the antisymmetric (magnetic) plasmon mode. Especially the coupling strength to the magnetic dipole of the antisymmetric mode is remarkable since magnetic moments usually can not be addressed easily.

The concept was extended from localized plasmons to propagating surface plasmons. Surface plasmons can only be excited under certain conditions that can be met by placing an array of continuous nanowires close to a mirror. The creation of a microcavity by positioning a second mirror at an appropriate distance allowed the strong coupling of the photonic cavity modes to the surface plasmons. The measured splitting energies were in the range of 10% of the resonance energy. It was shown that the cavity modes can also mediate a coupling of localized and surface plasmons via far-field distances.

The excellent agreement between the simulations and the measured spectra of the various fabricated samples required accurate and versatile fabrication procedures for the multilayer nanostructures. It was demonstrated that different thin layer and nanostructure fabrication techniques can be combined to produce the functional nanostructures

in a layer-by-layer fashion. A combination of spin-on glasses and evaporated dielectric materials was used to produce spacer layers of a wide range of thicknesses with well-defined parameters. Furthermore, it was shown that the very simple technique of applying mechanical pressure on two substrates is suitable for the construction of microcavities with a variable resonator length ranging from several micrometers to only a few hundred nanometers.

The acquired knowledge of the coupling mechanisms and fabrication procedures of the considered structures was used to design a structure for a practical application. A method to enhance the sensing properties of a localized plasmon sensor was investigated theoretically and experimentally. It was shown that the technique of adding a mirror at an appropriate distance to a sensitive nanostructure and thereby creating a cavity, can considerably increase the sensitivity due to an extremely decreased linewidth of the coupled plasmonic-photonic resonance. The values characterizing the properties of an LSPR sensor could be increased by a factor of more than 3 in the experiments. Furthermore, an overview of different parameters to characterize a sensor was given since the assignment of a mere sensitivity defined as the resonance shift per refractive index unit change is not sufficient to fully describe and compare sensors.

8.2 OUTLOOK

In general, the concepts can be further expanded to multiple cavities or multiple elements at Bragg- or anti-Bragg spacing. At the end of Chs. 4 and 5, the properties of multilayer stacks were briefly examined. The investigation of plasmon far-field coupling mechanisms are important in the context of three-dimensional novel materials with unconven-

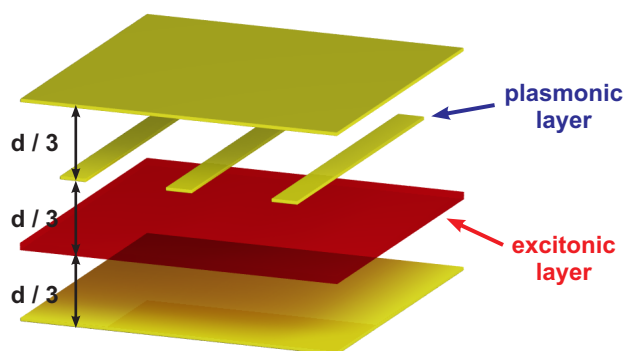


Figure 60: Microcavities can be used to couple excitons and plasmons via the far-field. Excitonic resonances can be excited for example in a layer of quantum dots or J-aggregates.

tional optical properties (3D-metamaterials) consisting of many nanostructured layers. An increase in coupling strength and range can facilitate the production and improve the functionality of these materials. Also, the indication of band gap formation in Bragg-spaced multilayer nanostructures already at a very small number of layers can be used for functional layers with tailored transmission and reflection properties that are applicable as nanoscale filters or absorbers for example in integrated optics.

Even more intriguing is the coupling to quantum emitters, such as J-aggregates or semiconductor quantum dots [Fig. 60], which can be spaced a Bragg distance away from the metal. J-aggregates are coupled dye molecules exhibiting sharp excitonic resonances [105, 45, 78]. The far-field coupling of excitons and plasmons in microcavities avoids near-field quenching and should result in strongly coupled plasmon/exciton states (= plexcitons [30]).

The highlighted sensing applications of strongly coupled plasmonic and photonic modes in Ch. 7 can be further improved in a number of ways: At first, the cavity volume can be included for the sensing by different methods such as using porous media in the cavity, placing the nanostructures on pillars by drilling or etching holes or channels in the cavity or using microfluidic techniques. Second, a functionalization of the nanostructures can specialize the sensor and make it sensitive for certain kind of substances. Furthermore, the concept can be applied to many LSPR sensor structures superior to nanorods [13, 2] (e.g. colloidal systems such as nanostars [Fig. 61]) and will considerably improve their sensing properties. In general, the coupling in microcavities might be further increased by using dielectric mirrors resulting in high-Q cavities. Potential applications of LSPR sensing in the fields of biotechnology, medical diagnostics, or pharmacology including biomolecule detection as well as real-time monitoring of chemical reactions or molecular kinetics might benefit from this concept.

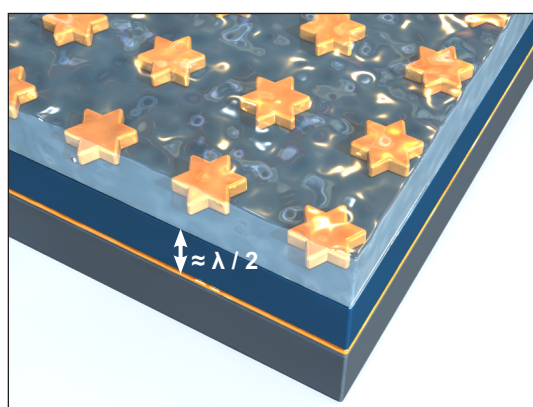


Figure 61: All kinds of geometries of sensitive nanostructures, such as nanostars, can be combined with a microcavity to enhance their sensing properties.

REFERENCES

- [1] A. ALÙ and N. ENGHETA. *Wireless at the Nanoscale: Optical Interconnects using Matched Nanoantennas*. *Physical Review Letters* **104**, 213902 (2010).
- [2] R. ALVAREZ-PUEBLA, L. M. LIZ-MARZÁN and F. J. GARCÍA DE ABAJO. *Light Concentration at the Nanometer Scale*. *The Journal of Physical Chemistry Letters* **1**, 2428 (2010).
- [3] J. N. ANKER, W. P. HALL, O. LYANDRES, N. C. SHAH, J. ZHAO and R. P. VAN DUYNE. *Biosensing with plasmonic nanosensors*. *Nature Materials* **7**, 442 (2008).
- [4] A. ARTAR, A. A. YANIK and H. ALTUG. *Fabry-Pérot nanocavities in multilayered plasmonic crystals for enhanced biosensing*. *Applied Physics Letters* **95**, 051105 (2009).
- [5] M. BARTH, S. SCHIETINGER, S. FISCHER, J. BECKER, N. NÜSSE, T. AICHELE, B. LÖCHEL, C. SÖNNICHSEN and O. BENSON. *Nanoassembled Plasmonic-Photonic Hybrid Cavity for Tailored Light-Matter Coupling*. *Nano Letters* **10**, 891 (2010).
- [6] J. BECKER, A. TRÜGLER, A. JAKAB, U. HOHENESTER and C. SÖNNICHSEN. *The Optimal Aspect Ratio of Gold Nanorods for Plasmonic Bio-sensing*. *Plasmonics* **5**, 161 (2010).
- [7] D. BERGMAN and M. STOCKMAN. *Surface Plasmon Amplification by Stimulated Emission of Radiation: Quantum Generation of Coherent Surface Plasmons in Nanosystems*. *Physical Review Letters* **90**, 027402 (2003).
- [8] J. E. BERTIE and Z. LAN. *Infrared Intensities of Liquids XX: The Intensity of the OH Stretching Band of Liquid Water Revisited, and the Best Current Values of the Optical Constants of H₂O(l) at 25°C between 15,000 and 1 cm⁻¹*. *Applied Spectroscopy* **50**, 1047 (1996).
- [9] A. BOCA, R. MILLER, K. M. BIRNBAUM, A. D. BOOZER, J. MCKEEVER and H. J. KIMBLE. *Observation of the Vacuum Rabi Spectrum for One Trapped Atom*. *Physical Review Letters* **93**, 233603 (2004).
- [10] C. F. BOHREN and D. R. HUFFMANN. *Absorption and Scattering of Light by Small Particles*. Wiley (1983).
- [11] K. M. BYUN. *Development of Nanostructured Plasmonic Substrates for Enhanced Optical Biosensing*. *Journal of the Optical Society of Korea* **14**, 65 (2010).
- [12] J. CESARIO, R. QUIDANT, G. BADENES and S. ENOCH. *Electromagnetic coupling between a metal nanoparticle grating and a metallic surface*. *Optics Letters* **30**, 3404 (2005).

- [13] H. CHEN, X. KOU, Z. YANG, W. NI and J. WANG. *Shape- and Size-Dependent Refractive Index Sensitivity of Gold Nanoparticles*. Langmuir : the ACS Journal of Surfaces and Colloids **24**, 5233 (2008).
- [14] A. CHRIST, Y. EKINCI, H. SOLAK, N. GIPPIUS, S. TIKHODEEV and O. MARTIN. *Controlling the Fano interference in a plasmonic lattice*. Physical Review B **76**, 201405(R) (2007).
- [15] A. CHRIST, O. J. F. MARTIN, Y. EKINCI, N. A. GIPPIUS and S. G. TIKHODEEV. *Symmetry breaking in a plasmonic metamaterial at optical wavelength*. Nano Letters **8**, 2171 (2008).
- [16] A. CHRIST, T. ZENTGRAF, J. KUHL, S. G. TIKHODEEV, N. A. GIPPIUS and H. GIESSEN. *Optical properties of planar metallic photonic crystal structures: Experiment and theory*. Physical Review B **70**, 125113 (2004).
- [17] A. CHRIST, T. ZENTGRAF, S. G. TIKHODEEV, N. A. GIPPIUS, J. KUHL and H. GIESSEN. *Controlling the interaction between localized and delocalized surface plasmon modes: Experiment and numerical calculations*. Physical Review B **74**, 155435 (2006).
- [18] P. DEBACKERE, P. BIENSTMAN and R. BAETS. *Adaptive spatial resolution: application to surface plasmon waveguide modes*. Optical and Quantum Electronics **38**, 857 (2006).
- [19] J. DINTINGER, S. KLEIN, F. BUSTOS, W. L. BARNES and T. W. EBBESEN. *Strong coupling between surface plasmon-polaritons and organic molecules in subwavelength hole arrays*. Physical Review B **71**, 035424 (2005).
- [20] G. DOLLING, C. ENKRICH, M. WEGENER, C. M. SOUKOULIS and S. LINDEN. *Simultaneous Negative Phase and Group Velocity of Light in a Metamaterial*. Science **312**, 892 (2006).
- [21] G. DOLLING, C. ENKRICH, M. WEGENER, J. F. ZHOU, C. M. SOUKOULIS and S. LINDEN. *Cut-wire pairs and plate pairs as magnetic atoms for optical metamaterials*. Optics Letters **30**, 3198 (2005).
- [22] J. DORFMÜLLER, R. VOGELGESANG, R. T. WEITZ, C. ROCKSTUHL, C. ETRICH, T. PERTSCH, F. LEDERER and K. KERN. *Fabry-Pérot Resonances in One-Dimensional Plasmonic Nanostructures*. Nano Letters **9**, 2372 (2009).
- [23] D. DREGELY, R. TAUBERT, J. DORFMÜLLER, R. VOGELGESANG, K. KERN and H. GIESSEN. *3D optical Yagi-Uda nanoantenna-array*. Nature Communications (in press) (2011).
- [24] K. H. DREXHAGE. *Interaction of light with monomolecular dye layers*. Progress in Optics **12**, 163 (1974).
- [25] P. DRUDE. *Zur Elektronentheorie der Metalle*. Annalen der Physik **306**, 566 (1900).
- [26] C. ENKRICH, M. WEGENER, S. LINDEN, S. BURGER, L. ZSCHIEDRICH, F. SCHMIDT, J. ZHOU, T. KOSCHNY and C. SOUKOULIS. *Magnetic Metamaterials at Telecommunication and Visible Frequencies*. Physical Review Letters **95**, 203901 (2005).

-
- [27] T. ERGIN, N. STENGER, P. BRENNER, J. B. PENDRY and M. WEGENER. *Three-dimensional invisibility cloak at optical wavelengths*. *Science* **328**, 337 (2010).
- [28] M. FARADAY. *The Bakerian Lecture: Experimental Relations of Gold (and other Metals) to Light*. *Philosophical Transactions of the Royal Society of London* **147**, 145 (1857).
- [29] E. FEIGENBAUM and M. ORENSTEIN. *Ultrasmall Volume Plasmons, yet with Complete Retardation Effects*. *Physical Review Letters* **101**, 163902 (2008).
- [30] N. T. FOFANG, T.-H. PARK, O. NEUMANN, N. A. MIRIN, P. NORDLANDER and N. J. HALAS. *Plexcitonic Nanoparticles: Plasmon-Exciton Coupling in Nanoshell-J-Aggregate Complexes*. *Nano Letters* **8**, 3481 (2008).
- [31] M. GOLOSOVSKY, Y. NEVE-OZ, D. DAVIDOV and A. FRENKEL. *Phase shift on reflection from metallodielectric photonic bandgap materials*. *Physical Review B* **70**, 115105 (2004).
- [32] G. GRANET. *Reformulation of the lamellar grating problem through the concept of adaptive spatial resolution*. *Journal of the Optical Society of America A* **16**, 2510 (1999).
- [33] A. J. HAES, L. CHANG, W. L. KLEIN and R. P. VAN DUYN. *Detection of a Biomarker for Alzheimer's Disease from Synthetic and Clinical Samples Using a Nanoscale Optical Biosensor*. *Journal of the American Chemical Society* **127**, 2264 (2005).
- [34] A. J. HAES and R. P. VAN DUYN. *A Nanoscale Optical Biosensor: Sensitivity and Selectivity of an Approach Based on the Localized Surface Plasmon Resonance Spectroscopy of Triangular Silver nanoparticles*. *Journal of the American Chemical Society* **124**, 10596 (2002).
- [35] T. K. HAKALA, J. J. TOPPARI, A. KUZYK, M. PETTERSSON, H. TIKKANEN, H. KUNTTU and P. TÖRMÄ. *Vacuum Rabi Splitting and Strong-Coupling Dynamics for Surface-Plasmon Polaritons and Rhodamine 6G Molecules*. *Physical Review Letters* **103**, 053602 (2009).
- [36] N. J. HALAS. *Plasmonics: An Emerging Field Fostered by Nano Letters*. *Nano Letters* **10**, 3816 (2010).
- [37] M. HENTSCHEL, M. SALIBA, R. VOGELGESANG, H. GIESSEN, A. P. ALIVISATOS and N. LIU. *Transition from Isolated to Collective Modes in Plasmonic Oligomers*. *Nano Letters* **10**, 2721 (2010).
- [38] W. HOLLAND and D. HALL. *Surface-plasmon dispersion relation: Shifts induced by the interaction with localized plasma resonances*. *Physical Review B* **27**, 7765 (1983).
- [39] W. HOLLAND and D. HALL. *Frequency Shifts of an Electric-Dipole Resonance near a Conducting Surface*. *Physical Review Letters* **52**, 1041 (1984).
- [40] J. HOMOLA. *Surface plasmon resonance sensors: review*. *Sensors and Actuators B: Chemical* **54**, 3 (1999).
- [41] M. HUANG, A. A. YANIK, T.-Y. CHANG and H. ALTUG. *Sub-wavelength nanofluidics in photonic crystal sensors*. *Optics Express* **17**, 24224 (2009).
-

- [42] M. HÜBNER, J. KUHL, T. STROUCKEN, A. KNORR, S. W. KOCH, R. HEY and K. PLOOG. *Collective Effects of Excitons in Multiple-Quantum-Well Bragg and Anti-Bragg Structures*. Physical Review Letters **76**, 4199 (1996).
- [43] M. HÜBNER, J. P. PRINEAS, C. ELL, P. BRICK, E. S. LEE, G. KHITROVA, H. M. GIBBS and S. W. KOCH. *Optical Lattices Achieved by Excitons in Periodic Quantum Well Structures*. Physical Review Letters **83**, 2841 (1999).
- [44] J. D. JACKSON. *Classical Electrodynamics*. Wiley (1962).
- [45] E. E. JELLEY. *Spectral absorption and fluorescence of dyes in the molecular state*. Nature **138**, 1009 (1936).
- [46] P. B. JOHNSON and R. W. CHRISTY. *Optical Constants of the Noble Metals*. Physical Review B **6**, 4370 (1972).
- [47] G. KHITROVA, H. M. GIBBS, F. JAHNKE, M. KIRA and S. W. KOCH. *Nonlinear optics of normal-mode-coupling semiconductor microcavities*. Reviews of Modern Physics **71**, 1591 (1999).
- [48] G. KHITROVA, H. M. GIBBS, M. KIRA, S. W. KOCH and A. SCHERER. *Vacuum Rabi splitting in semiconductors*. Nature Physics **2**, 81 (2006).
- [49] U. KREIBIG and M. VOLLMER. *Optical Properties of Metal Clusters*. Springer (1995).
- [50] E. KRETSCHMANN and H. RAETHER. *Radiative decay of non-radiative surface plasmons excited by light*. Zeitschrift für Naturforschung A **23**, 2135 (1968).
- [51] S. LAL, S. LINK and N. J. HALAS. *Nano-optics from sensing to waveguiding*. Nature Photonics **1**, 641 (2007).
- [52] L. LANGGUTH. *Coupling in Metamaterials*. Diploma thesis, University of Stuttgart (2010).
- [53] E. M. LARSSON, C. LANGHAMMER, I. ZORIĆ and B. KASEMO. *Nanoplasmonic Probes of Catalytic Reactions*. Science **326**, 1091 (2009).
- [54] J. B. LASSITER, H. SOBHANI, J. A. FAN, J. KUNDU, F. CAPASSO, P. NORDLANDER and N. J. HALAS. *Fano Resonances in Plasmonic Nanoclusters: Geometrical and Chemical Tunability*. Nano Letters **10**, 3184 (2010).
- [55] L. LI. *Use of Fourier series in the analysis of discontinuous periodic structures*. Journal of the Optical Society of America A **13**, 1870 (1996).
- [56] L. LI. *New formulation of the Fourier modal method for crossed surface-relief gratings*. Journal of the Optical Society of America A **14**, 2758 (1997).
- [57] H. LIAO, C. L. NEHL and J. H. HAFNER. *Biomedical applications of plasmon resonant metal nanoparticles*. Nanomedicine **1**, 201 (2006).
- [58] W. LICHTEN. *Precise wavelength measurements and optical phase shifts. I. General theory*. Journal of the Optical Society of America A **2**, 1869 (1985).

-
- [59] N. LIU, L. FU, S. KAISER, H. SCHWEIZER and H. GIESSEN. *Plasmonic Building Blocks for Magnetic Molecules in Three-Dimensional Optical Metamaterials*. *Advanced Materials* **20**, 3859 (2008).
- [60] N. LIU, H. GUO, L. FU, S. KAISER, H. SCHWEIZER and H. GIESSEN. *Plasmon Hybridization in Stacked Cut-Wire Metamaterials*. *Advanced Materials* **19**, 3628 (2007).
- [61] N. LIU, H. GUO, L. FU, S. KAISER, H. SCHWEIZER and H. GIESSEN. *Three-dimensional photonic metamaterials at optical frequencies*. *Nature Materials* **7**, 31 (2008).
- [62] N. LIU, S. KAISER and H. GIESSEN. *Magnetoinductive and Electroinductive Coupling in Plasmonic Metamaterial Molecules*. *Advanced Materials* **20**, 4521 (2008).
- [63] N. LIU, L. LANGGUTH, T. WEISS, J. KÄSTEL, M. FLEISCHHAUER, T. PFAU and H. GIESSEN. *Plasmonic analogue of electromagnetically induced transparency at the Drude damping limit*. *Nature Materials* **8**, 758 (2009).
- [64] N. LIU, H. LIU, S. ZHU and H. GIESSEN. *Stereometamaterials*. *Nature Photonics* **3**, 157 (2009).
- [65] N. LIU, M. MESCH, T. WEISS, M. HENTSCHEL and H. GIESSEN. *Infrared Perfect Absorber and Its Application As Plasmonic Sensor*. *Nano Letters* **10**, 2342 (2010).
- [66] N. LIU, T. WEISS, M. MESCH, L. LANGGUTH, U. EIGENTHALER, M. HIRSCHER, C. SÖNNICHSEN and H. GIESSEN. *Planar Metamaterial Analogue of Electromagnetically Induced Transparency for Plasmonic Sensing*. *Nano Letters* **10**, 1103 (2010).
- [67] D. LU, H. LIU, T. LI, S. M. WANG, F. M. WANG, S. N. ZHU and X. ZHANG. *Creation of a magnetic plasmon polariton through strong coupling between an artificial magnetic atom and the defect state in a defective multilayer microcavity*. *Physical Review B* **77**, 214302 (2008).
- [68] F. MA and X. LIU. *Phase shift and penetration depth of metal mirrors in a microcavity structure*. *Applied Optics* **46**, 6247 (2007).
- [69] S. A. MAIER. *Plasmonics: Fundamentals and Applications*. Springer (2007).
- [70] S. A. MAIER, M. L. BRONGERSMA, P. G. KIK and H. A. ATWATER. *Observation of near-field coupling in metal nanoparticle chains using far-field polarization spectroscopy*. *Physical Review B* **65**, 193408 (2002).
- [71] S. A. MAIER, P. G. KIK and H. A. ATWATER. *Observation of coupled plasmon-polariton modes in Au nanoparticle chain waveguides of different lengths: Estimation of waveguide loss*. *Applied Physics Letters* **81**, 1714 (2002).
- [72] S. A. MAIER, P. G. KIK, H. A. ATWATER, S. MELTZER, E. HAREL, B. E. KOEL and A. G. REQUICHA. *Local detection of electromagnetic energy transport below the diffraction limit in metal nanoparticle plasmon waveguides*. *Nature Materials* **2**, 229 (2003).
- [73] G. MATTEI, P. MAZZOLDI, M. L. POST, D. BUSO, M. GUGLIELMI and A. MARTUCCI. *Cookie-like Au/NiO Nanoparticles with Optical Gas-Sensing Properties*. *Advanced Materials* **19**, 561 (2007).
-

- [74] M. MESCH. *Metamaterial Sensors*. Diploma thesis, University of Stuttgart (2009).
- [75] T. P. MEYRATH, T. ZENTGRAF, C. ROCKSTUHL and H. GIESSEN. *Electromagnetic induction in metamaterials*. Applied Physics B **93**, 107 (2008).
- [76] P. MEYSTRE. *Cavity Quantum Optics and the Quantum Measurement Process*. Progress in Optics **30**, 261 (1992).
- [77] G. MIE. *Beiträge zur Optik trüber Medien, speziell kolloidaler Metallösungen*. Annalen der Physik **25**, 377 (1908).
- [78] D. MÖBIUS. *Scheibe Aggregates*. Advanced Materials **7**, 437 (1995).
- [79] J. J. MOCK, D. R. SMITH and S. SCHULTZ. *Local Refractive Index Dependence of Plasmon Resonance Spectra from Individual Nanoparticles*. Nano Letters **3**, 485 (2003).
- [80] P. MÜHLSCHLEGEL, H.-J. EISLER, O. J. F. MARTIN, B. HECHT and D. W. POHL. *Resonant optical antennas*. Science **308**, 1607 (2005).
- [81] N. NATH and A. CHILKOTI. *A Colorimetric Gold Nanoparticle Sensor to Interrogate Biomolecular Interactions in Real Time on a Surface*. Analytical Chemistry **74**, 504 (2002).
- [82] D. NAU, A. SEIDEL, R. B. ORZEKOWSKY, S.-H. LEE, S. DEB and H. GIESSEN. *Hydrogen sensor based on metallic photonic crystal slabs*. Optics Letters **35**, 3150 (2010).
- [83] P. NORDLANDER, C. OUBRE, E. PRODAN, K. LI and M. I. STOCKMAN. *Plasmon Hybridization in Nanoparticle Dimers*. Nano Letters **4**, 899 (2004).
- [84] L. NOVOTNY. *Effective Wavelength Scaling for Optical Antennas*. Physical Review Letters **98**, 266802 (2007).
- [85] M. A. ORDAL, L. L. LONG, R. J. BELL, S. E. BELL, R. R. BELL, R. W. ALEXANDER JR. and C. A. WARD. *Optical properties of the metals Al, Co, Cu, Au, Fe, Pb, Ni, Pd, Pt, Ag, Ti, and W in the infrared and far infrared*. Applied Optics **22**, 1099 (1983).
- [86] A. OTTO. *Excitation of nonradiative surface plasma waves in silver by the method of frustrated total reflection*. Zeitschrift für Physik **216**, 398 (1968).
- [87] R. F. OULTON, V. J. SORGER, T. ZENTGRAF, R.-M. MA, C. GLADDEN, L. DAI, G. BARTAL and X. ZHANG. *Plasmon lasers at deep subwavelength scale*. Nature **461**, 629 (2009).
- [88] J. PARSONS, I. R. HOOPER, W. L. BARNES and J. R. SAMBLES. *Interactions between Fabry-Pérot and nanohole resonances in metallo-dielectric plasmonic nanostructures*. Journal of Modern Optics **56**, 1199 (2009).
- [89] J. PENDRY. *Negative Refraction Makes a Perfect Lens*. Physical Review Letters **85**, 3966 (2000).
- [90] J. B. PENDRY, D. SCHURIG and D. R. SMITH. *Controlling electromagnetic fields*. Science **312**, 1780 (2006).

-
- [91] R. PERAHIA, T. P. M. ALEGRE, A. H. SAFAVI-NAEINI and O. PAINTER. *Surface-plasmon mode hybridization in subwavelength microdisk lasers*. Applied Physics Letters **95**, 201114 (2009).
- [92] E. PETER, P. SENELLART, D. MARTROU, A. LEMAÎTRE, J. HOURS, J. M. GERARD and J. BLOCH. *Exciton-Photon Strong-Coupling Regime for a Single Quantum Dot Embedded in a Microcavity*. Physical Review Letters **95**, 067401 (2005).
- [93] J. M. PITARKE, V. M. SILKIN, E. V. CHULKOV and P. M. ECHENIQUE. *Theory of surface plasmons and surface-plasmon polaritons*. Reports on Progress in Physics **70**, 1 (2007).
- [94] V. A. PODOLSKIY, A. K. SARYCHEV, E. E. NARIMANOV and V. M. SHALAEV. *Resonant light interaction with plasmonic nanowire systems*. Journal of Optics A: Pure and Applied Optics **7**, 32 (2005).
- [95] V. A. PODOLSKIY, A. K. SARYCHEV and V. M. SHALAEV. *Plasmon modes in metal nanowires and left-handed materials*. Journal of Nonlinear Optical Physics and Materials **11**, 65 (2002).
- [96] C. J. POWELL and J. B. SWAN. *Effect of Oxidation on the Characteristic Loss Spectra of Aluminum and Magnesium*. Physical Review **118**, 640 (1960).
- [97] E. PRODAN, C. RADLOFF, N. J. HALAS and P. NORDLANDER. *A Hybridization Model for the Plasmon Response of Complex Nanostructures*. Science **302**, 419 (2003).
- [98] H. RAETHER. *Surface Plasmons on Smooth and Rough Surfaces and on Gratings*. Springer (1988).
- [99] M. REIBOLD, P. PAUFLER, A. A. LEVIN, W. KOCHMANN, N. PÄTZKE and D. C. MEYER. *Carbon nanotubes in an ancient Damascus sabre*. Nature **444**, 286 (2006).
- [100] J. P. REITHMAIER, G. SEK, A. LÖFFLER, C. HOFMANN, S. KUHN, S. REITZENSTEIN, L. V. KELDYSH, V. D. KULAKOVSKII, T. L. REINECKE and A. FORCHEL. *Strong coupling in a single quantum dot-semiconductor microcavity system*. Nature **432**, 197 (2004).
- [101] R. H. RITCHIE. *Plasma Losses by Fast Electrons in Thin Films*. Physical Review **106**, 874 (1957).
- [102] J. R. SAMBLES, G. W. BRADBERY and F. YANG. *Optical excitation of surface plasmons: an introduction*. Contemporary Physics **32**, 173 (1991).
- [103] D. SARID and W. CHALLENGER. *Modern Introduction to Surface Plasmons*. Cambridge University Press (2010).
- [104] M. SCALORA, M. J. BLOEMER, A. S. PETHEL, J. P. DOWLING, C. M. BOWDEN and A. S. MANKA. *Transparent, metallo-dielectric, one-dimensional, photonic band-gap structures*. Journal of Applied Physics **83**, 2377 (1998).
- [105] G. SCHEIBE. *Über die Veränderlichkeit der Absorptionsspektren in Lösungen und die Nebenvalenzen als ihre Ursache*. Angewandte Chemie **50**, 212 (1937).
-

REFERENCES

- [106] P. J. SCHUCK, D. P. FROMM, A. SUNDARAMURTHY, G. S. KINO and W. E. MOERNER. *Improving the Mismatch between Light and Nanoscale Objects with Gold Bowtie Nanoantennas*. Physical Review Letters **94**, 017402 (2005).
- [107] V. M. SHALAEV. *Optical negative-index metamaterials*. Nature Photonics **1**, 41 (2007).
- [108] L. J. SHERRY, S.-H. CHANG, G. C. SCHATZ, R. P. VAN DUYNÉ, B. J. WILEY and Y. XIA. *Localized Surface Plasmon Resonance Spectroscopy of Single Silver Nanocubes*. Nano Letters **5**, 2034 (2005).
- [109] A. SOMMERFELD. *Ueber die Fortpflanzung elektrodynamischer Wellen längs eines Drahtes*. Annalen der Physik und Chemie **303**, 233 (1899).
- [110] C. SÖNNICHSEN, T. FRANZL, T. WILK, G. VON PLESSEN and J. FELDMANN. *Drastic Reduction of Plasmon Damping in Gold Nanorods*. Physical Review Letters **88**, 077402 (2002).
- [111] V. J. SORGER, R. F. OULTON, J. YAO, G. BARTAL and X. ZHANG. *Plasmonic Fabry-Pérot Nanocavity*. Nano Letters **9**, 3489 (2009).
- [112] C. M. SOUKOULIS, S. LINDEN and M. WEGENER. *Negative Refractive Index at Optical Wavelengths*. Science **315**, 47 (2007).
- [113] R. TAUBERT, R. AMELING, T. WEISS, A. CHRIST and H. GIESSEN. *From Near-Field to Far-Field Coupling in Three Dimensions: Retarded Interaction of Particle Plasmons*. (submitted) (2011).
- [114] R. TAUBERT, D. DREGELY, A. CHRIST and H. GIESSEN. *Octave-Wide Photonic Band Gap in Three-Dimensional Plasmonic Bragg Structures*. (in preparation) (2011).
- [115] M.-L. THÈYE. *Investigation of the Optical Properties of Au by Means of Thin Semitransparent Films*. Physical Review B **2**, 3060 (1970).
- [116] R. J. THOMPSON, G. REMPE and H. J. KIMBLE. *Observation of Normal-Mode Splitting for an Atom in an Optical Cavity*. Physical Review Letters **68**, 1132 (1992).
- [117] S. G. TIKHODEEV, A. L. YABLONSKII, E. A. MULJAROV, N. A. GIPPIUS and T. ISHIHARA. *Quasiguidded modes and optical properties of photonic crystal slabs*. Physical Review B **66**, 045102 (2002).
- [118] S. TRETYAKOV. *Analytical Modeling in Applied Electromagnetics*. Artech (2003).
- [119] S. M. ULRICH, C. GIES, S. ATES, J. WIERSIG, S. REITZENSTEIN, C. HOFMANN, A. LÖFFLER, A. FORCHEL, F. JAHNKE and P. MICHLER. *Photon Statistics of Semiconductor Microcavity Lasers*. Physical Review Letters **98**, 043906 (2007).
- [120] C. WEISBUCH, M. NISHIOKA, A. ISHIKAWA and Y. ARAKAWA. *Observation of the Coupled Exciton-Photon Mode Splitting in a Semiconductor Quantum Microcavity*. Physical Review Letters **69**, 3314 (1992).
- [121] T. WEISS, N. A. GIPPIUS, S. G. TIKHODEEV, G. GRANET and H. GIESSEN. *Efficient calculation of the optical properties of stacked metamaterials with a Fourier modal method*. Journal of Optics A: Pure and Applied Optics **11**, 114019 (2009).

- [122] T. WEISS, G. GRANET, N. A. GIPPIUS, S. G. TIKHODEEV and H. GIESSEN. *Matched coordinates and adaptive spatial resolution in the Fourier modal method*. Optics Express **17**, 8051 (2009).
- [123] D. M. WHITTAKER and I. S. CULSHAW. *Scattering-matrix treatment of patterned multi-layer photonic structures*. Physical Review B **60**, 2610 (1999).
- [124] K. A. WILLETS and R. P. VAN DUYN. *Localized Surface Plasmon Resonance Spectroscopy and Sensing*. Annual Review of Physical Chemistry **58**, 267 (2007).
- [125] A. A. YANIK, M. HUANG, A. ARTAR, T.-Y. CHANG and H. ALTUG. *Integrated nanoplasmonic-nanofluidic biosensors with targeted delivery of analytes*. Applied Physics Letters **96**, 021101 (2010).
- [126] K. S. YEE. *Numerical Solution of Initial Boundary Value Problems Involving Maxwell's Equations in Isotropic Media*. IEEE Transactions on Antennas and Propagation **14**, 302 (1966).
- [127] Y.-L. YEH. *Real-time measurement of glucose concentration and average refractive index using a laser interferometer*. Optics and Lasers in Engineering **46**, 666 (2008).
- [128] T. YOSHIE, A. SCHERER, J. HENDRICKSON, G. KHITROVA, H. M. GIBBS, G. RUPPER, C. ELL, O. B. SHCHEKIN and D. G. DEPPE. *Vacuum Rabi splitting with a single quantum dot in a photonic crystal nanocavity*. Nature **432**, 200 (2004).
- [129] L. ZHAO, K. L. KELLY and G. C. SCHATZ. *The Extinction Spectra of Silver Nanoparticle Arrays: Influence of Array Structure on Plasmon Resonance Wavelength and Width*. The Journal of Physical Chemistry B **107**, 7343 (2003).
- [130] J. ZHOU, T. KOSCHNY, M. KAFESAKI and C. M. SOUKOULIS. *Negative refractive index response of weakly and strongly coupled optical metamaterials*. Physical Review B **80**, 035109 (2009).
- [131] R. ZIA, J. SCHULLER, A. CHANDRAN and M. BRONGERSMA. *Plasmonics: the next chip-scale technology*. Materials Today **9**, 20 (2006).
- [132] R. ZSIGMONDY. *Ueber wässrige Lösungen metallischen Goldes*. Justus Liebigs Annalen der Chemie **301**, 29 (1898).

LIST OF FIGURES

1	Coloration of glasses by small metal particles	13
2	Applications of plasmonics	14
3	Dielectric function of gold (visible spectrum)	20
4	Dielectric function of gold (near-infrared spectrum)	21
5	Microcavity models: Apparent length increase and phase shifts	23
6	Microcavity resonance wavelengths	24
7	Surface plasmons at a metal-dielectric interface	24
8	Dispersion relation of surface plasmons	26
9	Surface plasmon excitation configurations	26
10	Localized plasmon in a nanosphere	27
11	Metal nanosphere in a homogeneous static electric field	28
12	Plasmon resonances in a nanorod	30
13	Plasmon resonances in a continuous nanowire	32
14	Metal evaporation with an electron beam	36
15	Ion beam etching	37
16	Layer scheme of electron beam lithography processes	38
17	SEM image of lift-off	40
18	FTIR spectrometer beam paths	41
19	Infrared microscope beam paths	42
20	Spectral coverage of FTIR spectrometer components	43
21	Examples of near-field coupled plasmonic nanostructures	45
22	Dipolar electric fields of near-field coupled nanoparticles	46
23	Energy diagram of hybridized localized plasmon resonances	47
24	Experimental measurements of nanorod pairs	49
25	Current densities and magnetic fields of nanorod pairs	50
26	Nanorods in front of a mirror	51
27	Transition from near- to far-field coupling	52
28	Phase shifts for cavities consisting of nanostructured mirrors	53
29	Homogeneous plasmonic layer with effective permittivity	54
30	Reflectance spectra of nanostructured cavities	55
31	Reflectance spectra of multilayer cavity stacks	58
32	Strong coupling of atoms in a cavity	60
33	Nanorods and nanorod pairs in a microcavity	62
34	Resonances of single nanorods in a microcavity	63
35	Resonances of nanorod pairs in a microcavity	65

36	Nanorod pairs at different positions in a microcavity	66
37	Electric and magnetic field distributions for nanorods in a microcavity . .	67
38	Fabrication scheme and SEM images of nanorod pairs in a microcavity . .	69
39	Measured and simulated reflection spectra of nanorods in a microcavity .	70
40	Multilayer stacks of nanorods in a microcavity	72
41	Localized and surface plasmon excitation and coupling to cavity modes .	76
42	SEM images of nanowires close to a mirror	78
43	Sample press	78
44	Coupled cavity, surface plasmon and localized plasmon modes (color plot)	79
45	Coupled cavity, surface plasmon and localized plasmon modes (graph) . .	80
46	Cavity-assisted far-field interactions of plasmons	81
47	Principle of LSPR sensing	84
48	Dependence of the plasmon resonance shift on the structure geometry . .	85
49	Detection methods of plasmon resonance shifts	86
50	Decreased linewidth of a plasmon resonance when coupled to a cavity . .	87
51	Phase shifts and reflectance plot of nanorods combined with a cavity . . .	88
52	Enhancement of sensitivity and figure of merit at Bragg distance	89
53	Distribution of the electric field in the cavity sensor structure	90
54	Variation of the period of nanorods combined with a cavity	92
55	Variation of the incident angle on nanorods combined with a cavity	92
56	SEM images of nanorods combined with a cavity	93
57	Microfluidic sensing cell	94
58	Spectra of nanorods compared to nanorods combined with a cavity.	94
59	Sensitivity and figure of merit of nanorods compared to nanorods com- bined with a cavity.	96
60	Coupled excitons and plasmons	98
61	Nanostars combined with a microcavity	99

LIST OF ABBREVIATIONS

$a_{x,y,z}$	nanorod size
$C_{\text{abs, ext, sca}}$	absorption, extinction, and scattering cross-section
\vec{D}	dielectric displacement
d	mirror, nanorod or nanowire distance
E	energy
$\vec{E} = (E_x, E_y, E_z)$...	electric field
$E_{\text{inc, refl}}$	incident and reflected electric field amplitude
e	elementary charge
FDTD	finite difference time domain
FIB	focussed ion beam
FMM	Fourier model method
FOM	figure of merit (with respect to resonance linewidth)
FOM*	figure of merit (with respect to absolute intensity)
FWHM	full width at half maximum
FTIR	Fourier transform infrared spectroscopy
g	coupling strength
H	Hamiltonian
$\vec{H} = (H_x, H_y, H_z)$..	magnetic field
\hbar	reduced Planck constant
I	intensity
ΔI	intensity variation
$\vec{k} = (k_x, k_y, k_z)$	wave vector
LSPR	localized surface plasmon resonance
m_e	effective electron mass in the quasi-free electron model
MCT	mercury cadmium telluride
MIBK	methyl-isobutyl-ketone
N	positive integer
n	refractive index
n_A	refractive index of analyte
$n_{\text{cav, met, sub}}$	refractive index of microcavity, metal, and glass substrate
n_e	electron density
n_{LP}	effective refractive index of plasmonic layer
Δn	refractive index change
NMP	N-Methyl-2-pyrrolidone

LIST OF ABBREVIATIONS

\vec{P}	macroscopic polarization
$p_{x,y}$	lateral period
\vec{p}	electric dipole moment
PMMA	polymethyl-methacrylate
QD	quantum dot
R	reflectance
\vec{r}	position vector
S	sensitivity (with respect to spectral shifts)
S^*	sensitivity (with respect to intensity variations)
SEM	scanning electron microscope
SERS	surface-enhanced Raman spectroscopy
t	time
T	periodic time
T_d	dephasing time
α	polarizability
Γ	full width at half maximum
γ_e	electron damping in the quasi-free electron model
δ	apparent length increase
ϵ	electric permittivity
ϵ_0	electric permittivity of vacuum
θ	incident angle
κ_E	radiation losses due to spontaneous emission
κ_M	radiation losses at a mirror
λ	wavelength
$\Delta\lambda$	spectral shift
ν	frequency
σ	electric conductivity
Φ	electrostatic potential
$\Delta\varphi$	phase shift
$\Delta\varphi_{\text{exc}}$	phase shift upon plasmon excitation
$\Delta\varphi_{\text{prop, refl}}$	phase shift on propagation and upon reflection
$\Delta\varphi_{\text{tot}}$	total phase shift
χ	dielectric susceptibility
ψ	eigenstate
ω	resonance frequency
ω_p	plasma frequency

The indices d and m are used to specify parameters in a dielectric or metallic environment. Furthermore, the indices LP , SP , and N denote the affiliation to localized plasmons, surface plasmons, and the N -th order microcavity mode.

PUBLICATION LIST

Parts of this thesis have been published

- **in scientific journals:**

R. AMELING and H. GIESSEN. *Cavity Plasmonics: Large normal mode splitting of electric and magnetic particle plasmons induced by a photonic microcavity*. Nano Letters **10**, 4394 (2010).

R. AMELING, L. LANGGUTH, M. HENTSCHEL, M. MESCH, and H. GIESSEN. *Cavity-enhanced localized plasmon resonance sensing*. Applied Physics Letters **97**, 253116 (2010).

R. AMELING, D. DREGELY, and H. GIESSEN. *Strong coupling of localized and surface plasmons to microcavity modes*. Optics Letters **36**, 2218 (2011).

R. TAUBERT, R. AMELING, T. WEISS, A. CHRIST, and H. GIESSEN. *From Near-Field to Far-Field Coupling in Three Dimensions: Retarded Interaction of Particle Plasmons*. Submitted (2011).

- **at international conferences:**

R. AMELING and H. GIESSEN. *Microcavity plasmonics*. CLEO/QELS (Conference on Lasers and Electro-Optics / Quantum Electronics and Laser Science Conference), Talk QFC4 (May 2010, San Jose, CA, USA).

R. AMELING and H. GIESSEN. *Giant splitting of localized electric and magnetic plasmon modes in a photonic microcavity*. Photonic Metamaterials and Plasmonics (OSA conference), Talk MTuC4 (June 2010, Tucson, AZ, USA).

H. GIESSEN, N. LIU, M. HENTSCHEL, and R. AMELING. *Plasmonic coupling games*. Plasmonics Gordon Research Conference, Talk (June 2010, Waterville, ME, USA).

R. AMELING and H. GIESSEN. *Strong coupling of localized magnetic and electric plasmons to photonic microcavity modes*. Metamaterials 2010 (Fourth International Congress on Advanced Electromagnetic Materials in Microwaves and Optics), Talk (September 2010, Karlsruhe, Germany).

R. AMELING, L. LANGGUTH, M. HENTSCHEL, M. MESCH, and H. GIESSEN. *Cavity-enhanced localized plasmon resonance sensing*. Nanometa: The 3rd European Topical Meeting on Nanophotonics and Metamaterials, Talk TUE2o.2 (January 2011, Seefeld, Austria).

R. TAUBERT, R. AMELING, T. WEISS, A. CHRIST, and H. GIESSEN. *From near-field to far-field: Radiative coupling of particle plasmon resonances in three-dimensional geometries*. Nanometa: The 3rd European Topical Meeting on Nanophotonics and Metamaterials, Talk THU2s.3 (January 2011, Seefeld, Austria).

R. TAUBERT, R. AMELING, T. WEISS, A. CHRIST, and H. GIESSEN. *From Near-Field to Far-Field: Radiative Coupling of Particle Plasmon Resonances in Three-Dimensional Geometries*. CLEO/Europe-EQEC (Conference on Lasers and Electro-Optics / European Quantum Electronic Conference), Talk CK3.5 (May 2011, München, Germany).

R. AMELING, D. DREGELY, and H. GIESSEN. *Strong coupling of localized and surface plasmons to microcavity modes*. Metamaterials 2011 (Fifth International Congress on Advanced Electromagnetic Materials in Microwaves and Optics), Poster (October 2011, Barcelona, Spain).

• **at national conferences:**

R. AMELING and H. GIESSEN. *Plasmon interactions in stacked cut-wire metamaterials*. Spring Meeting of the German Physical Society (DPG), Poster O27.76 (March 2009, Dresden).

R. AMELING and H. GIESSEN. *Microcavity plasmonics*. Spring Meeting of the German Physical Society (DPG), Talk O63.7 (March 2010, Regensburg).

R. TAUBERT, R. AMELING, L. LANGGUTH, D. DRÉGELY, and H. GIESSEN. *Bragg plasmonics*. Spring Meeting of the German Physical Society (DPG), Talk O83.5 (March 2010, Regensburg).

R. AMELING, L. LANGGUTH, M. HENTSCHEL, M. MESCH, and H. GIESSEN. *Cavity-enhanced localized plasmon resonance sensing*. Spring Meeting of the German Physical Society (DPG), Talk O50.6 (March 2011, Dresden).

• **at workshops and seminars:**

R. AMELING, H. GUO, L. FU, N. LIU, and H. GIESSEN. *Simulation of negative-index metamaterials at optical frequencies and nano-antennas*. CST Microwave Studio User Workshop (June 2008, Enschede).

R. AMELING and H. GIESSEN. *Microcavity plasmonics*. Meeting of the Research Group FOR557 “Light Confinement and Control with Structured Dielectrics and Metals” (November 2009, Bonn).

Additional publications not presented in this thesis

- **in scientific journals:**

A. SIEGEL, M. R. GONÇALVES, R. AMELING, and O. MARTI. *Investigations of the light scattering structure factor of metallic nanostructures using Bragg diffraction*. Journal of Optics A: Pure and Applied Optics **9**, 443 (2007).

H. LIU, J. X. CAO, S. N. ZHU, N. LIU, R. AMELING, and H. GIESSEN. *Lagrange model for the chiral optical properties of stereometamaterials*. Physical Review B **81**, 241403 (2010).

- **at conferences:**

M. R. GONÇALVES, A. SIEGEL, R. AMELING, and O. MARTI. *Scattering of light at micro- and nanostructures of triangular shape*. SPIE Conference Proceedings “Complex Light and Optical Forces”, 64830B (2007).

R. AMELING, M. R. GONÇALVES, A. SIEGEL, and O. MARTI. *Talbot effect at two-dimensional microscopic periodic structures*. Spring Meeting of the German Physical Society (DPG), Poster Q65.6 (March 2007, Düsseldorf).

M. R. GONÇALVES, R. AMELING, A. SIEGEL, and O. MARTI. *Optical self-imaging of gratings fabricated using colloidal crystals and soft-lithography*. Spring Meeting of the German Physical Society (DPG), Talk Q48.1 (March 2007, Düsseldorf).

A. SIEGEL, M. R. GONÇALVES, R. AMELING, and O. MARTI. *Investigation of plasmon resonances and Bragg diffraction properties of metallic nanostructures*. Spring Meeting of the German Physical Society (DPG), Poster O17.12 (March 2007, Regensburg).

M. R. GONÇALVES, A. SIEGEL, R. AMELING, and O. MARTI. *Investigation of the scattering form factor and surface plasmon resonances of metallic nanoparticles by Bragg diffraction*. Spring Meeting of the German Physical Society (DPG), Talk O39.1 (March 2007, Regensburg).

CURRICULUM VITAE

- Personal details

Date of birth	April, 25th 1981
Address	Sperberweg 38, 73434 Aalen
Email	ralf.aming@gmx.de

- Education

1987-1991	Primary School Aalen-Hofherrweiler
1991-2000	Secondary School Schubart-Gymnasium Aalen
2000-2001	Civil Service at Johanniter-Unfallhilfe Aalen
2001-2007	Diploma in Physics (Grade 1.2), University of Ulm Diploma thesis at the Institute of Experimental Physics “The Talbot effect and its dependence on wavelength and structure geometry”
2007-2011	PhD thesis “Microcavity Plasmonics” University of Stuttgart, 4th Physics Institute

ACKNOWLEDGEMENTS

Without the help and support of many people, this thesis would not have been possible. I would like to thank everybody who has contributed in any way to this work. Special thanks go to

- Prof. Dr. Harald Giessen for providing the possibility to accomplish this thesis at the 4th Physics Institute, for many hints, discussions and encouraging words
- Prof. Dr. Peter Michler for kindly agreeing to be the second advisor
- Prof. Dr. Günter Wunner for kindly taking the chair of the examination committee
- Richard Taubert for many useful discussions and help at simulations and experiments
- Lutz Langguth for many tips and ideas, especially concerning the cavity-enhanced plasmon sensing
- Mario Hentschel for the electron beam lithography of the sensing samples
- Daniel Dregely for the electron beam lithography of the surface plasmon samples
- Martin Mesch for everything concerned with Glucose sensing
- Thomas Weiss for his S-matrix code and its constant improvement
- Hedi Gräbeldinger and Monika Ubl for assistance and support in the cleanroom
- Bernhard Fenk (MPI for Solid State Research), Ulrike Eigenthaler (MPI for Intelligent Systems), and Bernhard Reuscher (IFOS Kaiserslautern) for the focussed ion beam support
- Prof. Paul V. Braun for useful discussions about the plasmon sensing project
- all current and former members of the 4th Physics Institute for the nice atmosphere at work and at many excursions and conferences, for all parties, barbecues, Karaoke nights, Weißwurtsfrühstücks, movie nights, ... it was a great time!